MASTER OF SCIENCE THESIS

Optimisation of Fibre Metal Laminate Splice Designs with Focus on Fatigue Performance

A Multi-Disciplinary Approach

Mykyta Poliakov

Faculty of Aerospace Engineering · Delft University of Technology

Optimisation of Fibre Metal Laminate Splice Designs with Focus on Fatigue Performance

A Multi-Disciplinary Approach

MASTER OF SCIENCE THESIS

For obtaining the degree of Master of Science in Aerospace Engineering
at Delft University of Technology

Mykyta Poliakov

18th August, 2023

Faculty of Aerospace Engineering · Delft University of Technology

The work in this thesis was supported by GTM Advanced Structures B.V.. Their cooperation is gratefully acknowledged.

Delft University of Technology
Faculty of Aerospace Engineering
Department of Aerospace Structures and Materials

GRADUATION COMMITTEE

Dated: 18th August, 2023

Chair holder:

Dr.ir. René C. Alderliesten

Committee members:

Dr.ir. John-Alan Pascoe

Dr.ing. Saullo G. P. Castro

ir. Johannes J. Homan

Preface

This thesis report is written to fulfill the requirements for obtaining a Masters of Science in Aerospace Engineering degree. The topic describes a predictive methodology that is used to predict damage initiation within Fibre Metal Laminates due to fatigue loading, and later applies that methodology to adapt designs of existing splice joint configurations, while also comparing the performance of two most prominent configurations of the splice joint. Research was done at Delft University of Technology and in collaboration with GTM Advanced Structures B.V., located in Ypenburg, The Hague.

Although the topic for this research did not stem from my own ideas, the research was naturally shaped around the topic most passionate to me in engineering - numerical predictive modelling and experimental work.

I would like to thank GTM Advanced Structures, specifically ir. Johannes Homan for his valuable insights into experimental testing of Fibre Metal Laminates, ir. Simon Gunnink, Niamara van Woggelum, and Simon Vlatter for their time and efforts to help me with the manufacturing of the splice samples, and ir. Jan Willem Gunnink for allocating the resources and his deep expertise to this research.

I would like express my gratitude to my supervisor Dr. ir. René Alderliesten for his countless feedback and help during the course of this research. He taught me that, although often overlooked, general engineering judgement that we as students spend years developing is crucial when it comes to experimental work. I could always rely on Dr. René in providing me with prompt responses to problems I desperately needed to solve, and for that I am very grateful. It was a pleasure working with him during the course of this research and I encourage any future students who are interested in structural integrity, fatigue and damage tolerance, and of course fibre metal laminates to approach Dr. René for his supervision.

Finally, I would like to thank my friends, colleagues, and family for always supporting me and making this journey so much easier, and that goes not just for this research, but also the entirety of my academic journey to becoming a Master of Science in so-called "Rocket Science".

Executive Summary

Although a relatively new material, Fibre Metal Laminates (FMLs) have been widely utilised in aircraft structures for their specific strength, durability and damage tolerance. Most aircraft structures, due to their size, require joining, and FMLs allow for a special type of joint called the splice, a unique but a lesser known joint.

The bulk of research into the splice joint has been conducted in the early 2000s for the A380 program, where a specific type of splice has been implemented, the overlap splice. While it is a proven design, it was expected that other splice designs could be as good if not better than the overlap splice. Further, the pre-existing design guidelines on the splices were not suited for detailed design that would target specific mechanical strengths of the joint, like durability and damage tolerance. Therefore, this research focused on design iterations of the two splice types, the butt splice and the overlap splice, that would provide insights into splice design guidelines against fatigue and demonstrate which splice configuration is a superior joint. An extension of this research focuses on identification of location and lifetime to damage initiation within the splice using analytical numerical methods, which was previously done on uninterrupted FMLs, but not on spliced FMLs.

Research comprises of a multi-disciplinary approach, combining Finite Element Method (FEM), numerical predictive modelling and experimental investigations that then also doubled as means of validation of the models built. Design iterations were based on the influence that the parameters, labeled **a** through **e**, within the splice joint have on the overall stress field within the joint and how that affects the joint's fatigue life to damage initiation, N_i, a fatigue performance indicator of the study. It has been discovered that changing the tolerances within the splices provides little influence on the stress field within the splice, which resulted in several iterations of the splice design approaching smaller and more lightweight joint alterations. The designs showed excellent durability characteristics when compared to the Limit of Validity (LOV) cycles set by the aviation authorities, such as EASA and FAA. The Finite Element (FE) model was able to accurately depict the stress field within the splice, validated by the experimental data through strain fields captured using Digital Image Correlation (DIC) technique, and consequently accurately pointed to the location of damage initiation, which in all cases was the outer-most overlap on the flush side of the joint. Along with the adapted predictive numerical model it was possible to predict the damage initiation lives in the spliced specimens with a blunt notch. The predictions in the samples without the notch resulted in far lesser agreement with experiments. This was likely caused by to the limitations of the model,

which only took into account quasi-static loading without damage and is highly dependent on the reference data used.

It was concluded that splices can be designed smaller and lighter than previously done due to the tighter tolerances allowed within the splice. Overlaps of 5 mm in both the unnotched butt splice and the unnotched overlap splice, however, resulted in an alternative damage progression mode, specifically a complete delamination of the external overlap rather than metal fatigue cracking. This is attributed to the rising average shear stress in the adhesive. Regardless, the smallest and lightest iterations of the butt splice and the overlap splice with 5 mm overlaps and gaps between aluminium interruptions were able to withstand 600,000 cycles while loaded at $S_{max} = 120$ MPa, at stress ratio of $R = 0.1$, without onset of damage, suggesting an even larger fatigue life. The updated versions of both splice types are said to possess an excellent durability, but it is hard to draw a concrete conclusion on the damage tolerance of the updated designs due to alternative damage modes and lack of research thereof. While both splice types were deemed to be successful in their role of a joining structure, the butt splice was concluded to be superior to the overlap splice when it came to fatigue performance, consistently developing visible damage later than the overlap splice. This gap in fatigue performance is expected to expand if thicker layers or larger number of layers are to be considered. This is because of the secondary bending which occurred in the joint, more so for the overlap splice than the butt splice judging from FEA results and experiments.

It is recommended that a more extensive FE model is developed using the model built in this research as a foundation. The current model could be expanded in several ways, such as simulations of damage progression, individual modelling of the uni-directional fibres, fibre failure models, and a curing simulation. This will improve the validity of the methodology, specifically concerning the unnotched splice specimens, and improve the predictions of not only initiation lives, but also failure lives.

Table of Contents

List of Figures

List of Tables

Nomenclature

List of Acronyms

ARALL	Aramid Reinforced Aluminium Laminate
BS	Butt Splice
CA	Constant Amplitude
CARALL	Carbon Fibre Reinforced Aluminium Laminate
CLT	Classical Laminate Theory
CZM	Cohesive Zone Model
DIC	Digital Image Correlation
DOF	Degrees Of Freedom
EASA	European Aviation Safety Agency
FEA	Finite Element Analysis
FE	Finite Element
FEM	Finite Element Method
FML	Fibre-Metal Laminate
FRP	Fibre-Reinforced Polymer
ML	Metal Laminate
GLARE	Glass Reinforced Laminate
GFRP	Glass Fibre Reinforced Polymer
LEFM	Linear Elastic Fracture Mechanics
OS	Overlap Splice
SFT	Self Forming Technique
UD	Uni-Directional

List of Symbols

Greek Symbols

α_t	Coefficient of thermal expansion
β	Geometry factor
ν	Poisson's ratio
σ_{base}	Internal stress in the metal layer of the base laminate
σ_{II}	Mode II stress
σ_I	Mode I stress
σ_{nom}	Nominal stress
σ_{peak}	Peak stress

Latin Symbols

a	Crack length
d	Hole diameter
D_i	Damage initiation parameter
E	Young's Modulus
K	Stress intensity factor
K_t	Stress concentration factor
$K_{bridging}$	Stress intensity factor due to fibre bridging
$K_{farfield}$	Stress intensity factor due to far field stress
$K_{t,notch}$	Stress concentration factor due to a notch
$K_{t,S-N}$	Stress concentration factor of the reference curve
$K_{t,splice}$	Stress concentration factor due to a splice geometry
$K_{t,total}$	Total peak stress concentration in the specimen
K_{tip}	Effective stress intensity at the crack tip
N	Number of cycles
R	Stress ratio
R_{nom}	Nominal stress ratio
R_{S-N}	Stress ratio of the reference curve
S_k^{th}	Thermal stress
S_a	Stress amplitude
$S_{a,corr}$	Corrected stress amplitude in the reference curve
$S_{a,S-N}$	Stress amplitude in the reference curve
t	Thickness of the laminate
U	Translational degree of freedom in ABAQUS
UR	Rotational degree of freedom in ABAQUS
W	Specimen width

Subscripts

ff	Far field
f	Failure
II	Mode II crack opening
I	Mode I crack opening
i	Initiation
k	Layer code in a laminate
max	Maximum
min	Minimum
nom	Nominal

Chapter 1

Introduction

Fibre Metal Laminates (FMLs) have been utilised in aircraft for several decades, with the most notorious application of this material being the Glass Reinforced Laminate (GLARE) fuselage panels of the A380. This application was motivated by the loading experienced by the front and rear of the fuselage, which is primarily fatigue loading of the ground-air-ground cycle due to pressurisation and depressurisation. Due to their laminated structure and high-strength yet lightweight materials, FMLs suited perfectly for such applications. Unfortunately, with it came challenges that did not appear in monolithic metal alloy structures, namely joining methods. To avoid mechanical fastening, which is known to have negative effects on fatigue performance and fibre strength, a special type of joint has been designed called the splice joint. It allowed to elegantly join GLARE panels and create even larger flush panels for the crown of the fuselage in aft and stern of the aircraft [2].

Mainstream research of the splice joint has been partially put to a halt as the A380 aircraft have been successful in operation since 2005 with the overlap splice holding the GLARE fuselage skin panels together. Nevertheless, there remains potential to improve and optimise the joint and promote it as a primary way to join FML panels. Splices contain a lot of features and geometries and at least three distinct materials, and therefore have a lot of room for mechanical improvement. In particular two splice designs were chosen, the aforementioned overlap splice, and the butt splice - a splice that was expected to be a close match or even outperform the overlap splice when it comes to durability and damage tolerance [3]. To constrain the research to fit the nominal timeline, the splice design domain was limited to parameters within the splice since it was previously discovered that the splice joint is heavily dependent on its internal features [6]. To provide a methodology that can be used to numerically evaluate the performance of such splices, a numerical method has been adapted from that of Spronk et al. [12], that is hypothesized to predict both location and lifetime of damage initiation within the splice. Naturally, the main question of the research is:

How do the splice tolerances affect fatigue life performance of a complete splice?

To guide the research towards to the answer to the above question, the following sub-questions were set:

1. Is it possible to accurately predict the location and lifetime of damage onset in spliced Fibre Metal Laminates?
2. Which splice configuration possesses superior mechanical performance - the overlap splice or the butt splice with external doubler straps?
3. What design guidelines shall be followed when designing splice joints in FMLs, aimed for improved fatigue performance?

The solution to the above problem is expected to further prove the potential of the splice joint, validate the methodology used to evaluate the newest splice configurations for any future use, and provide generic splice design guidelines that would aid in the development of this joint type in the foreseeable future. To effectively advance to this solution, a multi-disciplinary approach was used. This approach involved:

- **Finite Element Analysis (FEA)** of the splice joints used both as a design tool and as a analysis tool that helped point to vulnerable locations in each of the configurations studied and quantify the changes in the stress field with changing geometrical parameters.
- **Numerical predictive model** that was adapted from older models, primarily the model described in the paper of Spronk et al. [12], to quantitatively evaluate the fatigue performance of each splice configuration by utilising data extracted from FEA and reference S-N curves.
- **Experimental testing** to both evaluate performance of the splices without reliance on the models built, as well as analyse damage progression and validate the preceding models used in the design of the splices.

The structure of this thesis report is as follows. Chapter 1 is the current chapter which contains a brief introduction and the research questions. Chapter 2 provides the reader with background on the topic via a literature review conducted prior to the start of this research. Chapter 3 provides a detailed description of the methodology used and Chapter 4 presents numerical investigations of splice details and suggests final splice designs to be experimentally evaluated. Chapter 5 describes the test set-up used during the course of the experimental program and briefly explains coupon design and manufacturing. Chapter 6 showcases experimental results and their respective evaluation. Finally, Chapter 7 provides closing thoughts on the study, as well as recommendations for future research.

Chapter 2

Literature Review

This chapter is a compact version of the literature study done prior to the start of the main research phase of this thesis. Section 2.1 briefly describes the history of FMLs and their relevance in the aviation industry. Section 2.2 introduces the splice joint concept and Section 2.3 talks about the investigations done on this joint in the past. Section 2.4 outlines the most important fatigue and failure mechanisms in the splice and FMLs and finally, Section 2.5 summarises the literature study by providing the research questions.

2.1 Brief history of FMLs

Fibre-Metal Laminate (FML) is a hybrid material, consistent of alternating metal and Fibre-Reinforced Polymer (FRP) layers that are bonded together [2]. From the applications of bonded aluminium sheets in production of Fokker F-27 it was already known that laminated materials and structures possess crack stopping capabilities. Schijve et al. [17] quantitatively studied this effect in Metal Laminate (ML) sheets. It was observed in both through and part-through cracks that crack growth was much slower in MLs than in monolithic aluminium alloys. Later on, FRPs were introduced into the metal laminates for weight saving purposes, and in 1981 a patent was filed on FMLs, with Schijve, Vogelesang and Marissen being credited as its creators [2]. Apart from the advantageous weight reductions and outstanding fatigue performance, FMLs showed other attractive qualities, such as high specific static properties, excellent impact resistance, burn through resistance, and even corrosion resistance [18].

From thereon, FMLs became a topic of interest in the academic world as well as the industry. The pioneering FML grades that saw significant industrial applications are Aramid Reinforced Aluminium Laminate (ARALL) and Glass Reinforced Laminate (GLARE), where ARALL was most notably used for the cargo doors of C-17 and resulted in 27% weight savings[1] [19], and GLARE in particular has seen tremendous industrial success with the Airbus A380 program, where it was implemented into the crown section of the fuselage [2, 18]. GLARE

---

[1] Only about 30 aircraft were built with the ARALL cargo door before the material was deemed to be too cost inefficient [2].

is also utilised in the reinforcement straps in the A400 wing attachment frames, specifically for its damage tolerant properties [20, 21]. In total, 4 standardised ARALL grades have been developed and 6 standardised GLARE grades, the overview of which can be found in Table 2.1 in the book of Alderliesten [4]. By varying the FRP layup or the constituent materials, each grade was tailored towards a specific application, for instance longitudinal versus transverse strength, off-axis strength, or prioritised fatigue performance over static strength.

The ability to vary constituent materials, layups, manufacturing techniques, and dimensions provided an opportunity for researchers to study ways to add to this novel material class, resulting in many new FMLs. Sinmazçelik et al. [22] and Ding et al. [23] summarised existing FML grades and outlined a spike in interest in this material class because of an increase in automated manufacturing metallic like materials, which FMLs are when manufacturing is concerned. Additionally, investigations on natural fibre-metal laminates are starting to take place, targeting the automotive industry, according to Ishak et al. [24], the research largely motivated by the reduction of the ecological footprint in mass vehicle production.

The automotive industry is not solus in its venture to employ more FML structures, be it natural flax FMLs or more traditional FMLs, like GLARE and Carbon Fibre Reinforced Aluminium Laminate (CARALL). Industries such as aviation, space, and even maritime industries are also looking to employ the material in their structures [4, 22, 23]. Christian Ruckert, head of Research & Technology Integration for Materials and Processes at Airbus stated that GLARE will see growth in future aircraft. He attributed this prediction to the recent changes in automation, making it "lower cost vs. straight composites", which falls in-line with discussions of Ding et al. [23, 25]. This renewed industrial interest in FMLs calls for research & develoment of new FML grades, new manufacturing techniques, recycling, and improved ways to join FML structures.

2.2 The splice joint

Amidst of the development of the Airbus A380, challenges arose with regards to manufacturing of large GLARE panels that were meant to compose the upper aft and forward sections of the fuselage, see Figure 2.1. Production of aluminium panels was limited to 60 inches in width, or 1524 mm, which meant that additional joining steps were necessary to accommodate for the large diameter of the A380 fuselage [26]. To tackle this issue, the splice joint concept was created. The splice joint the involved aluminium sheets joined at the their interruptions, with prepreg layers running continuously through the joint, uninterrupted. For visual aid see Figure 2.2. The adhesive system used to fill the gaps in the splice joint is the same adhesive that was used to pre-impregnate the Glass Fibre Reinforced Polymer (GFRP). Carl Garasché is credited as the main inventor of the splicing concept [2].

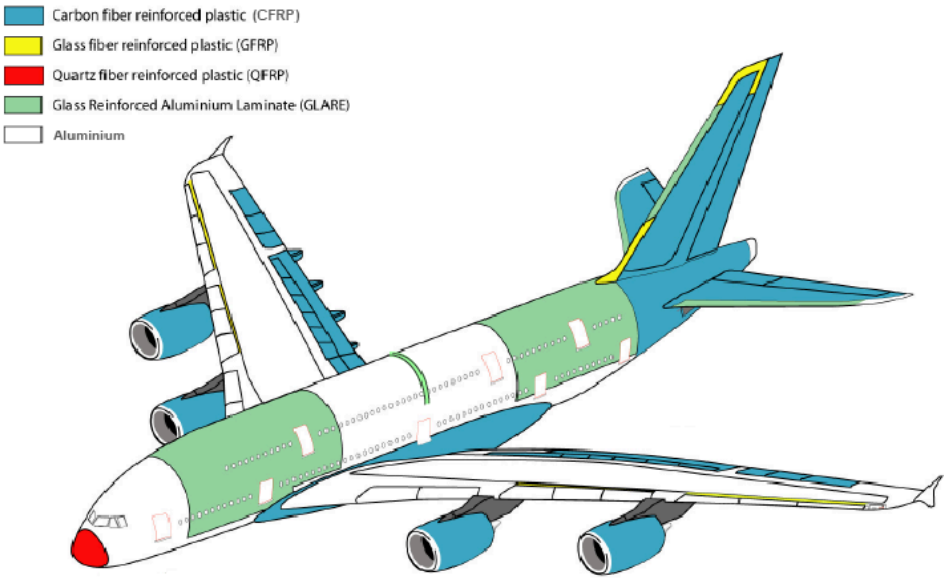

Figure 2.1: Exterior material breakdown in the Airbus A380 [1].

Vermeeren et al. [26] suggested a few qualitative design guidelines for splice design, such as maintaining the advantages of the base laminate, keeping the weight and cost to a minimum, ensuring the same net-section properties as in the base laminate and having a smooth facing on the outer skin. These design guidelines, however, remained rather general and only aided in the conceptual design of a splice.

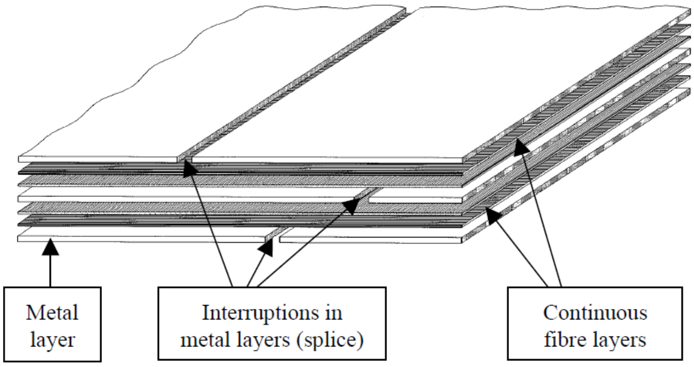

Figure 2.2: The original butt splice configuration [2].

Many other researchers expanded these guidelines with numerical, analytical, and experimental investigations, which resulted in numerous splice configurations, seen in Figure 2.3. The concept shown in Figure 2.2 and Figure 2.3(**a**) resulted in delamination of the outer layers when the stress in the direction transverse to the splice direction[2] would exceed over 400 MPa [2]. This configuration was modified by adding doublers on both sides of the panel to prevent delamination, illustrated in Figure 2.3(**b**). This however, required two curing cycles,

---

[2] Splice direction defined as the out-of-paper direction when looking at the splice cross-section, like in the case with this document.

first to cure the splice itself and then to cure the doublers, driving the production costs up. Along with the splice, a special FML production technique was invented, called the Self Forming Technique (SFT). SFT essentially meant that the splice was let to form on its own under the pressure of the autoclave, although this meant that the technique is reliant on the relative low stiffness of the sheet prior to curing, largely dictated by the stiffness of the aluminium layers. This put a limitation to the thickness of such layers to 0.4mm[3] [27]. This technique lead to configurations **(c)**, **(d)**, and **(f)** in Figure 2.3, the latter two being the inventions of Beumler from Airbus [28]. Figure 2.3 **(f)**. It is the overlap splice **(d)** configuration that was first implemented in the Airbus A380 program. Cracks were later discovered in the resin-rich area of this splice configuration, and therefore Figure 2.3 **(f)** was implemented to shield the resin-rich area from the environment and prevent crack initiation[4]. The welded splice, Figure 2.3**(e)**, was deemed infeasible due to uncertainty in weld quality of such joints [29].

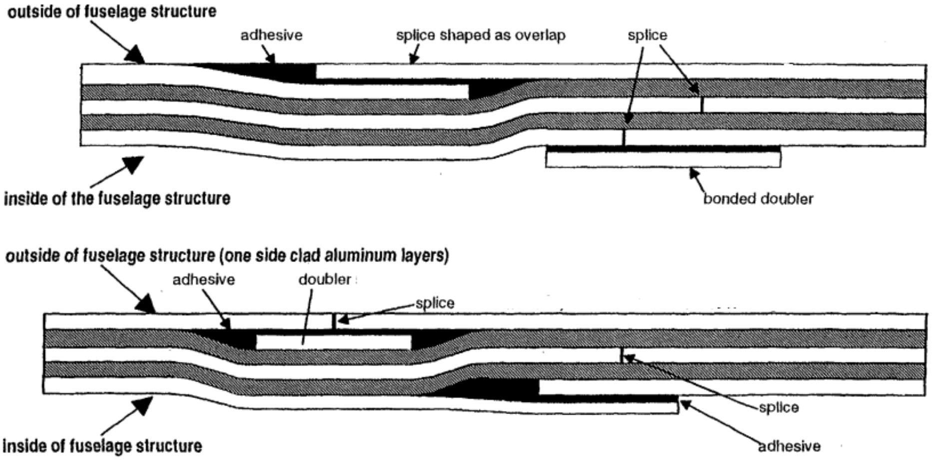

Figure 2.4: Alternative splicing configurations invented by Roebroeks, utilising SFT [3].

Roebroeks [3,30] proposed more designs, such as the ones shown in Figure 2.4. The top splice in Figure 2.4 is an alternative to Figure 2.3 **(c)**, but with an overlap strap instead. This configuration posed an issue, however, as many airliners prefer what is called a 'bright-skin aircraft' [3]. This means that the outermost aluminium layer that is exposed to the environment must be of clad aluminium alloy, and it is undesirable to place it over large adhesive bonds. The reason lies in micro-damage in the clad layer that can cause moisture ingression, leading to corrosion damage of the resin rich areas of the joint that can no longer be inspected due to the obstructing clad layer. The bottom splice in Figure 2.4 solves this problem by minimising the exposed resin area and eliminating the overlap of the clad aluminium layer.

---

[3] Thinner aluminium sheets are also available, like ones with 0.2mm thickness, however these pose a challenge in handling [27].

[4] From personal discussions with Jan Willem Gunnink, the co-editor of "Introduction to Fibre Metal Laminates" [2] and CEO of GTM Advanced Structures.

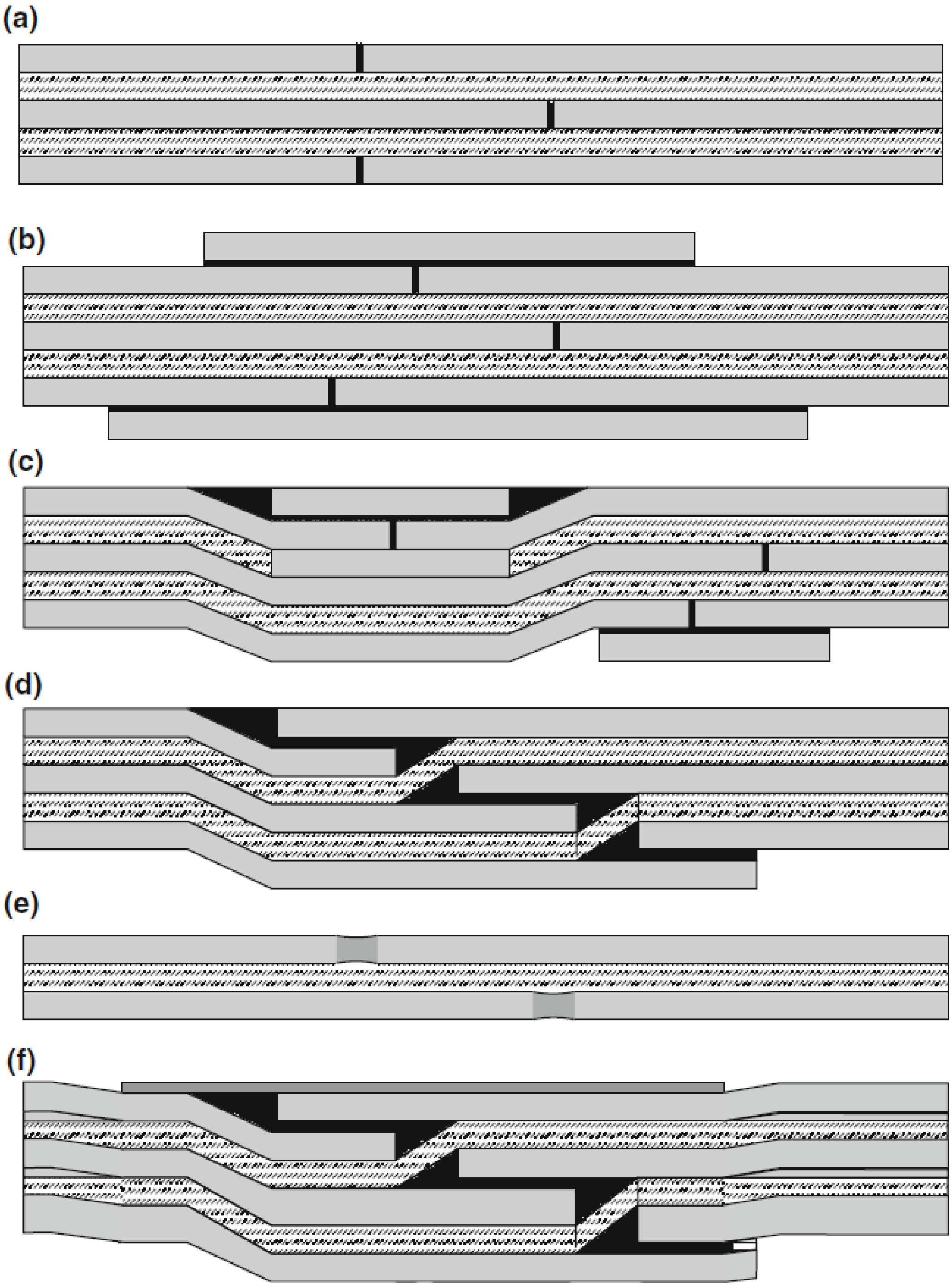

Figure 2.3: Different configurations of splicing of FMLs: **(a)** butt-joint, **(b)** doubler-butt-joint, **(c)** splice doubler joint, **(d)** overlap splice joint, **(e)** welded butt-joint, **(f)** reinforced overlap splice joint. Adapted from [4].

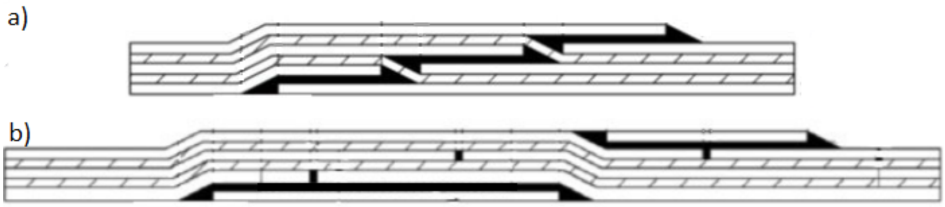

Figure 2.5: (a) Airbus overlap splice, **(b)** GTM butt splice.

Despite numerous variations of the splice joint, several remain as the 'optimised' versions of the splice. The examples of these are shown in Figure 2.5. Figure 2.5**(a)** is the overlap splice employed by Airbus in the A380 program, and Figure 2.5**(b)** is an alternative butt-splice design put forward by the GTM Advanced Structures, the collaboration company of this research master thesis.

2.3 History of splice investigations

Looking closely at the aforementioned splice designs, it is evident that a splice joint contains multiple structural features, such as butt joints between the aluminium plates, overlaps, and internal / external reinforcement doublers. Therefore, it was proposed to treat a splice not as a unique joint, but as a collection of joints or common joint features [30]. It was further proposed that these features are expected to behave similarly when it comes to damage mechanisms, regardless of the configuration they are present in. This assumption simplified research of the splice, as it allowed to isolate the splice features and draw conclusions on the performance of each one individually and subsequently devise design guidelines for the FML splice joint. Such investigations are thoroughly laid out in the review of Hooijmeijer [6], a brief summary of which follows below.

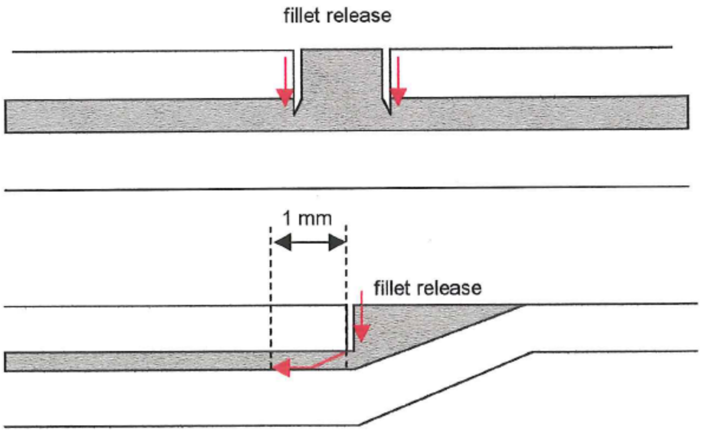

Figure 2.6: Fillet release within the splices caused by CA fatigue loading [5].

De Ruyter [7] tested the complete splice configurations as well as internal and external doubler run-outs. During fatigue tests, fillet release has been observed under lower stress levels, and at higher stress levels delamination of the external doubler was observed, which later initiated a metal fatigue crack in the adjacent aluminium layers, see Figure 2.7.

A similar fillet release was also observed by Hooijmeijer [5], after the splices were subjected to $S_{max} = 120$ MPa fatigue loading, see Figure 2.6. No further fatigue damage was observed.

Van Tongeren [31] used Finite Element Method (FEM) simulations to study stress states of splice details and determined the distances it takes to redistribute the stress around the splice detail back to undisturbed stress levels. He came up with a design guideline to place the splice details at least 20 mm apart, although he noted that in presence of secondary bending the stress disturbances span larger areas and that this phenomenon should be taken into account during the design.

Out [32] in his thesis investigated the tolerances that result from the manufacturing process that later affect the mechanical performance of splices. His testing was focused more on static properties with few fatigue tests being performed, which were deemed inconclusive in the end. It was concluded that tolerances do not influence ultimate or blunt notch strengths but it is the sheer presence of the splice joint that reduces static strengths.

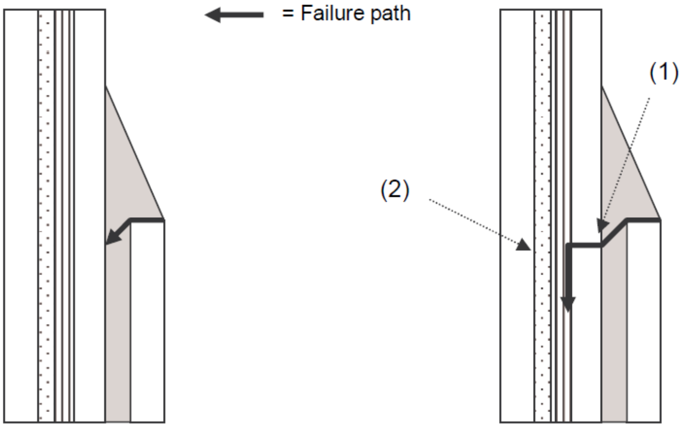

Figure 2.7: Damage progression of an external doubler loaded in fatigue. **(left)** first load case at $\sigma_{max} = 120$ MPa for 180k cycles causing a fillet release. **(right)** second load case at failure path $\sigma_{max} = 150$ MPa for 90k cycles, failure of the first aluminium layer and subsequent delamination [6, 7].

Overall, tests showed that mechanical properties of splices are better than expected and that fatigue performance of the complete splices is excellent. It was recommended to focus investigations on fatigue tests of complete splices with notches at various critical locations. This way a sensitivity study of notch location and presence could be performed, and moreover this allows to study fatigue behaviour of splices with open holes [6].

2.4 Fatigue and failure mechanisms in splices

Any structure subjected to cyclic loading is susceptible to fatigue damage and therefore has a fatigue life, typically characterised by the $S-N$ curves, or Wöhler curve, where S is S_a, the stress amplitude and N is the number of cycles [33]. Yet, it does not mean that every structure

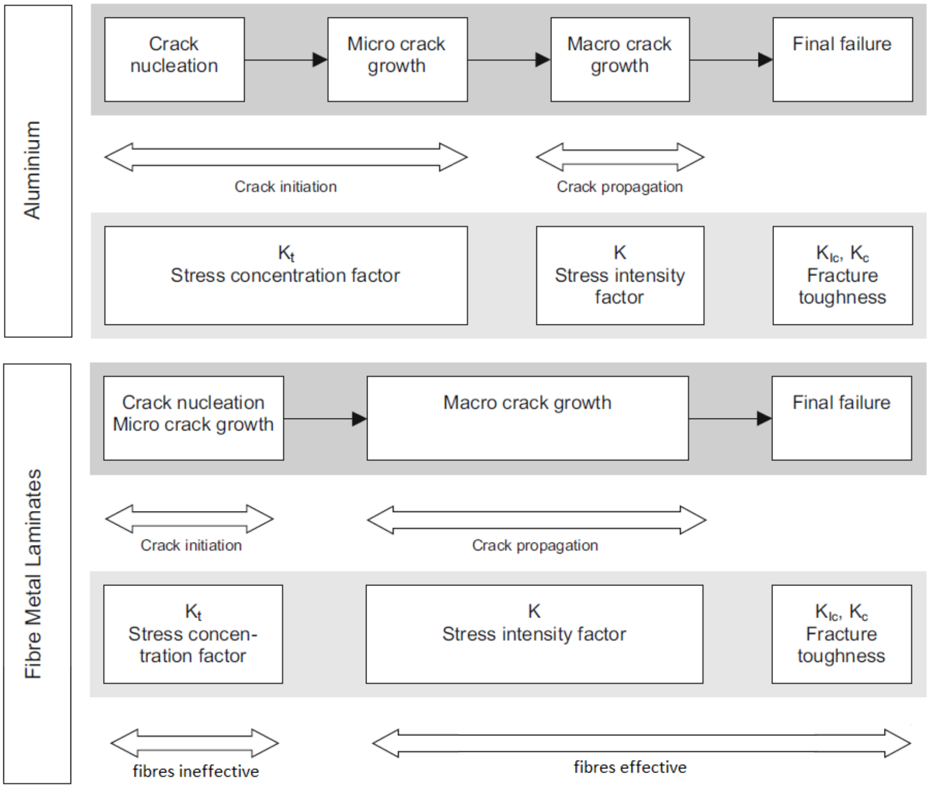

Figure 2.8: Different phases of fatigue in FMLs vs. metals. Adapted from [4, 8].

under the same type of loading, whether it be low amplitude high frequency loading or high amplitude low frequency loading, will behave and respond the same to the respective loading. The response of the structure depends on its geometry and more importantly the material it is made out of. The cause for this difference is related to how the damage in the material is initiated and later propagated through it. Fibre-metal laminates, being a hybrid material, combine three different materials with different behaviours and characteristics, resulting in a unique fatigue response, described in detail in the following subsections.

2.4.1 Crack initiation in metal constituent

In metals, majority of fatigue life is spent in crack initiation phase, characterised by the stress concentration factor, K_t, defined as:

$$K_t = \frac{\sigma_{peak}}{\sigma_{nom}} \tag{2.1}$$

where σ_{peak} is the peak stress, and σ_{nom} is the nominal stress [33]. Generally, crack initiation is difficult to predict due its sensitivity to external factors, causing scatter in experiments with seemingly identical testing environments [33].

Crack initiation in FMLs is considered to occur in the metal layers, and it is safe to assume that crack initiation behaviour in metal sheets of FMLs is the same as in monolithic aluminium sheets as there is no scientific evidence to suggest otherwise [4,8]. Unlike metals, however, the crack initiation phase in FMLs is brief with respect to the crack growth phase, see Figure 2.8, due to the extended crack growth in FMLs, explained in more detail in subsection 2.4.2. The assumption that initiation in both materials starts within the metal layer means that the number of cycles to crack initiation can be predicted using the existing data gathered from the $S - N_f$ curves of aluminium specimens, as long as the stress in the actual aluminium layers is used, which straightforwardly calculated using Classical Laminate Theory (CLT) [8]. Although $S - N_f$ curves demonstrate the number of cycles to *failure*, hence the subscript $_f$, the crack growth period is very short in metal specimens and equating $S - N_i$ of FMLs to $S - N_f$ of metals will lead to an error, yet this error is assumed to be quite small [8].

Homan [8] utilised this assumption and adapted the stresses within the metal layers in such a way that the initiation life in FMLs could simply be read of existing S-N curves of aluminium sheets.

Spronk [12] developed this methodology further and built on the model of Homan [8]. Both of the mentioned models neglect interlaminar shear because it does not play part in fatigue crack initiation, which means that this formulation completely disregards possible initiation in the bond line. Therefore, it is important to keep the capabilities of the model in mind, as it may lead to wrongful predictions if the geometry is prone to delaminating first, rather than initiating a fatigue crack, as is often the case in external doublers [30]. Spronk also suggested that in cases where the laminate is unbalanced or asymmetric, FEM should be used in order to evaluate stress concentrations at point of interest [12]. Since the research is focused on the splice joint, which is technically an asymmetric and an unbalanced laminate, it is beneficial to follow the aforementioned suggestion and turn to FEM for stress evaluations.

FE modelling of FMLs is not a novel research domain, with multiple examples available in the literature. Smolnicki et al. [34] conducted a comprehensive review on FEM simulations of FMLs. They state that a lot of the methods can be borrowed from simulations of classical laminates, however that depends on what event is being modeled exactly. A number of researchers even conducted simulations on spliced laminates like Sugiman and Crocombe [35], who employed a progressive damage FEM coupled with Cohesive Zone Model (CZM) on spliced ML and FMLs bonded to a stringer and studied fatigue in aluminium layers and in the interfacial bonds. Al-Azawwi et al. [14] focused on delamination only and employed a very similar method to Sugiman and Crocombe [35], except for differences in geometry tested and the traction-separation model used. Zhu et al. [15] performed static failure analyses on spliced CFRP laminates. They used cohesive zone elements (COH3D8) in ABAQUS in order to study the interlaminar behaviour under tensile loading and the VUMAT subroutine to model the damage evolution based on a principle of stiffness degradation. After analysing the existing literature, it became evident that simulating fatigue damage progression in FMLs is difficult and expensive. Most models focus on a specific damage mode, like mixed-mode delamination or metal fatigue, but rarely do they take all damage modes into consideration. Sugiman and Crocombe [35] give a complete model for fatigue damage in FMLs, but the model requires calibration of material property and cohesive damage parameters against experimental data, which limits the validity greatly.

Fortunately, when it comes to quasi-static simulations, more applicable models with promising results are present. Smolnicki and Stabla [36] and Zhu et al. [15] for example have utilised FEM to simulate static deformation and failure within FMLs and composites, showing excellent agreement with experimental results.

2.4.2 Crack growth and delamination

When the micro-crack reaches the transition crack length, usually taken at 1mm for statistical accuracy [4], crack growth period begins, which is characterised by the stress intensity factor, K, defined as:

$$K = \beta \sigma_{nom} \sqrt{\pi a} \tag{2.2}$$

where β is a geometry factor and a is the crack length. This way of characterisation of crack growth is a feature of Linear Elastic Fracture Mechanics (LEFM), and in metals is often the only thing one needs in order to find the crack growth under the specified fatigue loading, due to majorly elastic behaviour in fatigue stress levels, leading to good understanding of the underlying physical phenomena and therefore accurate predictions [33].

In FMLs, however, the behaviour is not as simple, as at the transition from crack initiation to crack growth, the hybrid nature of FMLs plays an important role. The presence of fibres retards the crack growth by providing a load transfer path, consequently reducing K and restraining crack opening [37]. This phenomenon is referred to as fibre bridging, graphically explained in Figure 2.9. This means that crack growth is no longer just a function of the nominal stresses induced within the specimen, but also the local bridging affects caused by the fibers, formulated as such [4]:

$$K_{tip} = K_{farfield} + K_{bridging} \tag{2.3}$$

where K_{tip} is essentially a superposition of far field stress intensity factor, $K_{farfield}$, and the stress intensity factor caused by the bridging, $K_{bridging}$, which in fact is negative. Because of this, the crack growth period becomes more significant in the overall fatigue life of these materials. This is again depicted in Figure 2.8, where the crack propagation takes up a larger portion of the specimen's fatigue life than crack initiation, which is exactly the opposite for the fatigue life of metal specimens. The transition between fibre effectiveness occurs roughly at the same crack length as micro-to-macro crack growth transition, although two phenomena have not shown to be physically related [8].

Followed by metal crack growth comes interlaminar delamination. The load transferred from the cracked metal layers cause excess in shear or peel stresses, causing the adhesive to tear and the laminae to separate from one another - in other words delaminations. Delaminations resulting from excessive peel stresses are called to be of Mode I type, and those resulting from excessive interlaminar shear stresses are called to be of Mode II type, illustrated in Figure 2.10 [4]. In base laminates, i.e. unspliced laminates, it is generally accepted to consider only Mode II type interlaminar delamination, however, that is not the case in spliced samples. The presence of assymetry and therefore eccentricities in the splice joint induces secondary bending, promoting a mixed-mode delamination or disbonding [38].

Surprisingly, delaminations can be both advantageous and disadvantageous. On one hand, large delamination zones can cause insufficient load transfer between the layers, worsening the stress situation within the material, eventually leading to failure [37]. On the other hand,

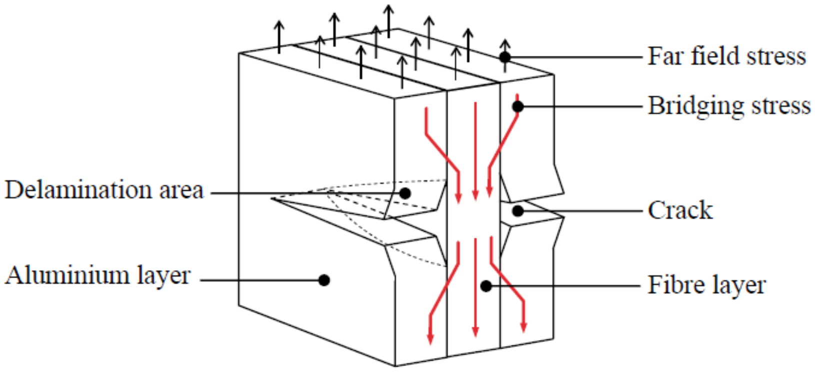

Figure 2.9: Fibre bridging effect along with the delamination of the constituent layers. This image assumes a fatigue through crack. Courtesy of [8, 9].

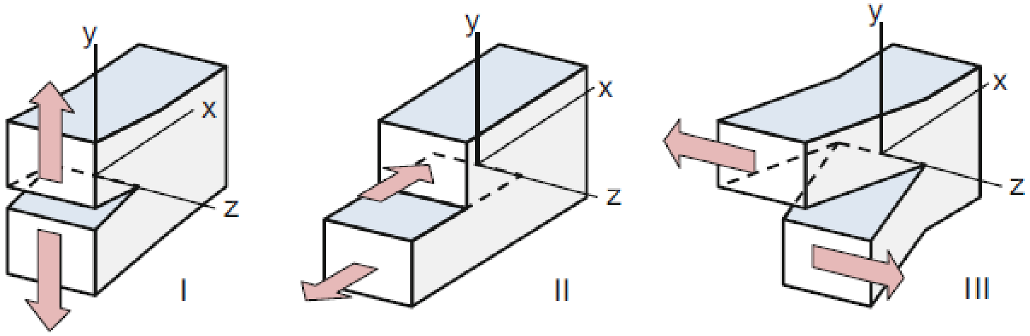

Figure 2.10: Depictions of the three crack opening modes. Courtesy of Alderliesten [4].

they reduce the bridging stress and therefore prevent fibre failure. This advantageous effect of delamination on fibre strain in combination with the bridging effect causes a linear crack growth, i.e. a constant crack growth rate, a unique feature of FMLs [4, 8, 37]. To put it in perspective, GLARE crack growth is compared with 2024-T3 in Figure 2.11.

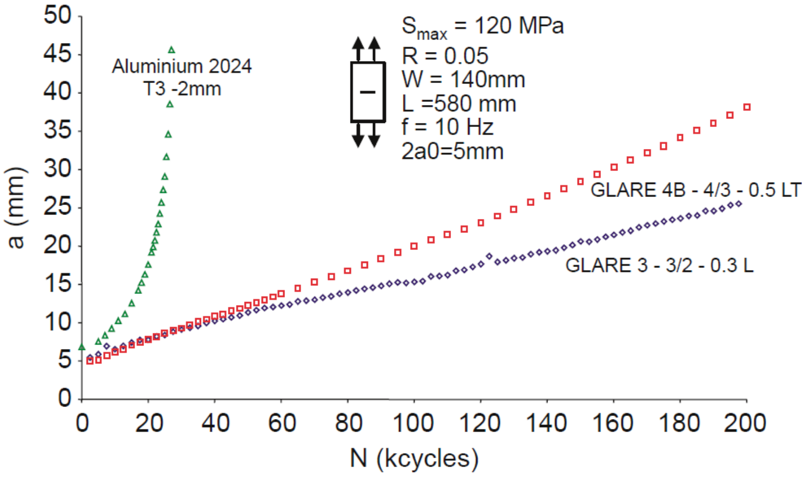

Figure 2.11: Crack growth comparison between GLARE and Aluminium 2024-T3 [8].

Multiple models exist that predict crack and delamination growth in FMLs, such as the Alderliesten model [39] for crack propagation and delamination propagation in GLARE, uniquely without any fitting parameters and Wilson model [40], built upon the Alderliesten model [39], adapting the model to include variable layer thicknesses, different laminae materials, varying crack lengths within the laminate, as well as coupled bending and axial loading. Other extended crack growth models exist that include crack directionality [41,42]. Regardless, these models have been constructed to tackle crack and delamination growth within uninterrupted FMLs, hence their validity when it comes to splices is limited. Splices introduces irregularities within the laminate, which in hand cause secondary bending moments, the impact of which is difficult to evaluate analytically due to the irregular geometry of the splice.

2.4.3 Adhesive disbond initiation

While delamination and disbond are very similar when it comes to mechanical behaviour and damage propagation, when looking at splices, it is useful to differentiate between the two [43]. Delamination hereby refers to the interlaminar delamination within the base laminate or the bulk of the splice, and disbond refers to the disbond of the reinforcement doublers and resin fillers between the splice interruptions.

It is difficult to compare the splice to other commonly found adhesive joints, such as the lap shear joints, scarf joints, or strap joints, as the splice is rather a collection of adhesive joints. Moreover, disbond initiation is often ignored as it is difficult to predict and does not always lead to further damage propagation [6,44]. In the splices, however, it is likely that the onset of fatigue damage would present itself as a disbond rather than metal crack nucleation, like showcased in Figure 2.6 and Figure 2.7. To predict the initiation of such damage, a quadratic damage initiation criterion is often used, which is a maximum stress damage criteria:

$$\left(\frac{\langle\sigma_I\rangle}{\sigma_{I,crit}}\right)^2 + \left(\frac{\sigma_{II}}{\sigma_{II,crit}}\right)^2 = D_i \geq 1 \tag{2.4}$$

where σ_I is Mode I opening stress[5], such as peel or tensile, σ_{II} is the Mode II opening stress, like shear, and D_i is the damage initiation parameter. Critical stress values are chosen depending on the failure mode of the material. While for metals this is often yield strength, for adhesive this is often failure strength and has been used by multiple researchers in the recent years [14,45,46].

2.5 Research questions

From the past developments and tests, it became clear that fatigue performance of splices is excellent if no prior damage is present. Static properties have also been studied extensively, including static strengths, blunt notch strengths, residual strengths as well as crack extension behaviours. It was concluded that it is the presence of splices and notches that defines the static strength of the splice, irrespective of their dimensions. However, fatigue performance

---

[5] The Macaulay brackets "$\langle\rangle$" indicate that only positive (tension) stress is taken into account since it is the one that would contribute to damage initiation and not compressive axial stress.

has not received as much attention, most likely due to the fact that early tests showed that even the weakest of the splice designs performed well in fatigue. It is hypothesized that the change in internal splice dimensions may trigger different damage modes within the joint, or result in different fatigue initiation periods. Therefore, it would be beneficial to conduct investigations on how such splice details and their variable geometries affect fatigue performance of the splice. To evaluate this performance, primarily damage initiation is taken into account due to an industrial point of view. Knowing damage initiation lives and modes can aid in scheduling of maintenance and repair. The result of the proposed investigation would lead to splice design guidelines when designing against fatigue. To formulate this, the following research goal is put forward:

Main question: How do the splice tolerances affect fatigue life performance of a complete splice?

To help accommodate this research, the main question is further broken down into smaller sub-questions:

Sub-Question 1: Is it possible to accurately predict the location and lifetime of damage onset in spliced Fibre Metal Laminates?

To answer this question, an FE model is going to be built. With this model, it would be possible to not only analyse stresses within a single splice detail, but to also compare stresses of splice details that are subjected to the same far-field loads. By having a complete model, it would be possible to study peel and shear stresses within the adhesive in different configurations, which can given an insight into fatigue onset within the adhesive layer. In addition, such a model will give internal stresses within the metal constituent, making it possible to extract the stress concentration factor that can then be used to evaluate fatigue life to crack initiation using the aforementioned predictive models.

Sub-Question 2: Which splice configuration possesses superior mechanical performance - the overlap splice or the butt splice with external doubler straps?

In order to draw a conclusion on the superior splice design, both FE and experimental results are going to be taken into account. Such investigations will quantify the properties of each splice and their respective variations, as well as point out any weaknesses or strengths of the design. A trade-off will be performed based on fatigue performance, but also on manufacturability and weight of the splice configuration. Based on the answers to the previous questions, it would be possible to derive splice design guidelines, which can then be used as to create FML joints in form of splices in structures where fatigue is of concern. Therefore the third and final sub-question is as follows:

Sub-question 3: What design guidelines shall be followed when designing splice joints in FMLs, aimed for improved fatigue performance?

Answering all of the above questions will aid in the future design approach to splice joints and joints of similar nature, such as adhesive joints in laminated structures. Although in this study the aircraft applications are taken as reference, the results of this thesis will benefit design of any FML structures where fatigue loading is a concern.

Chapter 3

Numerical & Finite Element Modelling

This chapter serves as a detailed description of the models built and used in this research, such that the models are easily comprehensible and reproducible. It is separated into four sections, section 3.1 briefly describing the basics of the methodology used, section 3.2 in detail provides the blueprint to the Finite Element Model built in ABAQUS, and section 3.3 outlines the adapted model of Spronk et al. [12] to predict fatigue initiation lives in FMLs. Lastly, section 3.4 talks about the limitations of the overall methodology described in this chapter.

3.1 Methodology

As mentioned in Chapter 2, the splice designs under investigation are depicted in Figure 2.5. One of the designs, the overlap splice in Figure 2.5 **(a)**, have been proven to comply with the operational requirements and have been implemented in the Airbus A380 fuselage structure [2]. Nevertheless, it remains unclear under which guidelines exactly the geometry was proposed and designed, and whether it is an optimal structural solution to the fatigue loading faced by the aircraft. Therefore, to establish clear design guidelines that could lead to an improved design, the geometries, i.e. overlap lengths, butt widths, strap widths, are challenged and investigated.

Looking closely at the splice designs in Figure 2.5 it is possible to pick out several distinct splice features and label such features, refer to Figure 3.1. Going forward, the Figure 2.5**(a)** will be abbreviated to as the Overlap Splice (OS), and Figure 2.5**(b)** to as the Butt Splice (BS). The features are described in Table 3.1 for future reference and to avoid confusion. Employing the assumption that the isolated details induce the same mechanical behaviour, like stress concentrations, when isolated as in a complete splice allows to pinpoint critical fatigue locations in each of the details and compare the influence of such features on the complete structure. Therefore, to investigate this influence of a certain feature on a complete splice, FE investigations on samples with variable dimensions of features laid out in Table 3.1 are conducted. While features '**a**' and '**d**' are possible to study individually, for features '**b**', '**c**', and '**e**' a more complete splice is necessary. Note that feature '**d**', the external overlap, exists as an overlap that is flush and non-flush with the base laminate. Therefore, these are going to be investigated separately.

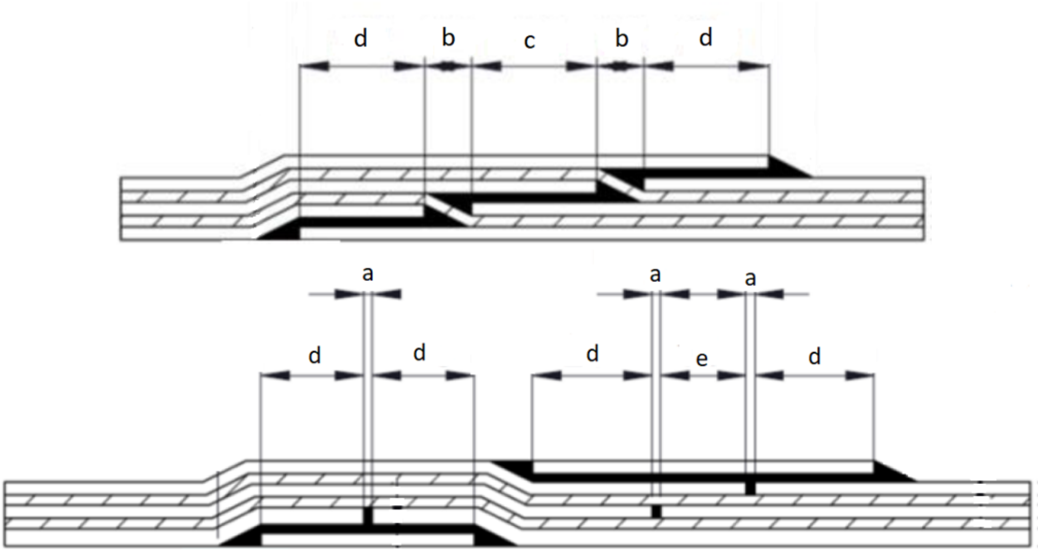

Figure 3.1: Broken down splice features.

Table 3.1: Description of the splice features under investigation.

Feature	Description	Splice
a	Butt joint	Butt splice
b	Overlap gap	Overlap splice
c	Internal overlap	Overlap splice
d	External overlap	Both
e	Distance between butt joints	Butt splice

Upon successful implementation of the FE analysis, outputs such as local stresses are extracted and used in quantitative engineering analysis of the particular joint in question. This is later combined with the methodology described in paper by Spronk et al. [12], giving insights into metal fatigue initiation within FMLs. Having the location of the damage onset from FEA and the damage onset lifetime from the numerical analysis, the answer to the first sub-question can be given. The complete framework to predict the cycles to metal fatigue initiation within the spliced FML in shown in Figure 3.8. The answers to the sub-questions 2 and 3 require a more general overview of the splice performance and can be provided after the experimental testing.

3.2 Finite element model

Following the framework outlined in Figure 3.8, a Finite Element model has been built to establish fatigue critical locations, stress concentration factors, internal stresses in aluminium, prepreg, and adhesive system. While the FE model is utilised in the prediction of metal fatigue initiation, it is also used to parametrically study the splices. Numerical samples are subjected to maximum and minimum loads of the Constant Amplitude (CA) fatigue loads, mimicking the real-life loading.

3.2.1 Set-up

Material model

Three materials are modeled, that is aluminium alloy 2024-T3, the GFRP with S2-glass fibers and FM94 resin system, and the FM94 epoxy on its own for the resin rich regions. 2024-T3 alloy and the GFRP are assumed to be linear elastic due to the relatively small loads present during fatigue loading. The FM94 resin is modeled to be elasto-plastic as the resin has shown to be ductile rather than brittle [10]. To accurately estimate the critical stress in Equation 2.4, plasticity has to be taken into account because of the ductile nature of this resin.

Table 3.2: Aluminium alloy 2024-T3 mechanical properties [14].

Property	Value	Unit
Young's modulus, E	72.4	GPa
Poisson's ratio, ν	0.33	-
CTE, α_t	$22 \cdot 10^{-6}$	degC^{-1}

Table 3.3: FM94 epoxy resin elastic mechanical properties [14].

Property	Value	Unit
Young's modulus, E	2.19	GPa
Poisson's ratio, ν	0.33	-
CTE longitudinal, $\alpha_{t,x}$	$6.1 \cdot 10^{-6}$	degC^{-1}
CTE transverse, $\alpha_{t,y}$	$26.2 \cdot 10^{-6}$	degC^{-1}

Table 3.4: FM94 epoxy resin linear Drucker-Prager plasticity model [10].

Property	Value	Unit
Angle of friction, β	24.51	deg
Flow stress ratio, K	1	-
Dilation angle, ψ	18.43	deg

Table 3.5: Hardening data for FM94 for linear Drucker-Prager model [10].

Stress [MPa]	Plastic strain [-]
30	0.000
35	0.001
40	0.003
45	0.006
50	0.017

Table 3.6: GFRP uni-directional prepreg, S2-glass fibres and FM94 matrix mechanical properties [14]. *out-of-plane properties are assumed equal to their transverse counterparts [15].

Property	**Value**	**Unit**
Young's modulus, fibre direction, E_1	50.0	GPa
Young's modulus, transverse direction, E_2	9.0	GPa
*Young's modulus, transverse direction, E_3	9.0	GPa
Poisson's ratio, ν_{12}	0.33	-
*Poisson's ratio, ν_{13}	0.33	-
Poisson's ratio, ν_{23}	0.06	-
Shear modulus, in-plane, G_{12}	3.5	GPa
*Shear modulus, out-of-plane, G_{13}	3.5	GPa
Shear modulus, transverse, G_{23}	3.0	GPa

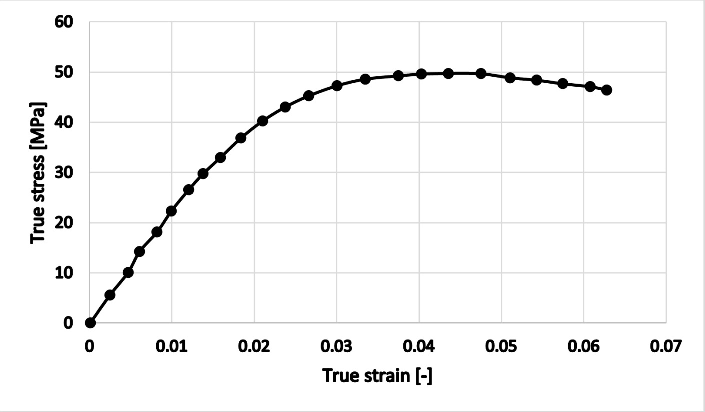

Figure 3.2: Tensile response of FM94, adapted from Quan and Alderliesten [10].

Elastic properties of aluminium are given in Table 3.2. For the FM94 resin system, the elastic properties are displayed in Table 3.3, the parameters for the linear Drucker-Prager plasticity model, proven to be accurate by Quan and Alderliesten [10], is given in Table 3.4, and hardening data is given in Table 3.5. The hardening data was extracted graphically from Figure 3.2. Uni-Directional (UD) prepreg properties are listed in Table 3.6. To ease the overall modelling and improve efficiency of the simulation, the prepreg layup is modeled as a single lamina. That means that representative equivalent properties for such lamina had to be determined. Taking the prepreg's GLARE4A layup, that is $[0/90/0]_{GFRP}$, it is possible to compute the equivalent engineering constants of the laminate with the help of Classical Laminate Theory (CLT), the methodology of which is described in detail in Appendix A. Moreover, since the model is a solid 3D model[1] and not a shell model, there is a need in the out-of-plane engineering constants which CLT does not offer since it employs a plain-stress assumption in its formulation.

The equations of Gibson [47] , Equation 3.1 - Equation 3.5, for cross-ply laminates are used to find the through-thickness laminate properties

---

[1] 3D solid model rather than 2D shell model was found to be more accurate for FML applications by Smolnicki and Stabla [36].

$$\nu_{13} = V_0 \frac{\nu_{13}^{ply}(1-\nu_{21}^{ply}\nu_{12}) + \nu_{23}^{ply}(\nu_{12}^{ply}-\nu_{12})}{1-\upsilon_{12}^{ply}\upsilon_{21}^{ply}} + V_{90} \frac{\nu_{13}^{ply}(\nu_{21}^{ply}-\nu_{12}) + \nu_{23}^{ply}(1-\nu_{12}^{ply}\nu_{12})}{1-\upsilon_{12}^{ply}\upsilon_{21}^{ply}} \tag{3.1}$$

$$\nu_{23} = V_0 \frac{\nu_{13}^{ply}(\nu_{21}^{ply}-\nu_{21}) + \nu_{23}^{ply}(1-\nu_{12}^{ply}\nu_{21})}{1-\upsilon_{12}^{ply}\upsilon_{21}^{ply}} + V_{90} \frac{\nu_{13}^{ply}(1-\nu_{21}^{ply}\nu_{21}) + \nu_{23}^{ply}(\nu_{12}^{ply}-\nu_{21})}{1-\upsilon_{12}^{ply}\upsilon_{21}^{ply}} \tag{3.2}$$

$$E_3 = \left[\frac{1}{E_3^{ply}} - \frac{(\nu_{13}^{ply})^2}{E_1^{ply}} - \frac{(\nu_{23}^{ply})^2}{E_2^{ply}} + V_0\left(\frac{\nu_{13}^{ply}\nu_{13}}{E_1} + \frac{\nu_{23}^{ply}\nu_{23}}{E_2}\right) + V_{90}\left(\frac{\nu_{13}^{ply}\nu_{23}}{E_2} + \frac{\nu_{23}^{ply}\nu_{13}}{E1}\right)\right]^{-1} \tag{3.3}$$

$$G_{13} = \left(\frac{V_0}{G_{13}^{ply}} + \frac{V_{90}}{G_{23}^{ply}}\right)^{-1} \tag{3.4}$$

$$G_{23} = \left(\frac{V_0}{G_{23}^{ply}} + \frac{V_{90}}{G_{13}^{ply}}\right)^{-1} \tag{3.5}$$

where the superscript *ply* indicates the engineering property of the UD ply, otherwise the laminate constant is used. V_0 and V_{90} refer to the volume fraction of the longitudinally vs. transversely oriented plies, respectively. Assuming that the UD plies are of equal volume makes $V_0 = 2/3$ and $V_{90} = 1/3$. With UD ply properties in Table 3.6, CLT, and the equations of Gibson mentioned above, it is possible to compute engineering constants of the prepreg laminate, given in Table 3.7.

Table 3.7: GFRP prepreg [0/90/0] laminate (S2-glass fibres and FM94 matrix) mechanical properties.

Property	Value	Unit
Young's modulus, fibre direction, E_x	36.7	GPa
Young's modulus, transverse direction, E_y	22.9	GPa
Young's modulus, transverse direction, E_3	9.0	GPa
Poisson's ratio, ν_{xy}	0.13	-
Poisson's ratio, ν_{xz}	0.24	-
Poisson's ratio, ν_{yz}	0.15	-
Shear modulus, in-plane, G_{xy}	3.5	GPa
Shear modulus, out-of-plane, G_{xz}	3.32	GPa
Shear modulus, transverse, G_{yz}	3.15	GPa

Element choice

The model is a solid 3D model, the choice made in order to facilitate accuracy of mechanical deformation and stress states under applied load. The exact elements chosen are C3D20R, that is a "20-node quadratic brick, reduced integration" type. Although more computationally costly, these elements generally lead to an improved accuracy in stress magnitudes and distributions, as was demonstrated by Smolnicki et al. [36]. Such second-order elements are also better suited in models with complex geometries and capture stress concentrations more accurately. They are beneficial when problems involve bending, even if the extent of bending is small, like in the case of this research where secondary bending is expected. Reduced integration is employs 8 integration points, down from 27, and is recommended for second-order elements due to more accurate results and prevention of shear and volumetric locking, provided that strains are not excessive, which is expected to be the case for fatigue stress levels [11].

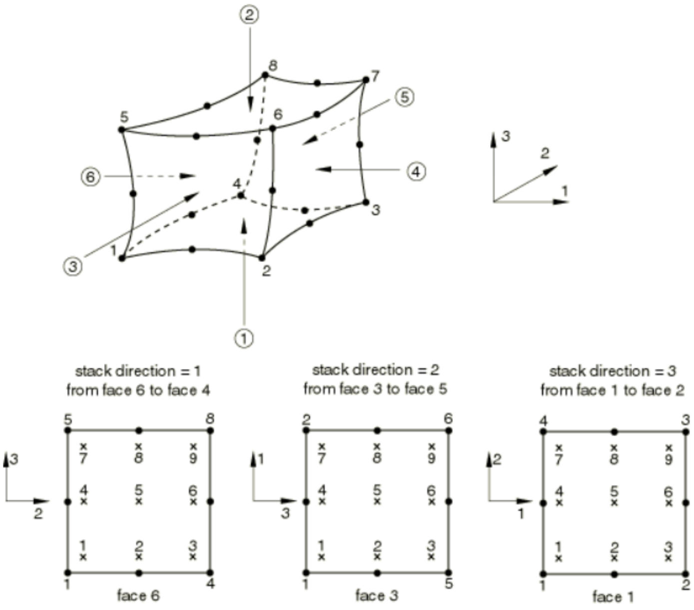

Figure 3.3: 20-node solid brick in ABAQUS [11].

Contact

To model a perfect contact between the laminae surfaces, that is no slip contact between the surfaces, a tie constraint is employed. This constraint type is not necessarily a contact interaction, yet it successfully models perfect adhesion by tying the nodes of the adjacent surfaces together. This constraint type, however, would not be suitable if failure is expected as it does not facilitate any type of separation of the surfaces from one another, i.e. delamination or disbonding. Since the load levels at which fatigue tests are performed are below the minimal expected loads to initiate significant damage, this method is deemed appropriate. To employ this constraint, ABAQUS offers a tool to automatically detect surface pairs that are within the tolerances specified. The tolerance of surface pairs detection was set to 0.001 mm.

Scenario

Even though the model is meant to predict the location of the first fatigue damage, the model is quasi-static. It is assumed that a region in the splice that is the most critical statically is also the most critical in fatigue loading due to structure being in the elastic regime during fatigue load levels. Each specimen is clamped on one side (U1 = U2 = U3 = UR1 = UR2 = UR3 = 0)[2] and is subjected to a uniform load on the opposing end. The loaded end is also

---

[2] In ABAQUS, X, Y, Z directions are referred to as 1, 2, 3, respectively. *U* is translational displacement, and *UR* is rotational displacement.

restricted by multiple roller boundaries to allow movement only in the axial direction (U2 = U3 = UR1 = UR2 = UR3 = 0). On both sides of the specimen a Z-symmetry boundary condition is applied (U2 = UR1 = UR3 = 0) to avoid effects of the free edges on the stress field, and thus simulate the middle of the specimen. For visual aid, refer to Figure 3.4. This allowed to model a specimen of 1 mm width instead of full specimen width, reducing the computational costs greatly without impacting accuracy through keeping analysis in the 3D domain as suggested by Smolnicki and Stabla [36].

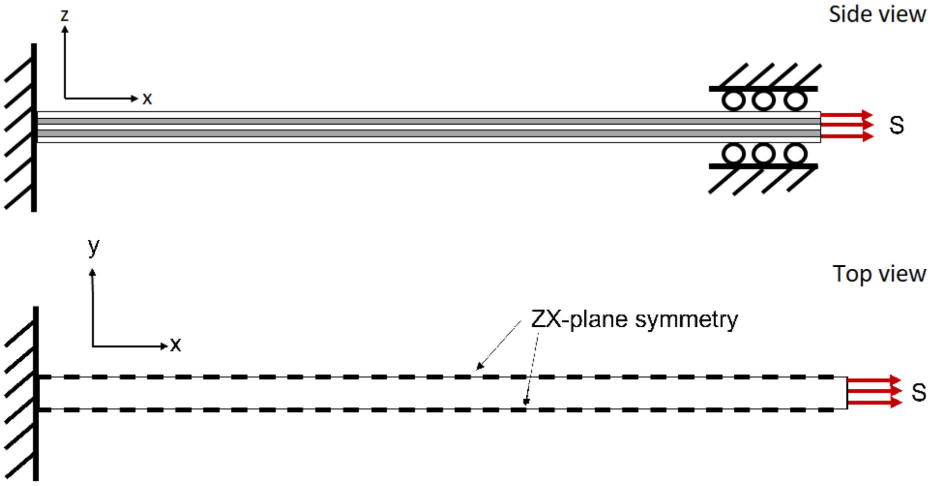

Figure 3.4: Loading scenario of an FML sample. Not to scale.

Due to the secondary bending effects in the asymmetric spliced specimens a non-linear analysis is employed to tackle this geometric non-linearity and improve solution convergence.

3.2.2 Verification & Validation

To ensure that the models and decision based on those models are representative of the real-life situation, the models must be verified and validated. These activities relate the finite element model built, since the model was built from scratch for this specific study and does appear anywhere else. The model of Spronk et al. [12] has been validated, although with a limited validity based on the reference data used. CLT is a widely used tool to analyse and design composite materials and therefore does not require any specific validation as only the standard methods have been used. Validity of CLT can be found in the literature, along with all of its underlying assumptions.

Verification

Verification is done via multiple ways, such as comparison against other verified models, in this case CLT and mesh convergence studies of the model.

A simple model of an unspliced GLARE4A-3/2-0.4 sample was built in order to compare the stresses and strains of the FE model and the CLT model. The results of the verification study

Table 3.8: Verification of the FEM model against CLT at $S = 100MPa$

	σ_{AL}[MPa]	σ_{GFRP} [MPa]	ε_{FML} [-]
FEM	127.36	58.08	0.00157
CLT v1	124.92	61.67	0.00170
CLT v2	124.92	-	0.00170
$\lvert Error_{MAX}\rvert$ [%]	2.0	5.8	7.6

Table 3.9: Verification of the FEM model against CLT at $S = 200MPa$

	σ_{AL}[MPa]	σ_{GFRP} [MPa]	ε_{FML} [-]
FEM	254.90	116.25	0.00314
CLT v1	249.84	123.33	0.00341
CLT v2	249.83	-	0.00341
$\lvert Error_{MAX}\rvert$ [%]	2.0	5.7	7.9

are summarised in Table 3.8 and Table 3.9. Two CLT models were built, 'CLTv1' contained prepreg layers with smeared properties, while 'CLTv2' modeled all individual UD prepreg layers. The results show that internal stresses and strains are very similar between CLT and Finite Element Method (FEM) models, with all errors being below 8%. Moreover, the internal stresses in aluminium deviate by only 2% between FEM and CLT, which is the most of-use result in this research as it is used in the initiation prediction model. When increasing the applied stress from 100 to 200 MPa, there is little-to-no difference in the errors. This way of verifying the FE model ensures that the boundary conditions, the material models, load application, and the constraints all yield an accurate result and thus can be deemed to be correctly implemented.

Mesh convergence was performed on a complete overlap splice. The results of the mesh study are displayed in Figure 3.5. It appears that at around 30,000 elements the model seems to converge to an appropriate degree. Regardless, between 2,000 and 64,0000 elements there is only a 4.3 % error in local stresses, which is not a large error considering the difference in mesh elements. It is therefore deemed appropriate to keep the number of mesh elements around 30,000 to 40,000 elements to yield accurate results without significantly increasing computational cost.

Validation

Validation was performed on the OS_2 sample. Validation data is taken from a fatigue experiment of the unnotched OS_2 sample loaded under $S_{max} = 120$, with $R = 0.1$. The comparison between in the strain fields obtained is visible in Figure 3.6. Averaged engineering strain data extracted from a virtual line along the sample under Digital Image Correlation (DIC), and the same data extracted from ABAQUS can be seen in Figure 3.7.

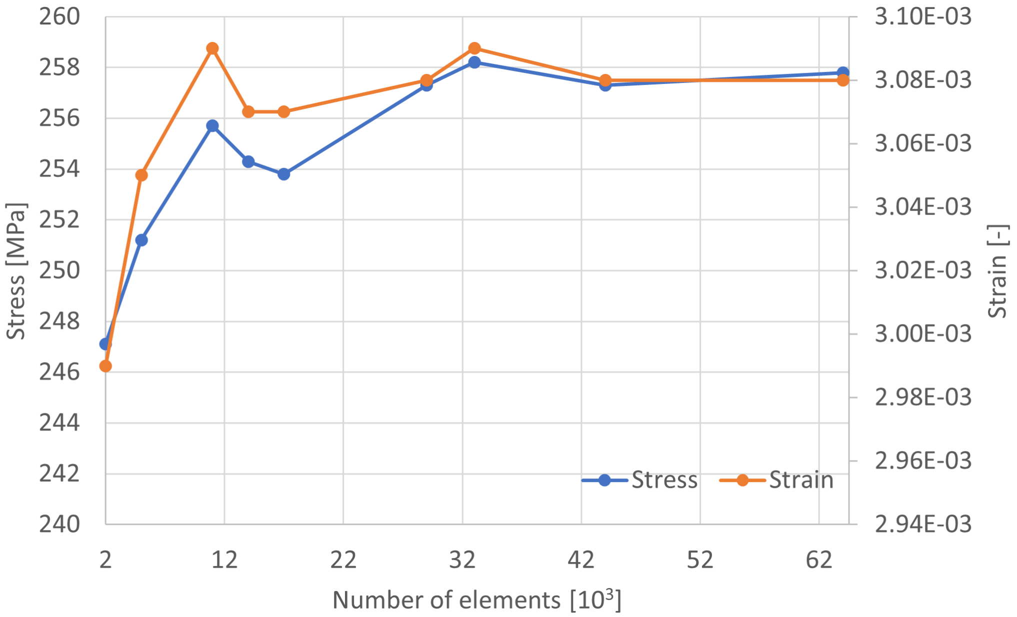

Figure 3.5: Mesh convergence of the overlap splice $S = 100MPa$

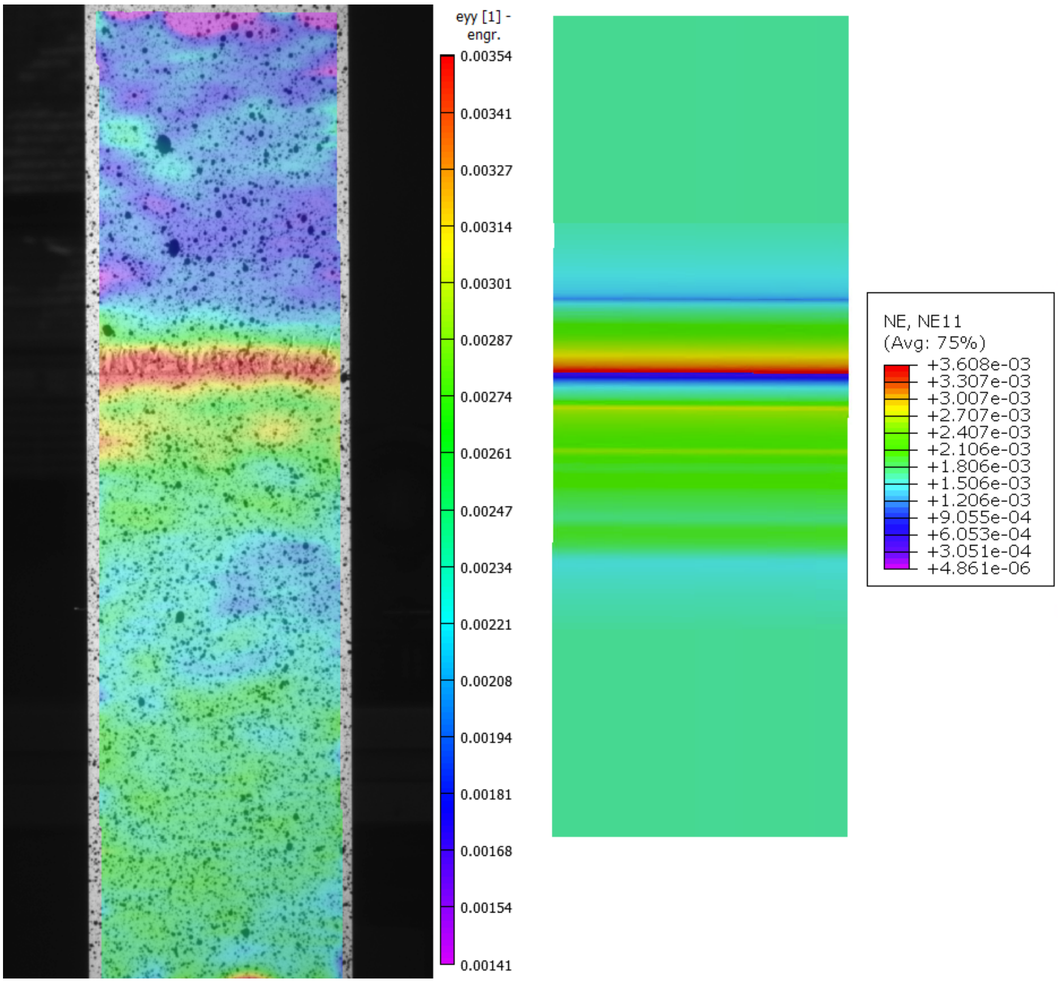

Figure 3.6: Validation of Longitudinal engineering strain profiles comparison between DIC and ABAQUS.

Looking at Figure 3.6, several differences and similarities can be obtained. The Finite Element (FE) model is able to accurately capture the stress concentration around the edge of the overlap, which can be also seen from the peaks in Figure 3.7. The difference in peak engineering strains is only 2.8%, which is considered to be a good correlation. Furthermore, the farfield strains seem to have an acceptable correlation both in downward and upward directions from the joint, although on average, the DIC is showing larger strains than FEM. This could be explained by the thermal residual stresses that would influence DIC images and FEA results, since curing is not part of the FE model. Curing of the samples would cause residual tension in the aluminium layers, and since only aluminium layers are visible to the DIC cameras, it makes sense that the strains on the DIC appear on average to be higher. In addition, it is common for FE models to act stiffer than their real-life counterparts due to a limited number of Degrees Of Freedom (DOF), which further adds to this difference in strains.

Finite Element Analysis (FEA) shows a drop in strain experienced by the overlapping aluminium layer that is not present in DIC. Since it is expected that the edge of the overlap carries little load due to the load transfer path, similar to lap shear joints, the discrepancy is likely caused by the resolution of the DIC images. It could be further explained by the filter that was used to post-process the DIC data, which was set to 21x21 pixels. Since it is the peaks in stresses that are of interest in this research, as well as the location of such peaks, it is deemed that the FEM model shows good correlation with real-life behaviour of the splice joint. It is thus assumed that the model would perform equally well in other splice configurations and in other loads, as long as mechanical response of the joint remains in the elastic regime and material models, boundary conditions, and loading conditions are consistent. The model can therefore be used for its intended purpose.

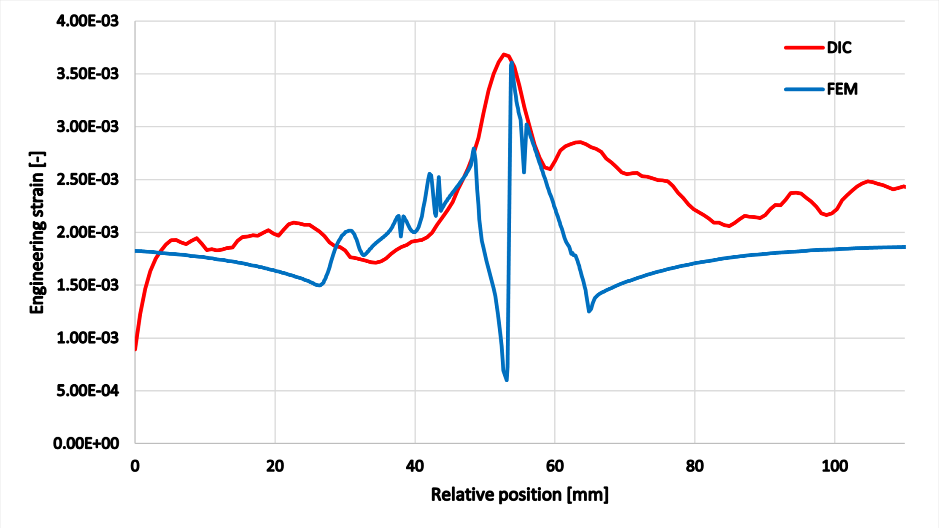

Figure 3.7: Validation of engineering strain vs. Relative position along the splice under 120 MPa loading.

3.3 Prediction of life to damage initiation

Prediction of fatigue life initiation concerns the initiation of crack propagation in the metal layers of the FML. The methodology is based on an assumption that the life to initiation in FMLs can be equated to life to failure in monolithic metal specimens [8]. The assumption is founded upon the observations on the metal fatigue life cycle, where cycles to initiation take up the majority of such life cycle. For a mathematical representation of such an assumption, see Equation 3.6.

$$S - N_{i,FML} \;=\; S - N_{f,Metal} \tag{3.6}$$

According to the literature review described in chapter 2, the model of Spronk et al. [12] is the most up-to-date approach to predict fatigue cycles to damage initiation in FMLs. Nevertheless, the validity of this approach is highly dependent on the experimental and the reference data used, specifically the similarity between the two. The reference data used for this approach is taken from a fatigue handbook [16].

For the detailed description of the model, the reader is encouraged to look at the source paper for this model [12]. Several adaptations to the said model are laid out further in this chapter.

The model uses the solution of Lekhnitskii [48] to calculate peak stresses around the notch, and consequently K_t of the subject. The solution does not work, however, if the laminate is asymmetric and / or unbalanced, which is the case in the spliced region of the structure. Therefore, to calculate stress concentration FEM is utilised. Since FEM outputs internal stresses instead of $K_{t,splice}$ directly, the need for Equation 3.8 and Equation 3.7 disappears and $\sigma_{k,peak}$, the peak internal stress in the k^{th} layer of laminate, and $S^{mech}_{k,nom}$, nominal mechanical stress in the k^{th} layer of laminate, are retrieved directly from the numerical simulations.

$$S^{mech}_{k,nom} = (S_{k,ff} - S^{th}_{k})\left(\frac{W}{W-d}\right) \tag{3.7}$$

$$\sigma_{k,peak} = K_{t,splice} \cdot S^{mech}_{k,nom} + S^{th}_{k} \tag{3.8}$$

where W is the width of the specimen, d is the diameter of the hole, S^{th}_{k} is residual thermal stress induced by curing and cooling of the sample, and $K_{t,splice}$ is the stress concentration caused by the splice geometry itself. Since the FE model does not involve the curing cycle of the laminate, this is later superimposed numerically, combining the outcomes of CLT and FEM, see Equation 3.9.

$$S_{k,nom} = S^{mech}_{k,nom} + S^{th}_{k} \tag{3.9}$$

where $S^{mech}_{k,nom}$ is an output of the FEA and S^{th}_{k} is the result of CLT.

In case a notched specimen is analysed, Equation 3.10, Equation 3.11, and Equation 3.12 are used to adapt the nominal and the peak stresses of the laminate.

$$K_{t,notch} = 2 + 0.284\left(1 - \frac{d}{W}\right) - 0.6\left(1 - \frac{d}{W}\right)^2 + 1.32\left(1 - \frac{d}{W}\right)^3 \tag{3.10}$$

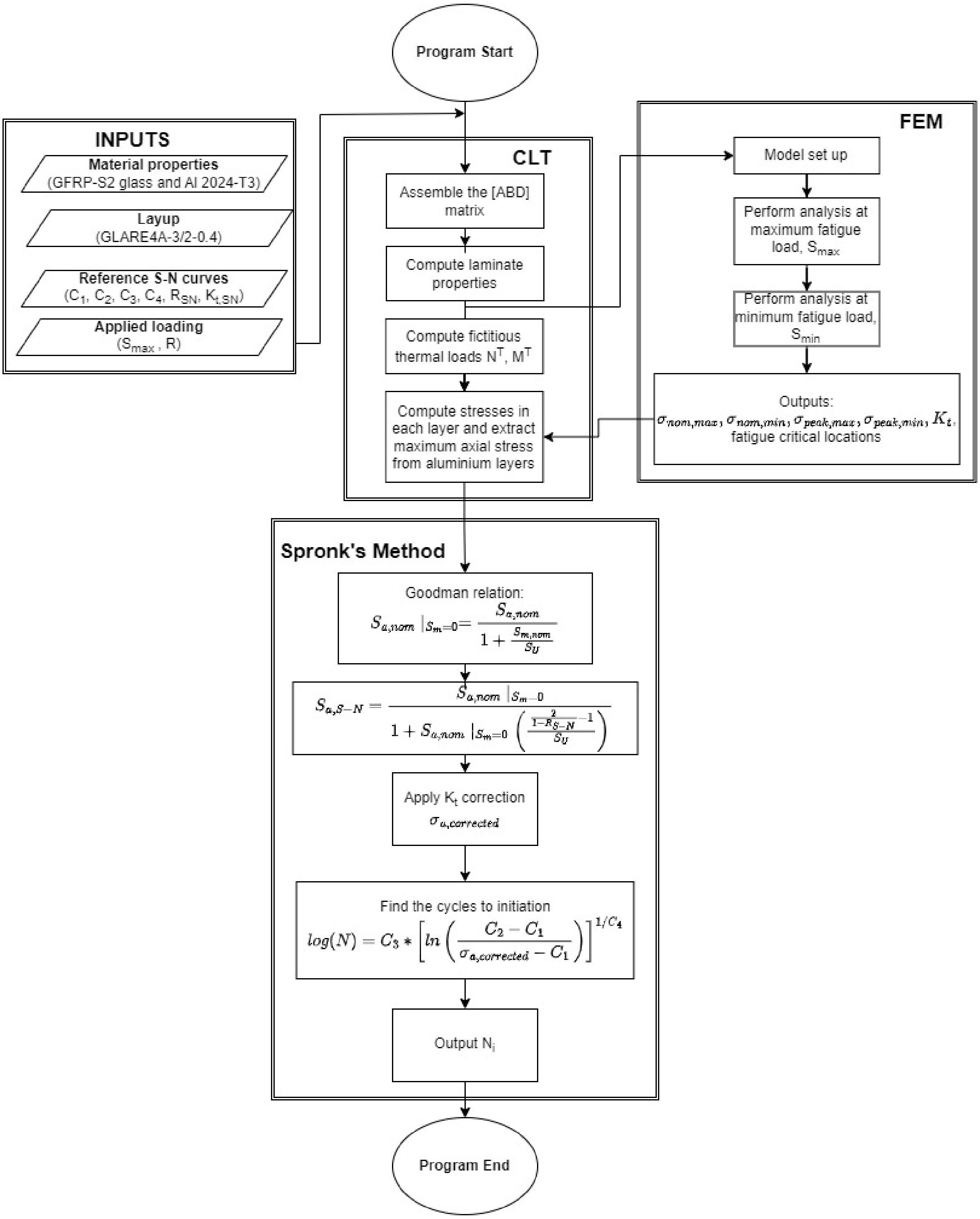

Figure 3.8: Framework to predict cycles to metal fatigue initiation utilising FEM and method developed by Spronk et al. [12], referred to as "Spronk's Method".

$$S^{mech}_{k,nom,notched} = S^{mech}_{k,nom,unnotched}\left(\frac{W}{W-d}\right) \tag{3.11}$$

$$\sigma_{k,peak,notched} = K_{t,notch} \cdot \sigma_{k,peak,unnotched} + S^{th}_{k} \tag{3.12}$$

where $K_{t,notch}$ is the stress concentration factor caused by the notch. Consequently, it is possible to compute the total stress concentration factor of the splice specimen by simply taking the ratio of the peak stress and the nominal stress, see Equation 3.13.

$$K_{t,total} = \frac{\sigma_{k,peak}}{S_{k,nom}} \tag{3.13}$$

This way $K_{t,total}$, or simply K_t, includes $K_{t,notch}$ and $K_{t,splice}$, even though the two haven't been explicitly superposed. If an unnotched specimen is used, the diameter d can be set to 0 and $K_{t,notch}$ can be set to 1.

The nominal stress amplitude and nominal mean stress are then calculated using the following relations described in Equation 3.14 and Equation 3.15.

$$S_{m,nom} = \left(\frac{1+R_{nom}}{2}\right) S^{max}_{k,nom} \tag{3.14}$$

$$S_{a,nom} = \left(\frac{1-R_{nom}}{2}\right) S^{max}_{k,nom} \tag{3.15}$$

whereR_{nom} is not to be confused with the R, the former one being the stress ratio of nominal stresses occurring in the metal layer of interest, and R being the applied stress ratio. To be able to relate the applied stress levels to the reference S-N curves, the respective stress amplitude of the S-N reference curve is computed using Equation 3.16. The derivation for it can be found in the paper proposing this model [12].

$$S_{a,S-N} = \frac{S_{a,nom}\ |_{S_m=0}}{1 + S_{a,nom}\ |_{S_m=0}\left(\frac{\frac{2}{1-R_{S-N}}-1}{S_U}\right)} \tag{3.16}$$

To take into account different stress concentration factors of the data to be compared, the reference stress amplitude is corrected via a correction factor, f_{corr}. It is suggested that reference data with $K_{t,S-N}$ lower than the K_t occurring in the laminate is used. This way, a correction factor f_{corr}, given by Equation 3.17, can be applied to $S_{a,S-N}$, the result of which, $S_{a,corr}$, can then be used to graphically obtain the cycles to initiation.

$$f_{corr} = \frac{K_{t,total}}{K_{t,S-N}} \tag{3.17}$$

The reference data comes in a form of a best-fit curve, represented by Equation 3.18 [16].

$$log(N) = C_3 * \left[ln\left(\frac{C_2 - C_1}{\sigma_{a,corrected} - C_1}\right)\right]^{1/C_4} \tag{3.18}$$

where C_1, C_2, C_3, C_4 are fitting constants for each dataset. How these are determined can be found in the fatigue handbook [16]. As mentioned earlier, to obtain the most accurate results it is best that the reference and experimental settings match closely. Reference data with R_{S-N} closest to R_{nom}, and $K_{t,S-N}$ closest but smaller to $K_{t,peak}$.

3.4 Limitations

It is important to acknowledge the limitations of the presented methodology for a better understanding of the results and conclusions drawn in the end of this thesis research.

1. The finite element model is a quasi-static model with no damage modelling. This means that it is not possible to predict the damage progression that is caused by accumulation of damage during loading purely from the simulation. The damage can, however, be added manually by altering the simulation model in further iterations if necessary.

2. For the same reason as above, it is not possible to model static or dynamic ultimate failures of the splices.

3. Further, the FE model is mostly an elastic model, with the exception of the adhesive. This means that the methodology used is assuming that the loading is such that the perfectly elastic regime within the composite and metal constituents is retained and would not be valid if the specimen would enter elasto-plastic regime.

4. The model smears the properties of individual laminae within the composite layers, which are then modeled as a solid layer. This means that the internal stress within the individual plies cannot be obtained.

5. The initiation prediction model assumes that initiation begins in the metal layers of the laminate. This means that in case delamination is dominant damage mode in the splice, the model would not be able to predict it.

6. The accuracy of the model is largely dependent on the reference data chosen for the prediction of the initiation life. Therefore the accuracy of the results would reduce significantly if loading used in the experimental program was to deviate significantly from the the reference data, specifically in K_t and R used [12].

7. Lastly, although not directly related to the methodology, but the parametric study was only restrained to the parameters labeled in Figure 3.1 because of the material availability. For instance it was not possible to use sheet metal other than that of 0.4mm thickness, as although it was in stock, it was not pre-treated, which would add a significant amount of time to the production process and the overall lapse time of this research thesis.

Since the prediction of the initiation of fatigue damage in FMLs method have been adapted from Spronk et al. [12], an additional list of assumptions and limitations, including analytical, numerical, and practical assumptions, are outlined in both the above cited paper, as well as the master's thesis of Spronk [21].

Chapter 4

Splice design

In this chapter the systematic approach to splice design is applied, with final splice geometries showcased in the end of the chapter. Numerical experiments conducted in ABAQUS are described in section 4.1, general design considerations that lie outside of the quantitative analysis are described in section 4.2 and final designs are showcased in section 4.3.

4.1 Finite element investigations

The FE investigations that are showcased in this section are aimed to better understand the stress state within the splice geometry. With this knowledge, it is hypothesized that it would be possible to predict damage modes during fatigue loading, fatigue critical locations, and of course extract the stresses such that they can then be used to predict fatigue life to initiation in the metal layers. Each element of the splice is analysed separately. This way it is possible to identify stress field changes in the joint as a result of alterations of only one feature.

Internal butt splice

The internal butt-splice contains an interruption in the internal metal layer, in this case it is the middle layer. It is therefore expected that no secondary bending and peeling is going to take place due to symmetry.

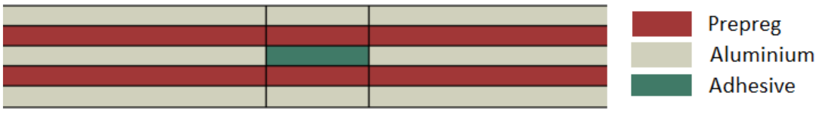

Figure 4.1: Internal butt splice model in material sections.

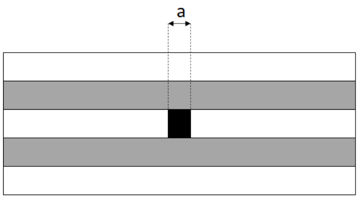

Figure 4.2: Internal butt splice sketch.

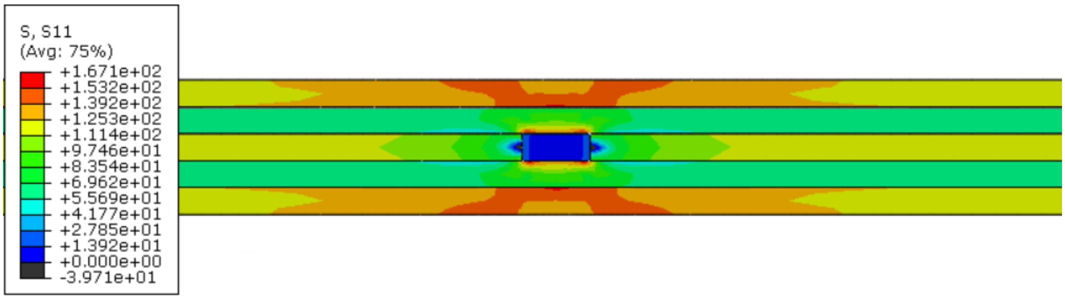

Figure 4.3: Axial stress distribution in an internal butt splice subjected to $S_{max} = 100$ MPa.

Table 4.1: Critical axial stresses of the internal butt-splice sample subjected to $S_{max} = 100$ MPa.

a [mm]	σ_x [MPa]	σ_x/σ_{base} [-]
1	163.9	1.31
2	164.4	1.32
3	164.2	1.31
4	166.2	1.33

σ_{base} is the internal axial stress in the metal layer of the base laminate, that is an unspliced laminate, equal to 125 MPa in the case where $S = 100$ MPa. σ_x is simply the axial stress. Evidently, changes in the butt splice width **a** do not result in in large changes in axial stress. Looking at the axial stress field shown in Figure 4.3, redistribution of stresses spans about 10 mm in total. The resin filler carries little-to-no load, as expected, and therefore could be excluded from future simulations for computational purposes. There is a slight trend of decreasing peak stress magnitudes and width **a**, see Table 4.1, however that can be considered insignificant since the change in stress is small when compared to reference stress. In real-life, imperfections within the specimen itself would likely result in larger stress changes than the ones found by FEM. Ideally, the shorter the butt width the better, however, it is important that there is a enough space in the butt joint for the abundant prepreg resin to flow into, and therefore $a = 2$ mm is suggested for manufacturing purposes.

External butt splice with a reinforcement doubler

External butt splice with an overlaping reinforcement doubler is located on the inner skin, non-flush side of the splice, and features a butt joint reinforced with an external aluminium sheet. Due to asymmetrical geometry, a certain degree of secondary bending is expected.

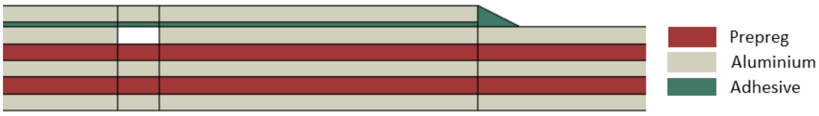

Figure 4.4: Internal butt splice model in material sections.

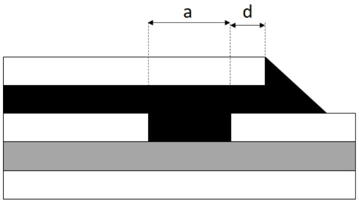

Figure 4.5: Internal butt splice sketch.

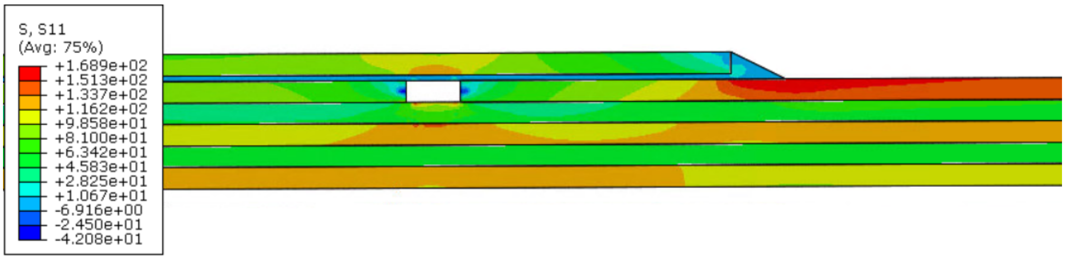

Figure 4.6: Axial stress distribution in the reinforced non-flush butt splice under $S_{max} = 100$ MPa.

Table 4.2: Displacement and critical stresses of of the sample with an external reinforcement doubler subjected to $S_{max} = 100$ MPa. $a = 2$ mm

b [mm]	σ_x [MPa]	σ_z [MPa]	τ [MPa]	σ_x/σ_{base} [-]
5	168.9	10.8	17.8	1.35
10	169.0	11.2	16.5	1.35
15	169.3	10.6	17.4	1.35
20	169.5	10.6	17.5	1.36

σ_z is the peel stress experienced by the adhesive, and τ is the shear stress also experienced by the adhesive. Once again, the difference in the stresses with variable reinforcement overlap lengths is negligible, as evident from Table 4.2. Most critical location is the reinforcement drop-off, with regards to peel, shear, and axial stress. The load transfer from the reinforcement sheet to the base laminate and the secondary bending causing tension in top layers of the structure are superposed to create a stress concentration in the red area seen in Figure 4.6.

External butt-splice with a flush reinforcement doubler

External butt-splice with a flush reinforcement doubler is similar to the feature, since it is also a butt joint reinforced by an additional aluminium sheet. In this case, however, the reinforcement sheet is flush with the surface of the laminate, aimed for the outer skin side of the aircraft.

Figure 4.7: Internal butt splice model in material sections.

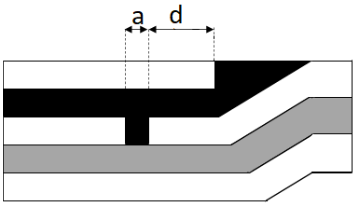

Figure 4.8: Internal butt splice sketch.

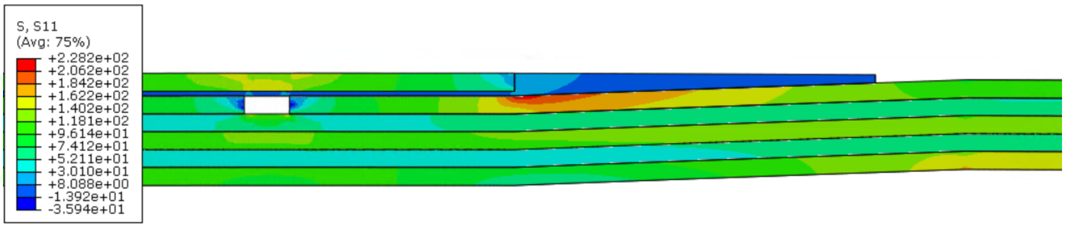

Figure 4.9: Axial stress distribution in the reinforced flush butt splice under $S_{max} = 100$ MPa.

Table 4.3: Displacement and critical stresses of of the sample with an external reinforcement doubler subjected to $S_{max} = 100$ MPa. $a = 1$ mm

d [mm]	σ_x [MPa]	σ_z [MPa]	τ [MPa]	σ_x/σ_{base} [-]
5	228.2	13.8	23.0	1.83
10	228.6	13.5	22.6	1.83
15	229.0	13.5	22.7	1.83
20	229.2	13.5	22.7	1.83

Judging from Table 4.3, stresses did not change significantly with variation of the reinforcement overlap length, but the stresses in the most critical location of flush reinforcement increased substantially ($\approx 35\%$) when compared to the non-flush critical axial stresses, seen in Table 4.2. This could be explained by an additional stress concentration caused by the slight curvature of the base laminate around the reinforcement sheet, seen in red in Figure 4.9.

Complete overlap splice

In order to analyse the features of the overlap splice in a 3/2 laminate, a complete overlap splice has been built. As seen from the Figure 4.10, there are 3 parameters analysed, **d**, **b**, and **c**. This was done by keeping two out of the three parameters constant while the other parameter varied in dimensions. In addition, the entire length of the splice sample is kept constant too, to ensure that secondary bending effects are not caused by the length of the joint but by the changes in the respective parameter. The adhesive within the interruption was not taken into account and therefore was not modeled, see Figure 4.11.

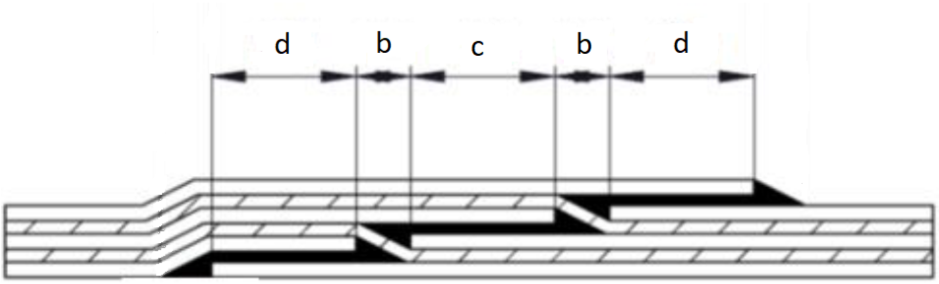

Figure 4.10: Overlap splice drawing. Not to scale.

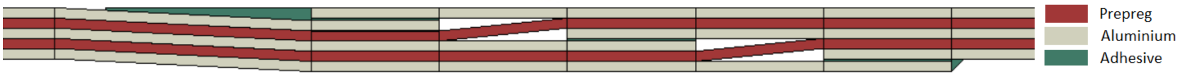

Figure 4.11: Overlap splice model.

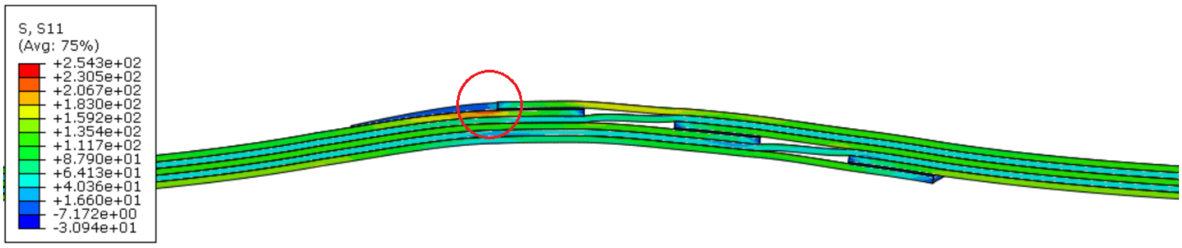

Figure 4.12: Overlap splice axial stress distribution under $S_{max} = 100$ MPa. Deformation scaled up 30 times. Critical location circled in red.

Table 4.4: Displacement and critical stresses of of the sample with an external reinforcement doubler subjected to $S_{max} = 100$ MPa. $b = 10$ mm, $c = 10$ mm.

d [mm]	σ_x [MPa]	σ_z [MPa]	τ [MPa]	σ_x/σ_{base} [-]
5	247.2	19.7	25.3	1.98
10	245.6	19.2	24.6	1.96
20	245.5	19.1	24.5	1.96

Table 4.5: Displacement and critical stresses of of the sample with an external reinforcement doubler subjected to $S_{max} = 100$ MPa. $d = 20$ mm, $c = 10$ mm.

b [mm]	σ_x [MPa]	σ_z [MPa]	τ [MPa]	σ_x/σ_{base} [-]
5	247.5	19.3	25.2	1.98
10	245.6	19.2	24.6	1.96
15	243.4	18.9	24.3	1.96

The analysis revealed that in the overlap splice the most critical stress location is at the drop-off of the flush reinforcement, see Figure 4.12. This is similar to the stress state of the flush reinforcement butt splice seen in Figure 4.9. Variations in **b**, **c**, and **d** do not cause significant

Table 4.6: Displacement and critical stresses of of the sample with an external reinforcement doubler subjected to $S_{max} = 100$ MPa. $d = 20$ mm, $b = 10$ mm.

c [mm]	σ_x [MPa]	σ_z [MPa]	τ [MPa]	σ_x/σ_{base} [-]
5	246.7	19.1	25.1	1.98
10	245.5	19.2	24.6	1.96
15	244.8	19.0	24.2	1.96

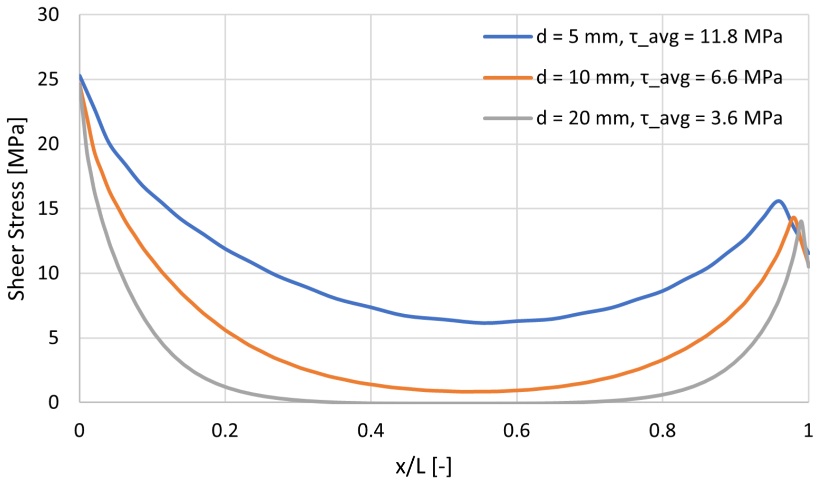

Figure 4.13: The effect of the overlap length on the shear stress profile within the overlap.

changes in the peak stresses of the joint. This is documented in Table 4.5, Table 4.6, and Table 4.4. The shortening in **d**, however, causes the average shear stress in the adhesive within the overlap to increase, depicted in Figure 4.13. While the different between $d = 20$ mm and $d = 10$ mm is only 3 MPa, the difference between $d = 20$ mm and $d = 5$ mm is 8.2 MPa. This may drive premature failure in form of a delamination of the outer-most overlap.

Complete butt splice

A complete butt splice has been modeled to analyse the stress behaviour of the complete joint, and to investigate features where a complete joint is beneficial, such as dimension **e**, see Figure 4.14. In this case, the resin filler in the butt joints has not been modeled as it provides no additional strength to the butt splice joint, see Figure 4.15. Geometries **a** and **d** have already been investigated in previous sections.

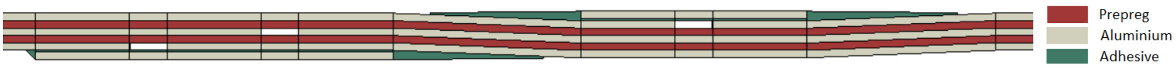

Figure 4.15: Complete butt splice model.

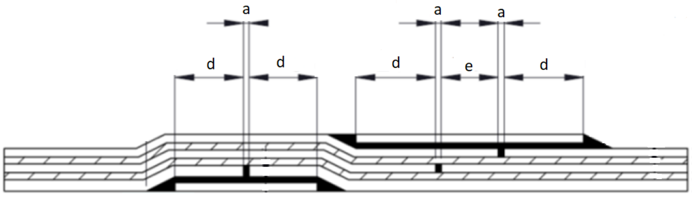

Figure 4.14: Complete butt splice drawing.

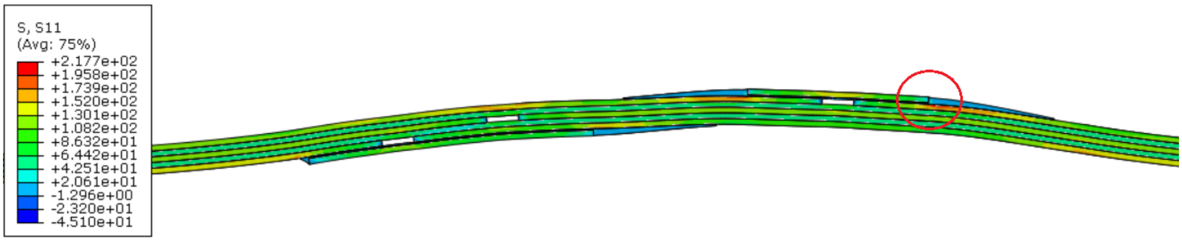

Figure 4.16: Butt splice axial stress distribution under $S_{max} = 100$ MPa. Deformation scaled up 30 times. Critical location circled in red. Not to scale.

Table 4.7: Displacement and critical stresses of of the sample with an external reinforcement doubler subjected to $S_{max} = 100$ MPa. $d = 20$ mm, $a = 2$ mm.

e [mm]	σ_x [MPa]	σ_z [MPa]	τ [MPa]	$\sigma_x/\sigma_{x,base}$ [-]
5	222.5	16.7	19.5	1.78
10	222.4	16.6	19.4	1.78
15	224.5	16.3	19.3	1.80

Axial stress distribution of the butt-splice is shown in Figure 4.16, and it reveals that the critical fatigue area is the same as the predicted by the investigation of the unique splice details. The flush reinforcement drop-off is the critical location in both cases, and as evident from Table 4.7, the peak stresses do not change significantly based on the geometrical changes within the splice. The average sheer stress in the overlap adhesive has also increased like in Figure 4.13.

4.2 General considerations

Several conclusions could be drawn based on the observations in the numerical experiments.

Firstly, it is clear that when it comes to internal stresses, any dimension investigated results in little changes to the stress field in either of the splices, considering that he dimensions of the parameters studied varied from 5 to 20 mm. Shorter overlaps do cause an increase in the average sheer stress within the adhesive, with peak stresses remaining relatively unchanged. This means that if the design was to be made based purely on these observations, features as small as 5 mm could be employed in the design as to reduce the size, and similar damage initiation lifetimes are expected as those are dependent on peak stresses. This way the weight of the joint is reduced without sacrificing strength and durability of the joint. The same cannot be said for the damage progression however, as in the smallest joints the average stress in the adhesive is predicted to increase, which might results in an alternative damage path.

Secondly, independent numerical experiments have revealed that it is the flush reinforcement overlap that is the most critical feature of the splice. This phenomenon appears both in the butt splice and the overlap splice, and has been previously foretold by the simulations on the isolated flush reinforcement. Although this feature provides a smooth facing on the skin side of the joint, it results in location that is most critical when it comes to fatigue. It is believed that the additional curvature of the subsurface layer present in this flush reinforcement is what causes most severe stress concentrations in the splice. In fact, it adversely affects the overlap splice more so than the butt splice. The butt splice showcased peak axial stress levels of $\approx$ 223 MPa, and the overlap $\approx$ 245 MPa. For reference, the flush reinforcement overlap tested independently, see Figure 4.9, showcases peak axial stress levels of $\approx$ 229 MPa, meaning that the butt splice design managed to reduce peak stresses, where the overlap splice increased them. This is attributed to the degree of secondary bending of the overall joint geometry. Ideally, one would want to increase the radius of the bend curvature that the flush reinforcement doubler creates by making a longer adhesive fillet for instance, and thus decrease the stress concentration around it. In reality, this curvature is defined by the pressure of the autoclave and is difficult to control. Consequently, no changes to the fillet radius are going to be made in this research as it is not the manufacturing of the splice that is of interest here. It remains difficult to predict whether fatigue damage in this location would take form of delamination or metal cracking, although it is certain that a release of the adhesive fillet would be seen, and that it is in that particular location where damage is predicted to commence. It is also possible that a combination of the two damage modes takes place.

With these considerations in mind, it is possible to come up with experimental designs that may lead to concrete design guidelines for such joint types. Nevertheless, it is important to keep in mind that overlaps in the joint must not be too short. This is because it might negatively impact the static strength of the joint and time between damage initiation and full delamination of the overlap could be too short to discover it so that a repair could be performed. While static strength is not evaluated in this research, the consideration of it remains crucial.

4.3 Final designs

To study the geometrical feasibility of the splice design and to validate the observations made with Finite Element Analysis (FEA), gradual reductions of the joint size are made. Since none of the dimensions are found to impact the peak stresses in the joint severely, they are all reduced simultaneously, with the smallest overlap dimensions being 5 mm in order to avoid large increases in peak and average stresses within the adhesive.

4.3.1 Overlap splice

The final designs for the overlap splice configurations are as follows:

1. **OS_0**: Reference overlap splice, with design recommendations taken from an internal GTM report [49]. This configuration acts as a baseline for comparison for alternative overlap splice geometries.

2. **OS_1**: An alternative overlap splice geometry that is hypothesized to perform as well as the reference one, **OS_0**.

3. **OS_2**: A critical configuration that is expected to cause smaller fatigue life due to the change in damage mechanisms, namely premature disbond of the outer overlaps due to the increase in average shear stress as depicted in Figure 4.13.

For visual representation of the configurations, see Figure 4.17

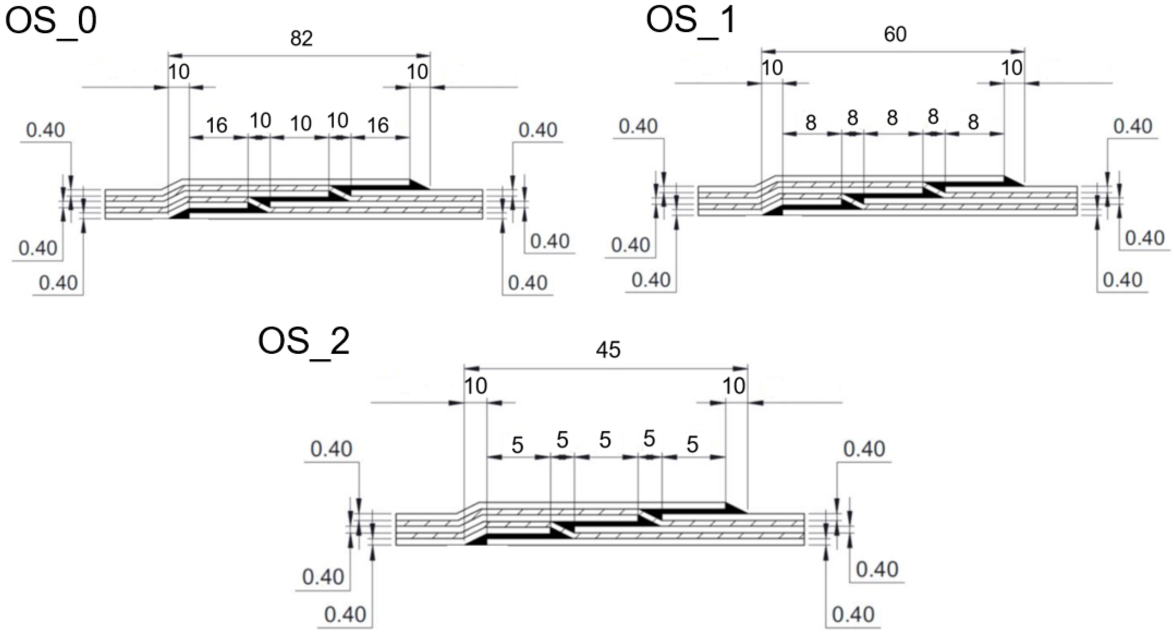

Figure 4.17: Designs of the overlap splice configurations to be subjected to experimental testing. Dimensions in [mm].

4.3.2 Butt splice

The final designs for the butt splice configurations follow a very similar logic than that of the overlap splice configurations, where the joint geometries were systematically made smaller and come as follows:

1. **BS_0**: Reference butt splice, with design recommendations taken from an internal GTM report [49]. This configuration acts as a baseline for comparison for alternative butt splice geometries.

2. **BS_1**: An alternative butt splice geometry that is hypothesized to perform as well as the reference one, **BS_0**.

3. **BS_2**: A critical configuration that is expected to cause smaller fatigue life due to the change in damage mechanisms, namely premature disbond of the outer reinforcements as depicted in Figure 4.13.

For visual representation of the configurations, see Figure 4.18.

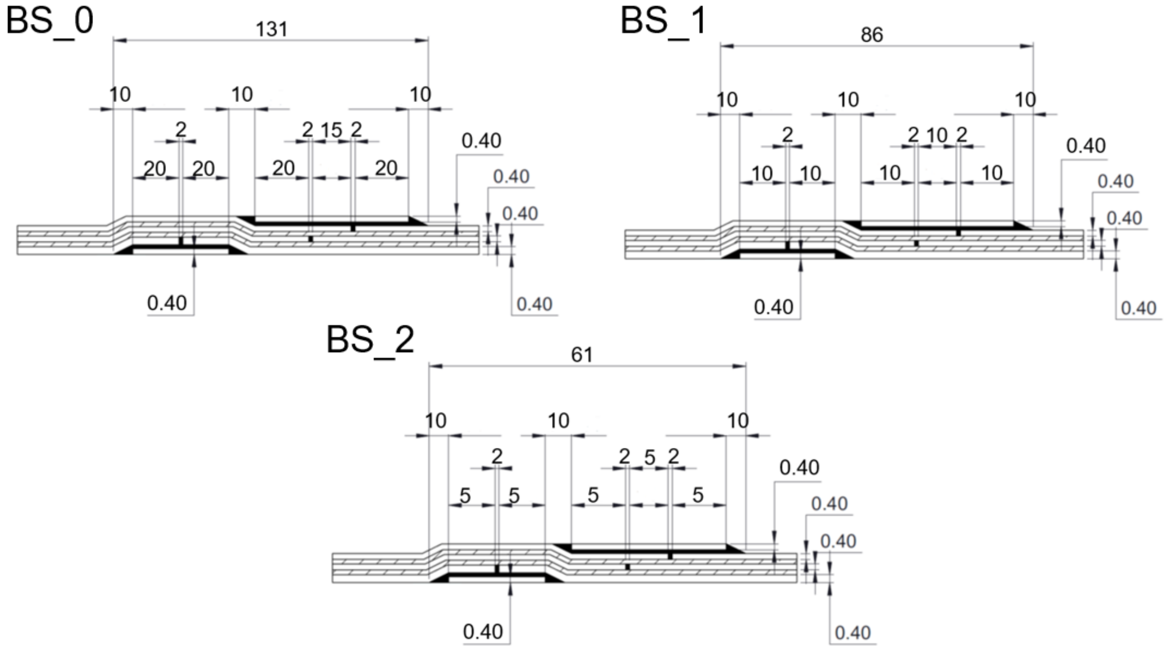

Figure 4.18: Designs of the butt splice configurations to be subjected to experimental testing. Dimensions in [mm].

4.3.3 Mass comparison

To provide an insight into the structural weight of the splice joint and how it compares from configuration to configuration, the unit weights have been calculated in Table 4.8. For comparison, the lightest configuration, OS_2, is taken as reference.

Table 4.8: Comparison of calculated mass between splice configurations.

Configuration	Length [mm]	Mass [gr/m]	Difference [%]
OS_0	82	0.448	+91
OS_1	60	0.320	+35
OS_2	45	0.237	0
BS_0	131	0.747	+215
BS_1	86	0.477	+101
BS_2	61	0.326	+38

It appears that the overlap splice is on average lighter than the butt splice, with the lightest configuration being OS_2, and the heaviest BS_0, with BS_0 being more than two times heavier than OS_2. This is expected as the butt splice configurations require additional reinforcement doublers, and the overlap splice utilises only the base laminate layers. Further, the total length of the overlap splice is on average shorter which lowers the unit mass of the joint.

Chapter 5

Production and Test Set-Up

This chapter talks about the testing of the coupons, as well as their manufacturing and design. Section 5.1 briefly talks about the motivation for the test program. Section 5.2 describes the coupons and their design, as well as the manufacturing path to obtaining the coupons. Finally, section 5.3 reports on the test setup.

5.1 Motivation

Experimental testing of spliced FML samples serves multiple purposes. Firstly, the results are used as validation data for the models and predictions made. That includes both numerical prediction models and FE models. Since it is difficult to predict exact damage progression during fatigue loading when complex geometries and several constituents are present, specially damage initiation within the FM94 epoxy, information from the experiments can provide insight into exact sequence of damage progression during fatigue loading of splices.

And secondly, they provide means to compare the fatigue performance of the two splices types in question without reliance on the validity of the models made. This comparative study does not only concern the two types of splices, but also different configurations of one splice.

5.2 Coupons

5.2.1 Design

Each coupon was designed such that is it of the same length as the rest, regardless of the length of the joint[1]. To eliminate the effects of the clamping on the secondary bending of the

---

[1] The lengths of the splice in each of the configurations are different, taking up different portions of the coupon, see Figure 4.17 and Figure 4.18.

coupons, it was ensured that the joint is at least 50t mm away from the clamp area[2], where t is the thickness of the base laminate, which is in the range of 1.85 - 2 mm. See Figure 5.2 for visual representation.

When it comes to notch location, this is derived from FEA, specifically it is the location with highest axial internal stresses in the metal layers, see Figure 5.1. Consequently, it is the location where fatigue damage is predicted to initiate. This is done to both validate the stress concentration displayed by FE simulations and also to evaluate the performance of the splice with the most critical notch location. The notch locations in the overlap splice and the butt splice are at the overlap drop-off on the flush side of the splice, caused by the secondary bending induced tension and the additional local curvature introduced by this feature.

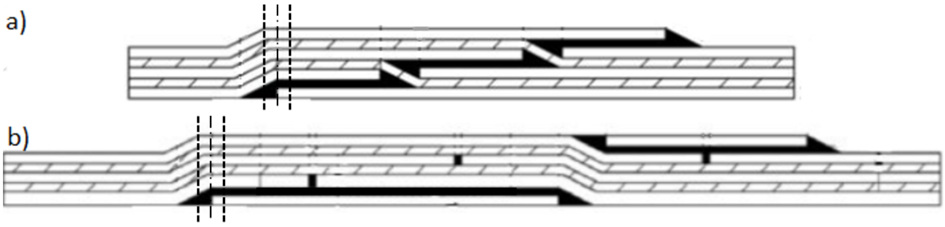

Figure 5.1: Notch location in **(a)** the overlap splice, **(b)** butt splice.

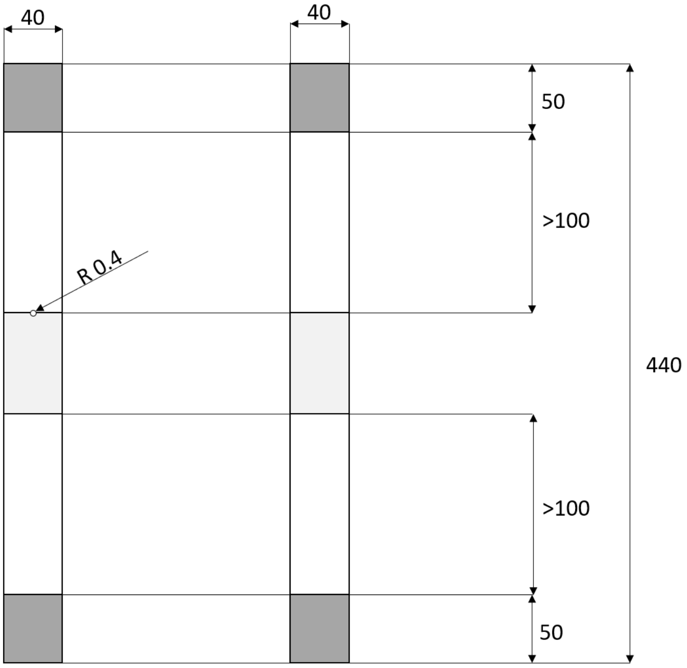

Figure 5.2: Notched and unnotched coupon geometry. Approximate location of the splice joint in light grey, clamping areas in dark grey.

---

[2] Advice of J. J. Homan, thesis co-supervisor from GTM Advanced Structures, based on his work on fatigue of Lap Shear Joints at Fokker company.

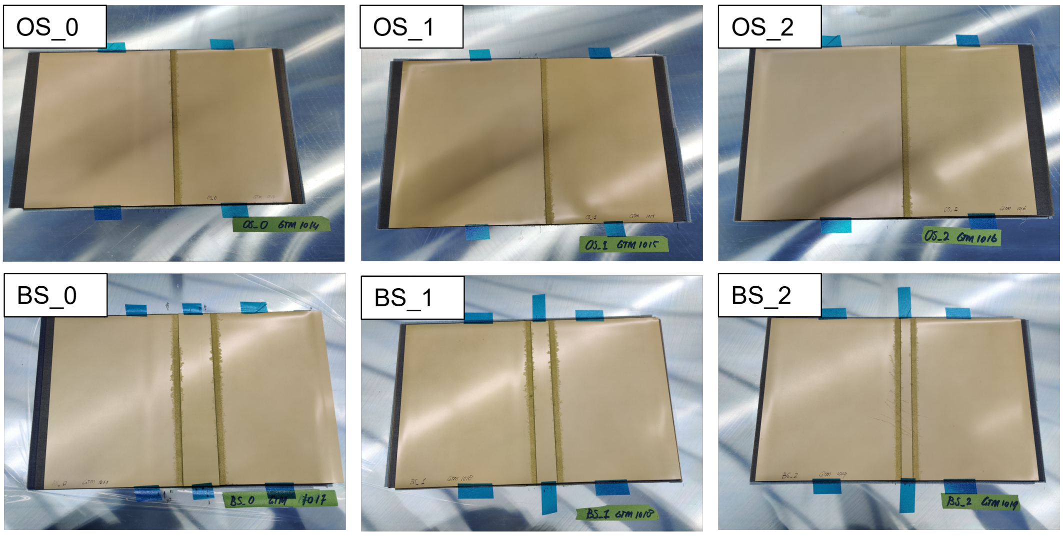

Figure 5.3: Post-autoclave panels ready for cutting into individual specimens.

5.2.2 Manufacturing

The coupons consist of 6 different types, presented in chapter 4. Due to the difficulties during manufacturing, specifically the differences in length of aluminium sheets for every layup, it was decided to cut the sheets into two dimensions, 220x300 mm and 260x300 mm, and trim the panel edges by sawing and milling the panels into coupon dimensions. The untrimmed edges are photographed in Figure 5.3. That means that although each coupon is of the same dimension, that is 40x440 mm, the joint is not centered in the coupon. This, however, should not have an influence on the results because of the sufficient distance from the joint end to clamping area.

All coupons are made of the same materials, that is Al 2024-T3 unclad alloy sheets of 0.4 mm thickness, GFRP with S2-glass and FM94 epoxy, and additional FM94 epoxy for the fillers and fillets. The laminates are GLARE4A-3/2-0.4, meaning that the prepreg layup is [0/90/0], with the total layup consisting of 3 aluminium and 2 prepreg alternating layers.

To manufacture the samples, SFT was used, which essentially means that the spliced GLARE samples have been let to self-form under the pressure of the autoclave. The curing cycle is documented in Figure 5.4. To ensure a flush surface on one side of the sample, aimed to imitate the outside of the aircraft skin, the laminate was built top-to-bottom, with the top being the flush side that touches the smooth aluminium mould plate. The cured panels can be seen in Figure 5.3, still attached to the mould table.

Dimensions of each splice configuration were measured post-production. An overview is presented in Table 5.1. It is important to keep these dimensions in mind, as the tolerances of the splices get more critical with the updated designs, like BS_2 and OS_2, due to the features within the splice getting smaller. This might cause a more severe local stress state within the splice, creating less room for tolerances, consequently making them more critical. This also provides an insight into manufacturing of such splices. Naturally, during the curing of the plates in the autoclave some sliding of the aluminium sheets and the fibers has happened. Since the tolerances are more critical in the butt splice rather than the overlap splice, namely

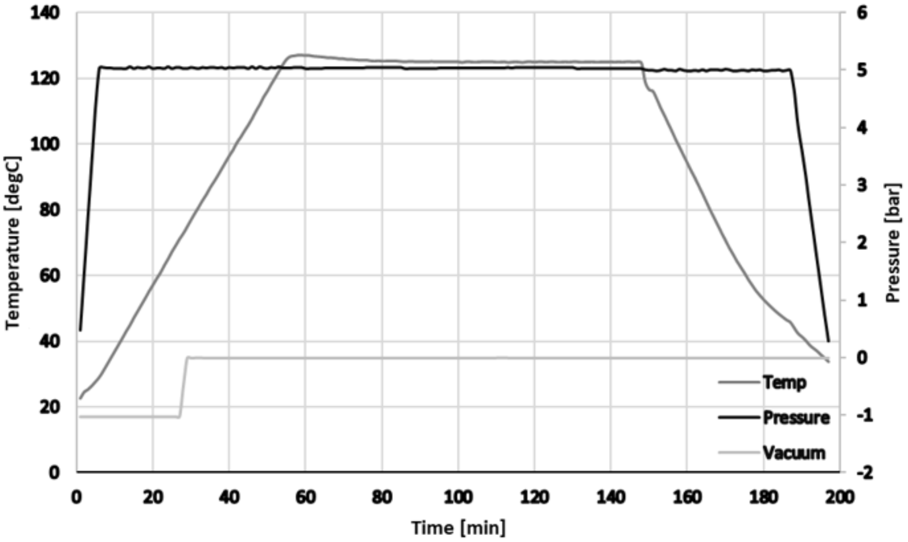

Figure 5.4: Curing cycle inside the autoclave for GLARE samples.

due to the butt widths that were set to 2 mm, it is safe to say that manufacturing of the butt splice panels took more effort than its counterpart. Manufacturing of the butt splice also proved to be more laborious due to an overall more complex layup than that of the overlap splice. While on a large-scale production the layup could be done in an automated fashion, it would still take longer to complete the layup of the butt splice than the overlap splice.

Each GLARE plate was approximately 500x300 mm, which led to 5 coupons of 40x440 mm being produced from each plate, except for BS_0, which yielded only 2 coupons. This was due to a manufacturing defect that took place during curing, resulting in warped panel where only 2 specimens could be salvaged. It is unclear why this specific panel was warped, however it is speculated that it was caused by the large protrusion of the outermost aluminium layer beyond the boundaries of the plate, which can be seen in bottom left image of Figure 5.3, causing it to bend the rest of the plate under the autocalve pressure to restore its internal force equilibrium. The overview of the total number of coupons in presented in Table 5.2.

Table 5.2: Production matrix

Splice	To test	Spare	Total
OS_0	2	3	5
OS_1	2	3	5
OS_2	3	2	5
BS_0	2	0	2
BS_1	2	3	5
BS_2	3	2	5
			27

Table 5.1: Comparison between the designed splice dimensions and the actual dimensions post-production.

Dimension	Ideal [mm]	Actual (avg.) [mm]	Outlier [mm]
OS_0			
External overlap, **d**	16	15.9	15.8
Internal overlap, **c**	10	10.2	-
Gaps, **b**	10	10.1	10.2
OS_1			
External overlap, **d**	8	7.9	7.6
Internal overlap, **c**	8	8.9	-
Gaps, **b**	8	8.0	7.0
OS_2			
External overlap, **d**	5	5.2	5.3
Internal overlap, **c**	5	5.5	-
Gaps, **b**	5	4.5	4.3
BS_0			
Width between butts, **e**,	15	15.5	-
External overlap, **d**	20	19.9	18.7
Butt width, **a**,	2	1.6	1.2
BS_1			
Width between butts, **e**,	10	10.7	-
External overlap, **d**	10	9.9	9.4
Butt width, **a**,	2	1.8	1.4
BS_2			
Width between butts, **e**,	5	5.7	-
External overlap, **d**	5	5.1	4.8
Butt width, **a**,	2	1.9	1.7

5.3 Experimental testing

The tests conducted involve tension-tension fatigue tests at R = 0.1, and frequency of 5 Hz. To capture the strain field, delaminations, crack initiation, and crack propagation, a two-camera set-up was used, one on each side of the specimen, the images of which were analysed using 2D DIC software. The set-up is visible in Figure 4.7, which shows 2 cameras pointing at the test specimen. Camera 1 is capturing the flush side of the specimen, also reffered to as the front of the specimen, from which damage is predicted to initiate, and Camera 2 is capturing the non-flush side, also known as the back of the specimen, where damage was expected to initiate later due to that side being under compression during secondary bending.

The test matrix is presented in Table 5.3. Unnotched specimens were tested at S_{max} = 250 MPa, and notched specimens were tested at S_{max} = 120 MPa. The reasons for choosing these specific stress levels are derived from literature. $S_{max} = 120MPa$ is comparable with aircraft loads during the ground-air-ground cycle[3], however, it has been documented that splices

---

[3] Although these loads are still slightly exaggerated by a factor of 1.2 - 1.5, with fuselage more typically experiencing 80-100 MPa hoop stresses under the pressurised cabin [27].

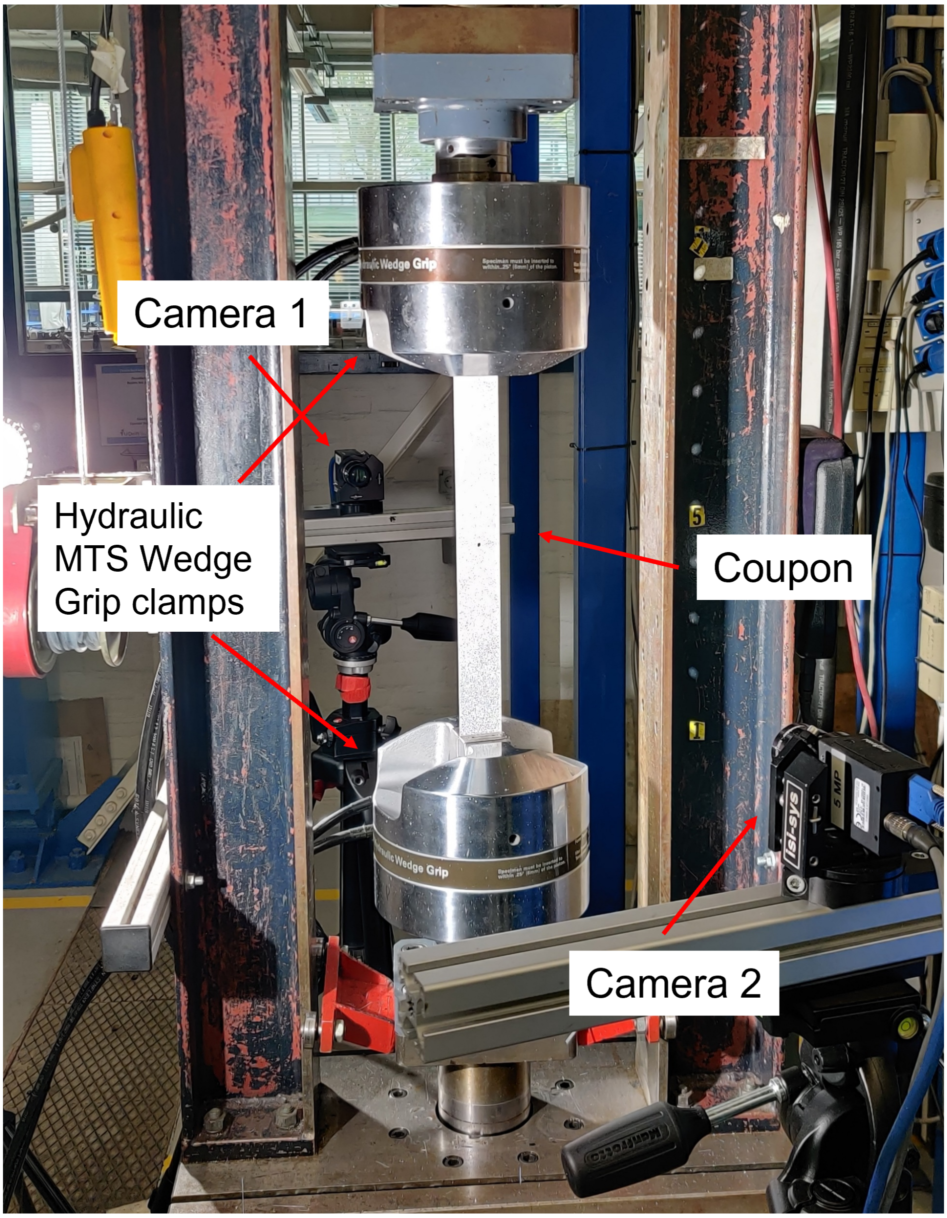

Figure 5.5: Physical experimental set-up.

Table 5.3: Test matrix

Splice	Notched?	S_{max} [MPa]	#
OS_0		250	1
OS_0	✓	120	1
OS_1		250	1
OS_1	✓	120	1
OS_2		250	1
OS_2	✓	120	1
OS_2		120	1
BS_0		250	1
BS_0	✓	120	1
BS_1		250	1
BS_1	✓	120	1
BS_2		250	1
BS_2	✓	120	1
BS_2		120	1
Total			14

perform well against such load levels, with specimens withstanding more than 1,000,000 cycles, which is way above the aircraft lifetime. Since there was little research on the notched spliced samples, this load level is chosen for specimens with a notch in critical location of the splice found during FEM analysis. Presence of a circular notch can simulate damage in the splice region and reduce the number of cycles to partial failure, making the test program feasible within the scope and time frame of this thesis research [6]. The satisfactory performance of the unnotched splices under realistic loads led to a choice of $S_{max} = 250$ MPa loading, exaggerating the loads by a factor of 2.5-3.1, when compared to typical hoop stress levels of 80-100 MPa [27]. This way damage can be seen quickly and the performance from specimen to specimen can be compared within an acceptable time frame. It is hypothesised that as long as the splice stays within the elastic regime, the damage propagation should remain the same. Finally, two additional tests were planned to confirm that the potentially weakest splice configurations, BS_2 and OS_2, are able to withstand aircraft loads for a satisfactory number of cycles. These samples therefore were unnotched and were tested at $S_{max} = 120 MPa$, at $R = 0.1$.

Chapter 6

Results

In this chapter the results of the experimental program are showcased, as well as the agreement between the experiments and the predictions made via an numerical approach. Section 6.1 describes the damage progression observed during the experiments. Section 6.3 outlines the experimental results of each splice configuration, and consequently provides a comparison between the predicted and the observed damage initiation cycles. A more detailed discussion of the results is provided in section 6.4. Finally, splice design guidelines derived from the observed results are proposed in section 6.5.

6.1 Damage propagation

6.1.1 Unnotched specimens

During the course of the experimental phase, it was found that the failure mode and damage progression was consistent throughout 4 out of 6 specimens. In majority of the specimens, the damage observed was the release of the adhesive fillet, followed by a shear cracking of the adhesive or a short disbond under 1mm of the outer aluminium, further transitioning into a metal fatigue crack of the adjacent underlying metal layer, see Figure 6.1 and Figure 6.2. An identical damage progression was observed by De Ruyter [7] and Hooijmeijer [5], see Figure 2.6 and Figure 2.7. All damage was initiated at the flush side of the specimen, attributed to secondary bending that causes additional tension on flush side of the splice. For a photo of the actual damage refer to Figure 6.3. Furthermore, it is important to note the difference in load levels applied during the experiments on the unnotched specimens and the experiments done by De Ruyter [7], with damage observations again underlined in Figure 2.7. Although De Ruyter [7] utilised $S_{max} = 150$ MPa, which is 100 MPa less than the applied load on the unnotched specimens in this thesis research, $S_{max} = 250$ MPa, the damage progression follows a similar pattern. This suggests that at any load given load level between $S_{max} = 150$ and $S_{max} = 250$ MPa, the damage progression would remain identical. This further supports the hypothesis that a high applied load used in the experiments described does not cause an alternative damage path and thus can be used confidently to compare fatigue performance of the splice joints described here.

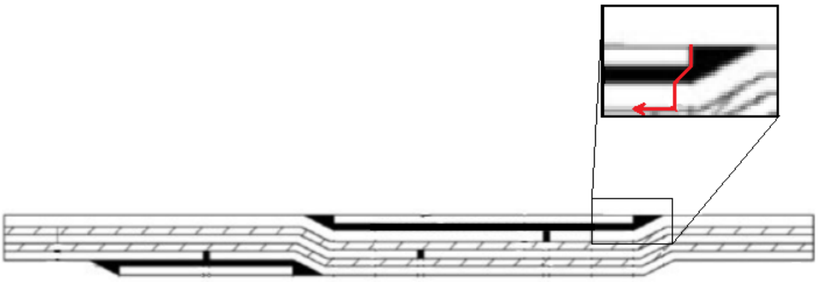

Figure 6.1: Initial damage progression in butt splices BS_0 and BS_1 under $S_{max} = 250$ MPa.

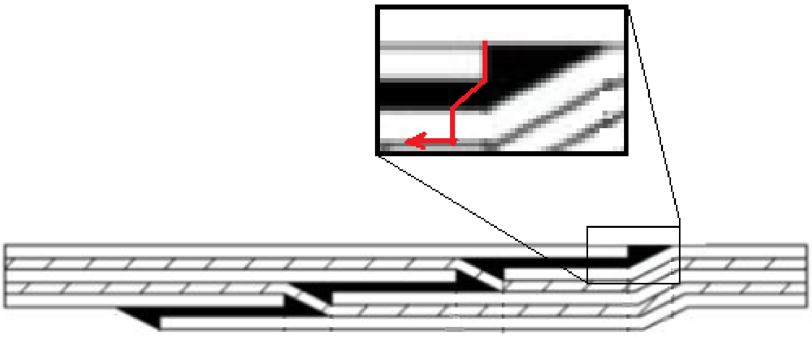

Figure 6.2: Initial damage progression in butt splices OS_0 and OS_1 under $S_{max} = 250$ MPa.

Figure 6.3: Typical fracture of the BS_0, BS_1, OS_0, OS_1. Adhesive fillet release followed by metal fatigue of bottom layer in the overlap, followed by interlaminar delamination.

Figure 6.4: Fracture of BS_2. Adhesive fillet release, followed by full delamination of the overlap, followed into delamination in within the butt joint and interlaminar delamination.

The 2 out of 6 specimens, specifically BS_2 and OS_2, stood out in the damage sequence in splice configurations, see Figure 6.5 and Figure 6.6. These configurations showed a full delamination of the overlap and did not show an early transition into metal cracking. This could be explained by a combination of factors. The shortest overlaps cause a slight increase in peak shear stresses of the adhesive, and the overall average stress of adhesive in the overlap, see Figure 6.8. While the peak shear stresses changes are insignificant, the shear stress in the middle of the of adhesive film is increased substantially, thus raising the average shear stress in the adhesive. Further, less load is carried by the metal layer when approaching the edge of the overlap, making it less likely to develop a crack. Such a stress field results in delamination rather than metal fatigue crack. A photo of BS_2 fracture is displayed in Figure 6.4. There is no image of OS_2, as unfortunately, that sample failed completely due to excessive cycles that occurred overnight. Nevertheless, the case of OS_2 shown in Figure 6.6. It is difficult to say what exactly occurred after the full disbond of the overlap. It is possible that the disbond caused the prepreg layer to fail due to overstress, or that the disbond caused cracking of the metal layer below, consequently diverting more load from the cracked metal to the prepreg layer, causing it to eventually fail due to overstress.

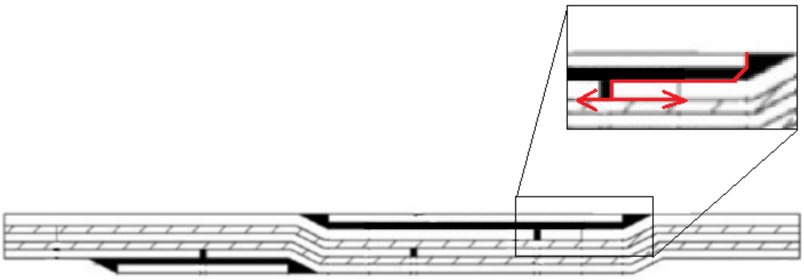

Figure 6.5: Initial damage progression in butt splices BS_2 under $S_{max} = 250$ MPa.

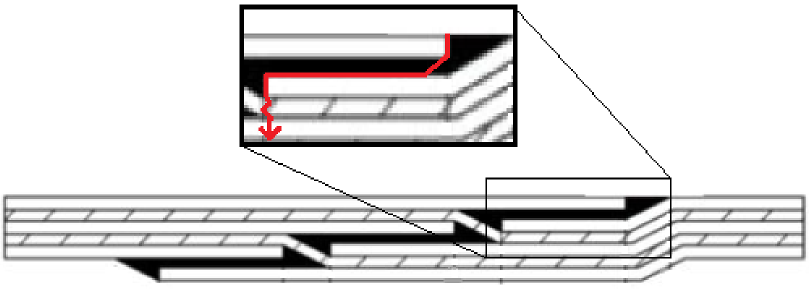

Figure 6.6: Initial damage progression in butt splices OS_2 under $S_{max} = 250$ MPa.

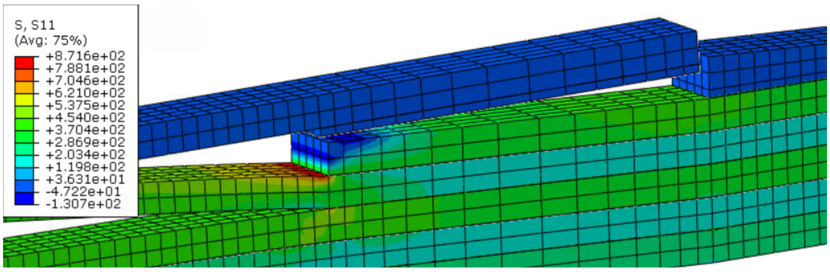

Figure 6.7: Stress field of the OS_2 with delaminated overlap under $S_{max} = 250$ MPa. Peak stress concentration in the prepreg layer at the interruption of the aluminium layer.

To understand what has occurred after the disbond of the overlap, a case was simulated with the overlap disbonded, which resulted in a concentration of stresses in the prepreg right next to the overlap end, see Figure 6.7. FEM simulation results in a peak axial stress of

872 MPa in the composite layer. Since the composite is modeled as a solid material with smeared laminate properties, this stress value does not represent the local stress within the outermost lamina of the respective prepreg layer. Thus it is not possible to exactly evaluate whether a composite failure criteria is satisfied in the most affected lamina as for that stresses within individual laminae are necessary. However, deducing from the experiment and the FEA findings depicted in Figure 6.7, it is likely that the 0^o glass fiber layer failed shortly after the overlap disbond due to a consequent overstress.

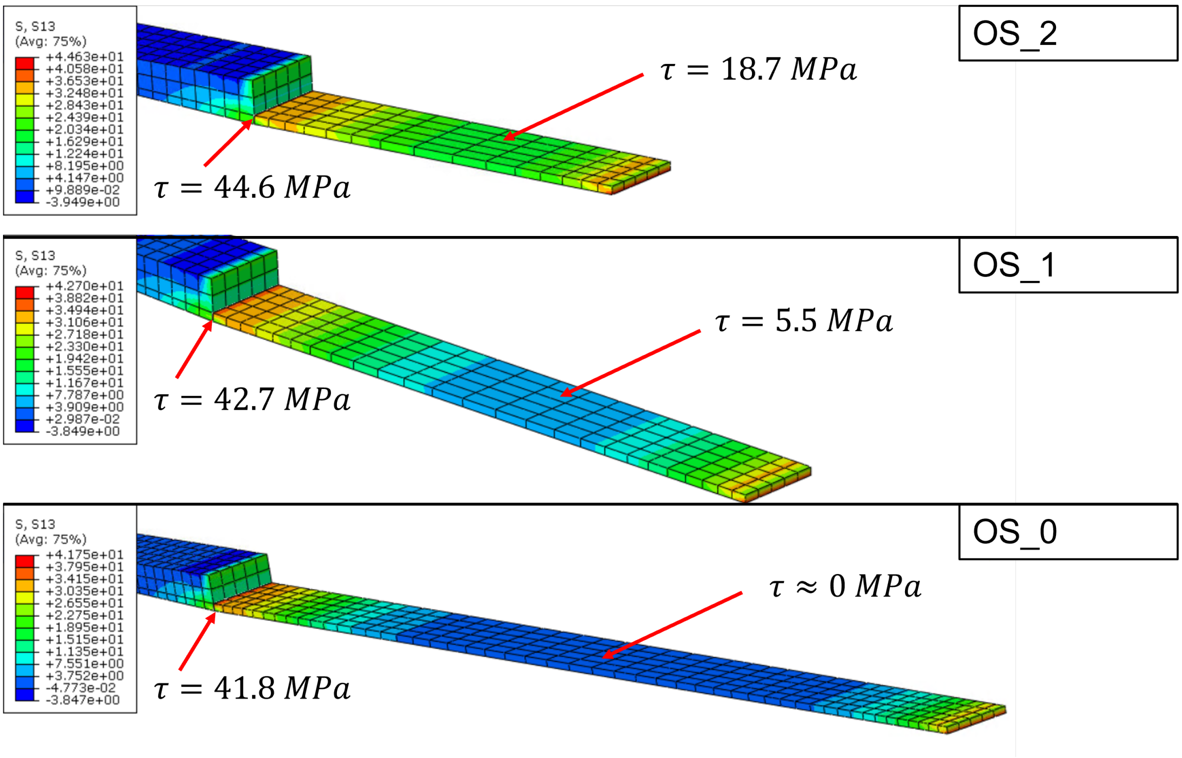

Figure 6.8: Comparison of shear stresses in the adhesive between overlap configurations under $S = 250$ MPa. The peak shear does not increase significantly, while the average shear increases substantially due to the shorter overlap.

The FE models were able to correctly point to the the location of initial damage, in both overlap and butt splices. When manually causing disbonds or delaminations in the model by turning off the tie constraint between the lamina and the adhesive, the model correctly points to locations of consequent damage.

As said earlier in section 5.3, two additional experiments have been conducted with BS_2 and OS_2 splice configurations without a notch under $S_{max} = 120$ MPa, $R = 0.1$[1]. The purpose of these tests was to confirm that no damage occurs within these splices under fatigue loads similar to those experienced by the structure during the ground-air-ground cycle, and therefore confirming that the newest designs are structurally feasible. Both samples withstood 600,000 cycles without any damage, after which the tests were stopped. The 600,000 cycles target

---

[1] Remember that this is different to the other unnotched samples, which were loaded at $S_{max} = 250$ MPa, $R = 0.1$.

was chosen arbitrarily. Since this number of cycles exceeds the reference number of cycles of 48,000 set by European Aviation Safety Agency (EASA) [50] more than 12 times, it is safe to assume that the proposed splice configurations are able to withstand ground-air-ground cycle loads for a sufficient lifetime.

6.1.2 Notched specimens

Specimens with a blunt notch followed a similar damage pattern shown in Figure 6.1 and Figure 6.2. Similarly, all damage initiated at the flush side of the specimen because of secondary bending present. Since the hole was drilled in the most critical location, see Figure 5.1, which is the same location as the initial damage location in the unnotched samples, the notch only accelerated the damage progression of the unnotched specimens in case of BS_0, BS_1, OS_0, and OS_1. In cases of BS_2 and OS_2, there was no disbond of the overlap as was observed with the unnotched samples, and the damage initiated around the notch as an adhesive fillet separation a metal fatigue crack. Therefore it can be concluded that in the case of a notch under high cycle fatigue loading, metal fatigue cracking is the predominant damage mechanism.

6.2 Predictions of metal fatigue initiation

The results of the methodology described in Figure 3.8 are summarised in Tables 6.1, 6.2, and 6.3. The reference data was chosen based on the K_t and the R_{peak} of each test case, leading to $S_{a,corr}$, which is then compared to the reference curves chosen, with the final outcome being the initiation life N_i. All parameters displayed in the below tables are for the metal layers in the FML.

Table 6.1: Calculation results for the unnotched samples. $K_{t,S-N} = 1$, $R = 0.25$ reference data used [16]. $S_{max} = 250$ MPa, $R = 0.1$ applied loading. Peak stress includes thermal and mechanical stress.

Splice	$\sigma_{peak,max}$[MPa]	R_{peak}[-]	K_t[-]	$S_{a,corr}$[MPa]	N_i[cycles]
OS_0	500.1	0.23	1.47	101.3	738,516
OS_1	500.3	0.24	1.47	101.3	738,516
OS_2	521.4	0.26	1.53	105.6	545,285
BS_0	494.2	0.21	1.45	100.1	816,377
BS_1	492.3	0.21	1.44	99.7	845,062
BS_2	488.8	0.22	1.43	99.0	903,740

For the notched case, two tables are displayed with different reference data, Table 6.2 and Table 6.3, and the reason for it follows. Since K_t of the overlap splice ranged between 5.25 and 5.45, and the butt splice between 4.69 and 4.81, it was decided to choose a different reference datasets to better match the splices to the reference tests. Thus the $K_{t,S-N} = 5.2$, $R = 0.25$ dataset was chosen for the overlap splice, and $K_{t,S-N} = 3.6$, $R = 0.25$ dataset fro the butt splice, which lead to minimal K_t corrections [16]. However, this resulted in longer initiation lives for the overlap splices than the butt splices, even though the stress concentration in the overlap splices is higher, which logically should have resulted in shorter initiation lives. Therefore, to fairly compare the two splice configurations, Table 6.3 was added, which uses only the $K_{t,S-N} = 3.6$, $R = 0.25$ reference curve for both overlap and butt splices. Indeed, in that case the overlap splices are predicted to initiate sooner than the butt splices, which directly reflects on the stress concentration magnitudes.

For the unnotched case, results in documented in Table 6.1, the choice for reference data was rather straightforward since it was the only dataset available with stress concentration factors below 2. Therefore the data chosen was $K_{t,S-N} = 1$, $R = 0.25$, which resulted in a correction factor simply equal to K_t, according to Equation 3.17.

Table 6.2: Calculation results for the notched samples. For reference data see footnote. $S_{max} =$ 120 MPa, $R = 0.1$ applied loading. Peak stress includes thermal and mechanical stress.

Splice	$\sigma_{peak,max}$[MPa]	R_{peak}[-]	K_t[-]	$S_{a,corr}$[MPa]	N_i[cycles]
OS_0[a]	1024.5	0.14	5.25	47.8	95,664
OS_1[a]	1035.2	0.15	5.3	48.3	91,134
OS_2[a]	1064.1	0.14	5.45	49.6	80,292
BS_0[b]	938.3	0.14	4.81	63.2	62,259
BS_1[b]	923.5	0.14	4.73	62.2	67,329
BS_2[b]	915.3	0.15	4.69	61.7	70,369

[a] $K_{t,S-N} = 5.2$, $R = 0.25$ reference data used, [b] $K_{t,S-N} = 3.6$, $R = 0.25$ reference data used [16]

Table 6.3: Calculation results for the notched samples. $K_{t,S-N} = 3.6$, $R = 0.25$ reference data used [16]. $S_{max} = 120$ MPa, $R = 0.1$ applied loading. Peak stress includes thermal and mechanical stress.

Splice	$\sigma_{peak,max}$[MPa]	R_{peak}[-]	K_t[-]	$S_{a,corr}$[MPa]	N_i[cycles]
OS_0	1024.5	0.14	5.25	69.0	40,428
OS_1	1035.2	0.15	5.3	69.7	38,431
OS_2	1064.1	0.14	5.45	71.7	33,574
BS_0	938.3	0.14	4.81	63.2	62,259
BS_1	923.5	0.14	4.73	62.2	67,329
BS_2	915.3	0.15	4.69	61.7	70,369

This prediction data, alongside the experimental results, are depicted in Figure 6.23, Figure 6.24, and Figure 6.25.

6.3 Experimental results

To assess fatigue performance of each configuration two types of data have been extracted during the experiments: Digital Image Correlation (DIC) capturing the damage progression from the front and back surfaces of the splice, and peak and valley displacement values to capture the changes in stiffness of the specimens.

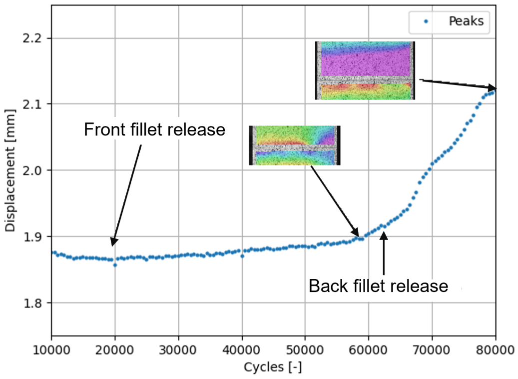

Figure 6.9: OS_0 under $S_{max} = 250$, $R = 0.1$. Front fillet release observed around 20,000 cycles, followed by a delamination of the corner, that most likely indicates a crack initiaton around 60,000 cycles. Crack causes a rapid change in compliance, judging by the gradient of displacement peaks, that later results in complete through-width crack and delamination.

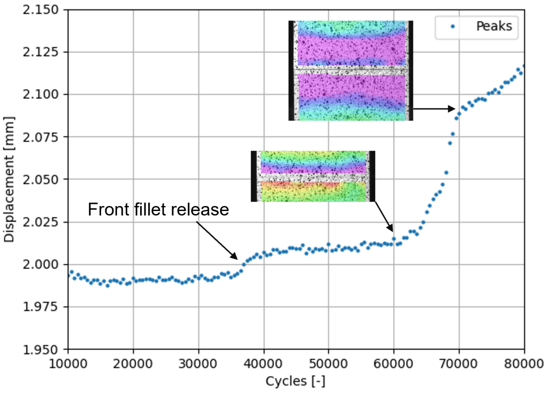

Figure 6.10: OS_1 under $S_{max} = 250$, $R = 0.1$. Front fillet release around 36,000 cycles, followed by initiation of the crack around 60,000, causing sub-surface aluminium layer failure and increase delamination growth.

6.3.1 Peak-Valley analysis

Since the loading was performed under force-control, changes in displacement values, and thus changes in the overall stiffness of the joint, have been recorded during the course of each test, which could point to different fracture and damage events in the splice. By looking at such events and correlating them with the DIC data, it is possible to reverse-engineer the fracture mechanism and point to start of damage accumulation. The legend for DIC strains are not shown because the images are used rather qualitatively. The purple regions in the images are delaminated or load-free areas, with strains approaching zero or even being negative. The red areas are areas of high strain. The ’front’ of the specimen refers to the flush side, and the back refers to the the non-flush side, as that is how the specimen was situated in the test set-up.

Unnotched

It is difficult to see initiation in the unnotched specimens solely from the DIC images, since the layer that is experiencing the highest stresses and therefore fatigue damage initiation is a subsurface layer. However, when looking at the displacement peaks (or valleys) recorded during the fatigue tests, distinctive changes are observed, which further point to change in stiffness of the overall joint, and therefore damage.

Figure 6.9 to Figure 6.14 show the peaks of the displacement cycle during fatigue loading. Corresponding snippets of DIC images are shown inside the plots. While explicit crack growth is not visible from such images, delamination caused by the crack development is, characterised by purple regions of zero or even negative strain. For OS_0, OS_1, BS_0, and BS_1 the fracture mechanism sequence suggests that crack growth occurred 30,000 - 45,000 cycles after the adhesive fillet release and shear cracking of the adhesive, see Figure 6.1 and Figure 6.2. This also means that the predictive model described in chapter 4 is only valid for the aforementioned splices and not the OS_2 and BS_2 configurations, as it predicts metal fatigue initiation and not delamination initiation.

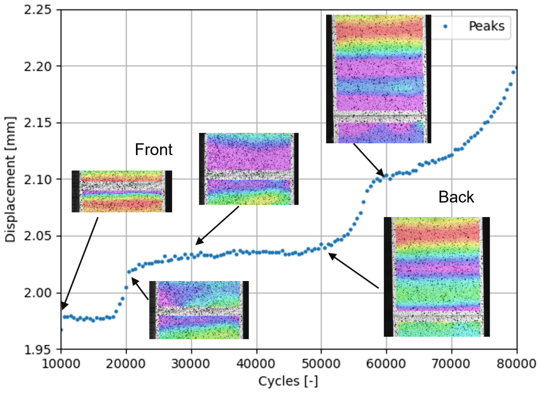

Figure 6.11: OS_2 under $S_{max} = 250$, $R = 0.1$. Front fillet release around 20,000 cycles, promoting delamination growth in the front and later in the back, around 55,000 cycles. Failure likely around 70,000-75,000 cycles due to a rapid change in compliance, judging by sharp increase in displacement peak gradient.

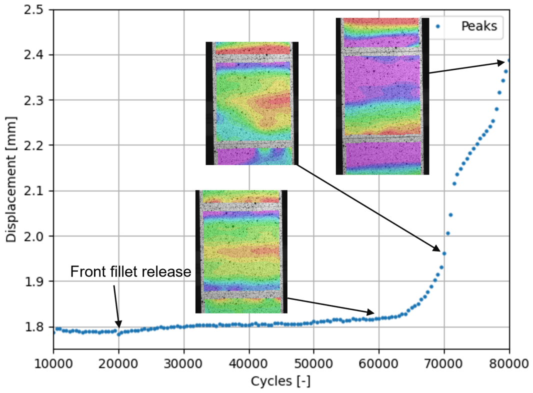

Figure 6.12: BS_0 under $S_{max} = 250$, $R = 0.1$. Front fillet release around 20,000 cycles, followed by a crack initiation around 64,000, causing a sharp increase in gradient, resulting in growing delaminations from the fillet-aluminium interfaces.

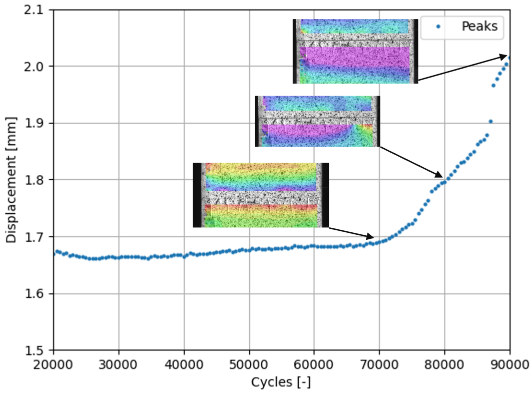

Figure 6.13: BS_1 under $S_{max} = 250$, $R = 0.1$. Front fillet release likely around 30,000 cycles, followed by crack initiation around 70,000 cycles, resulting in rapid change of gradient, attributed to crack and delamination growth.

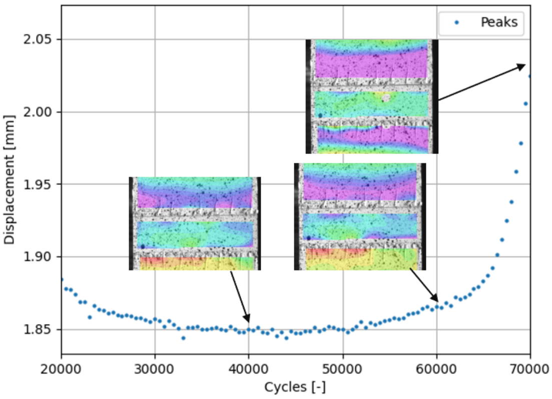

Figure 6.14: BS_2 under $S_{max} = 250$, $R = 0.1$. Front fillet release likely around 30,000-40,000 cycles, followed by interfacial delamination growth, completely separating the subsurface overlap around 65,000 cycles.

The failure condition is difficult to pinpoint, and therefore failure of the samples is considered when the fibres become the main load bearing components of the FML. This is characterised by a steep linear gradient in the displacement peak curve, example seen in Figure 6.15. Table 6.4 summarises fatigue performance of the unnotched samples. The percentage differences in performance are calculated using original designs as reference. First iterations of the original design showed slight improvement in damage initiation performance. Damage initiation is not defined for second design iterations since delamination was observed instead of metal fatigue cracking. The butt splices have encountered initiation of damage later than the overlap splices, on average they reach failure slightly sooner, at 80,500 cycles vs 86,000 cycles, suggesting a faster crack growth phase.

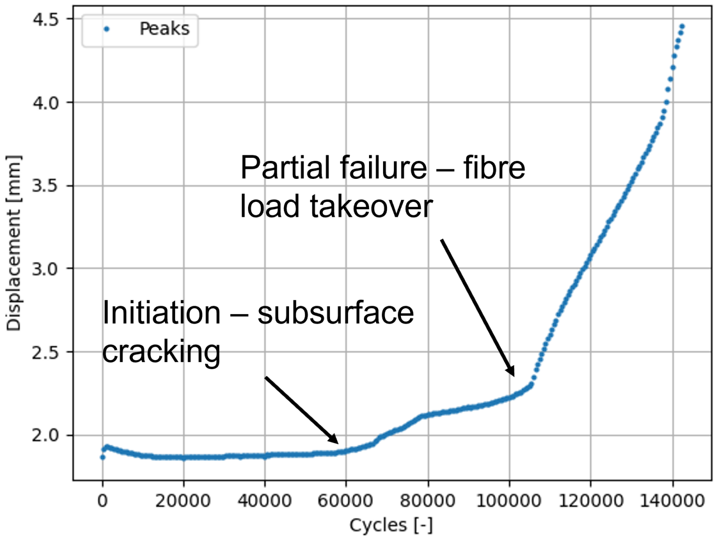

Figure 6.15: Full displacement peak history of an unnotched OS_0 specimen, pointing to first layer failure, i.e. initiation, and fibre load takeover, i.e. partial failure.

Table 6.4: Fatigue performance of unnotched specimens.

Specimen	N_i [cycles]	N_f [cycles]	Difference N_i[%]	Difference N_f[%]
OS_0	58,000	105,000	-	-
OS_1	60,000	78,0000	+3.4	-34.6
OS_2	-	75,000	-	-40.0
BS_0	64,000	83,000	-	-
BS_1	70,000	92,500	+9.4	+10.3
BS_2	-	66,000	-	-25.6

Notched

When looking at the history of displacement peaks depicted in Figure 6.17 to Figure 6.22, there is no clear pattern in the test cases, apart from a gradual increase in displacement peaks indicating damage growth in the joint. Therefore displacement peaks of the notched

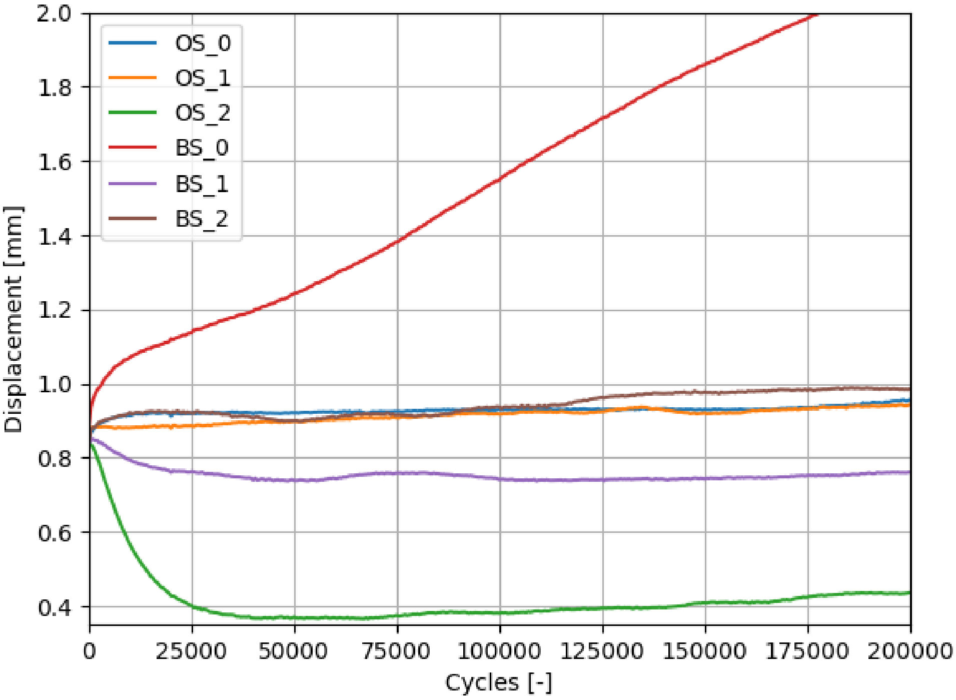

Figure 6.16: Displacement peaks in each of the notched samples, compared with one another. OS_0, OS_1, and BS_2 showcase very similar levels of compliance to mechanical loading, which is not the case for other samples. BS_0 is speculated to have had slip in the grips, causing a steep positive gradient. The causes for the downward trends in BS_1 and OS_2 are unclear.

specimens were not used to evaluate the fatigue initiation lifetimes. Instead, they are used to showcase the difference in methods used to evaluate fatigue damage initiation and partial failure lifetimes in unnotched vs. notched specimens. Moreover, tests of BS_0, BS_1, and OS_2 showcase significant deviation from the starting displacement peak values, which is depicted in Figure 6.16.

Unlike for the unnotched case, the DIC images enabled an easy detection of crack initiation in the notched samples, defined to be a crack of ≈ 1 mm [4]. The initiation of fatigue damage lives based on the cycles to 1 mm crack around the notch that was captured by the cameras is documented in Table 6.5. The initiation lives are accurate to 5,000 cycles because of the cycle interval between photographs. Further, it is assumed that the surface layer cracking that is captured by the DIC cameras occurs simultaneously with the subsurface cracking. This assumption leads to an error in recorded vs. real fatigue damage initiation lives, as it is known from the FEA and the unnotched test cases that the subsurface layer exhibits fatigue damage first rather than the surface layer. The error is likely small[2] due to the stress redistributed from the subsurface crack and adhesive fillet release and the notch itself resulting in almost simultaneous cracking of the surface layer too.

---

[2] The exact quantification of it would only be possible with subsurface damage detection techniques, such as ultra-sonic scanning of the specimens.

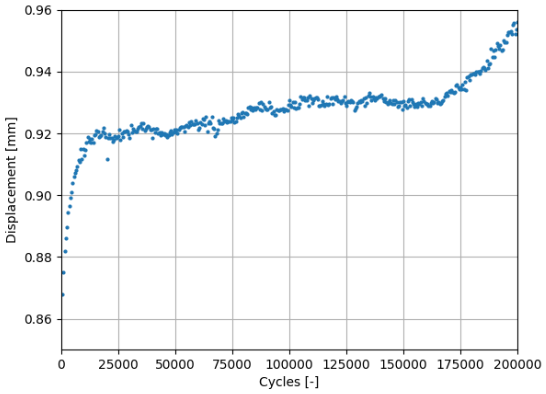

Figure 6.17: OS_0 under $S_{max} = 120$, $R = 0.1$. Initiation occured around 60,000 cycles, which is not reflected in the displacement data. Full width crack is reached around 180,000 cycles, which falls within the stiffness decrease seen after 175,000 cycles.

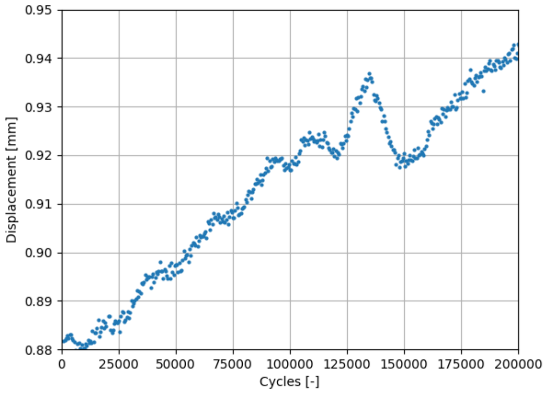

Figure 6.18: OS_1 under $S_{max} = 120$, $R = 0.1$. Crack initiated around 60,000 cycles, which is not reflected in the displacement data. A crack reached full length around 154,000 cycles, which may have caused an increase in the gradient after a valley seen around 150,000 cycles.

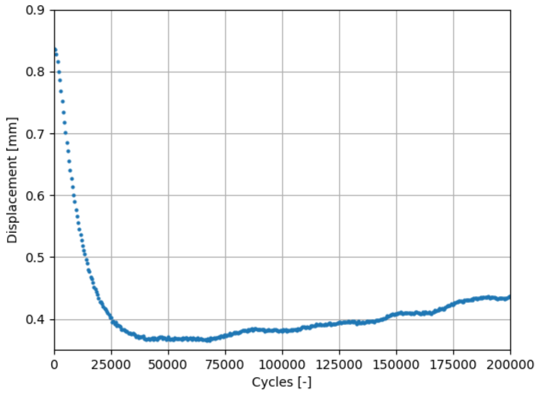

Figure 6.19: OS_2 under $S_{max} = 120$, $R = 0.1$. Initiation occurred around 80,000 cycles and full width crack at 142,000. The cause for the negative gradient in displacement peaks, indicating overall stiffening of the structure, is uncertain.

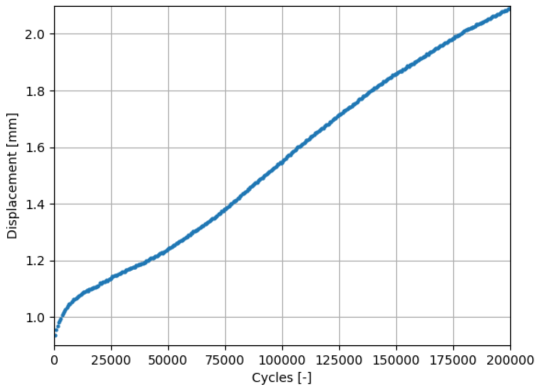

Figure 6.20: BS_0 under $S_{max} = 120$, $R = 0.1$. Given a very steep gradient, it is speculated that the sample slipped between the grips during the fatigue test, causing excessive elongation that cannot be attributed to mechanical loading. The slip, however, does not affect the initiation of fatigue damage since the loading is force controlled.

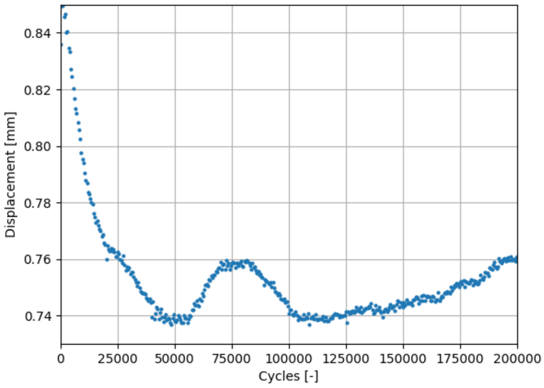

Figure 6.21: BS_1 under $S_{max} = 120$, $R = 0.1$. The cause of the sharp drop in displacement is unclear. Overall, it is difficult to attribute any displacement peak changes to damage events transpired during the testing. The cause for the stiffening of the joint depicted by the negative displacement gradient is uncertain.

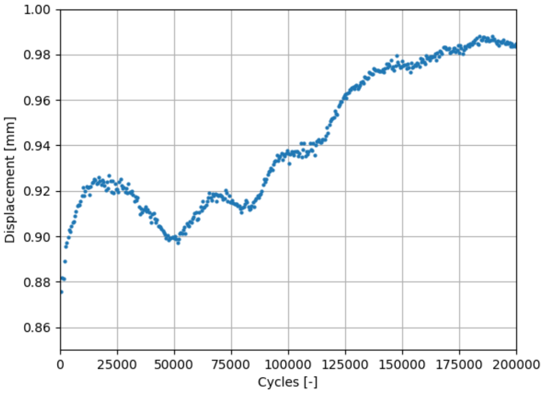

Figure 6.22: BS_2 under $S_{max} = 120$, $R = 0.1$. Crack initiation began at 80,000 cycles, causing a gradient increase.

Sample failure is quantified by a means of a full crack through specimen's width, which was again easily visible from the DIC imaging. The initiation and failure lives are showcased in Table 6.5. Butt splices showed a slightly delayed initiation and full crack length when compared to the overlap splices. Surprisingly, the second iteration of the overlap splice showed a significant improvement in damage initiation life.

Table 6.5: Fatigue performance of notched specimens.

Specimen	N_i [cycles]	N_f [cycles]	Difference $N_i[\%]$	Difference $N_f[\%]$
OS_0	60,000	180,000	-	-
OS_1	60,000	154,000	0.0	-16.9
OS_2	80,000	142,000	+33.3	-26.8
BS_0	85,000	184,000	-	-
BS_1	85,000	206,000	0.0	+10.7
BS_2	80,000	170,000	-17.6	-8.2

6.3.2 Predicted vs. experimental fatigue damage initiation

Notched specimens

Figure 6.23 showcases the initiation fatigue lives in the notched splices, loaded under $S_{max} = 120$, at $R = 0.1$. The stress amplitudes $S_{a,net}$ used are resulting from Equation 3.16, which provides a stress amplitude that can be fairly compared to the reference data used. Evidently, there is a good agreement between the predicted and test outcomes. The error resulting from the DIC capturing the initiation in surface layer instead of the subsurface one would

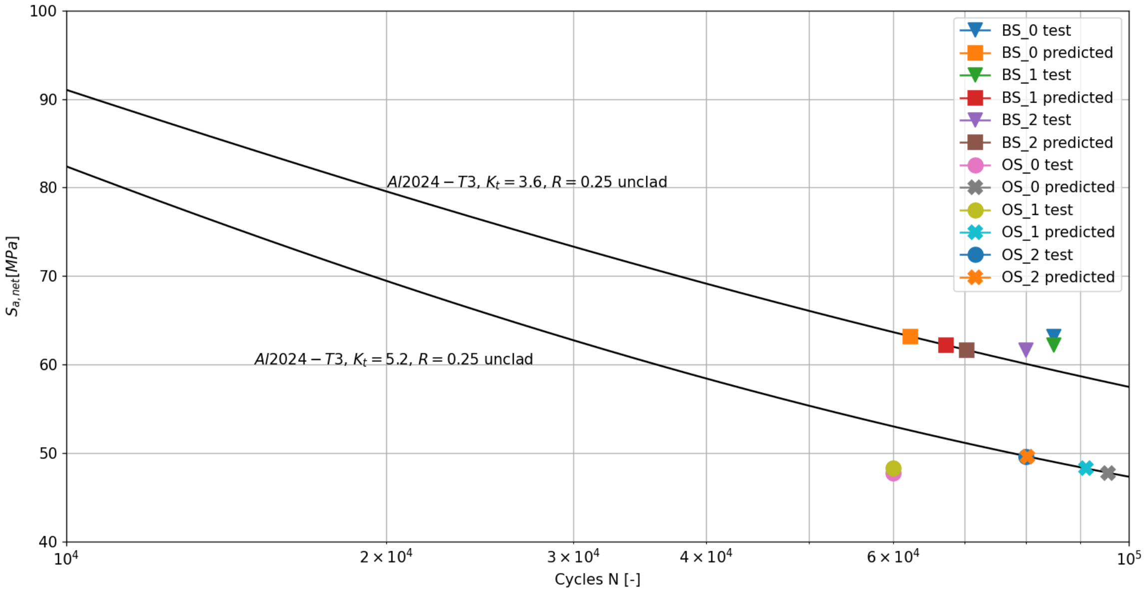

Figure 6.23: Predicted vs observed initiation fatigue lives in notched splices loaded under $S_{max} = 120\text{MPa}$, $R = 0.1$. The plots are of reference data used.

actually further improve the agreement between the butt splice predictions and experimental results by shifting the test results closer to the reference curve, see Figure 6.23. Contrary to that, the agreement between findings of overlap splices and predictions would shift further away from the reference curve, making the predictions worse, see Figure 6.23. Overall, butt splice predictions appear to be conservative, while the overlap splice predictions appear to be unconservative. Most predictions are within 20,000 cycles of the test outcome, except for overlap splices, that are around 35,000 cycles away from the predicted value. It is also important to note that the butt splice fatigue initiation lives have been based on the reference case with $K_t = 3.6$, while the overlap splice initiation lives used $K_t = 5.2$ as reference data. This was done to closely match the test data to the reference data, as was suggested by paper where this prediction method is put forward [12]. Moreover, all the test cases have initiated fatigue damage at cycles equal or exceeding 60,000 cycles, more than the number of ground-air-ground cycles allowed by the single-aisle short-range aircraft, like the Airbus A320, being 48,000 cycles [50]. This suggests that even with a severe damage such as an open hole at the most critical location of the splice, which is unlikely, the structure would allow for several thousands of flights without accumulating significant fatigue damage before a thorough inspection and repair is performed.

Predictions displayed in Figure 6.23 suggest that the overlap splices initiate damage later than the butt-splices. This is inconsistent with both experimental findings and FE findings. Therefore, to investigate this, both splices have been compared to the same reference curve, with the results of this shown in Figure 6.24, and errors computed in Table 6.7. Predicted initiation lives for overlap splices then agree with experimental findings and are shorter than the initiation lives of the butt splices, but the overall agreement of experiments and the predictions is then worse. For this reason it is important to look at both datasets, since Figure 6.23 shows a better agreement with experiments but does not show a realistic comparison between overlap splice and butt splice performance, and Figure 6.24 does the opposite.

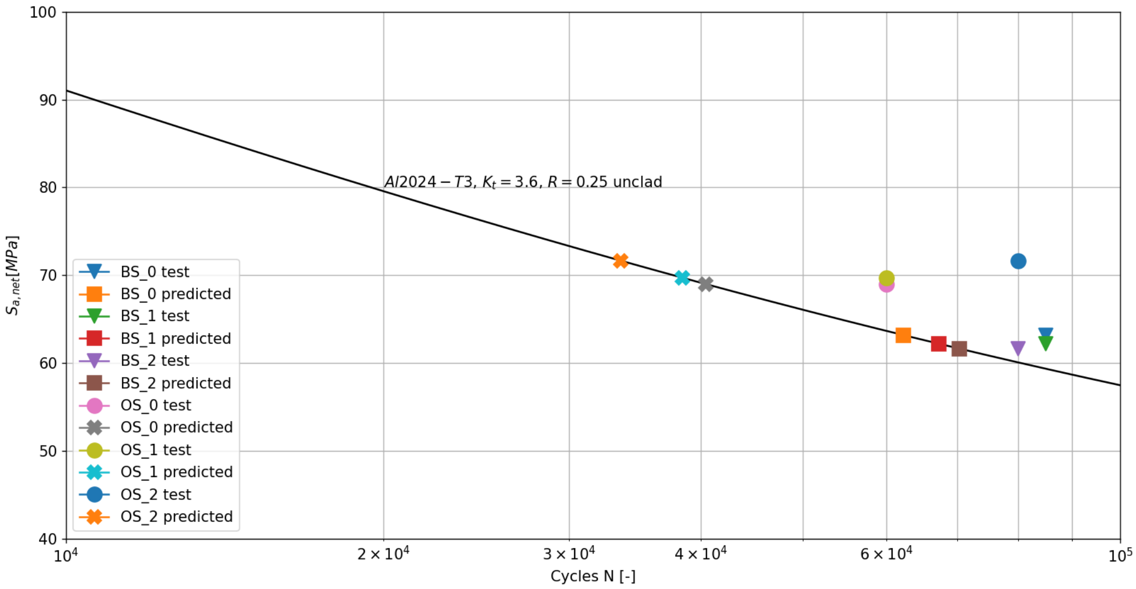

Figure 6.24: Predicted vs observed initiation fatigue lives in notched splices loaded under $S_{max} = 120$MPa, $R = 0.1$ on the same reference data.

Unnotched specimens

Predicted values for the unnotched cases, tested at $S_{max} = 250$, $R = 0.1$, disagree significantly from the test results, see Figure 6.25. The predictions are extremely unconservative, predicting the initiation lives to be close to 1M cycles, while the test data suggests initiation around 40-80k cycles. It is unknown exactly why there is such a big discrepancy, but it is likely that it is a result of several causes present simultaneously.

1. For the unnotched case, the dimensions of the coupon play an even bigger role. It is difficult to predict where the fatigue crack would initiate. Ideally, the notch should start from the sides of the coupon at the microscopic inclusions due to the sawing and milling of the samples. However, it is possible that a crack also begins to form in middle of the coupon due to stress concentrations caused by the crack in the adhesive. Therefore, in the unnotched case, a multiple site damage is likely, making difficult to define initiation of damage.

2. It is likely that preceding adhesive fillet release and then adhesive cracking, see Figure 6.1 and Figure 6.2, caused a severe stress concentration than, causing the fatigue crack to initiate much earlier. This is a common occurrence for FMLs, where it was often observed that a matrix crack initiated a metal fatigue crack in the adjacent metal layers [4].

3. Following on the previous point, this underestimated stress concentration would consequently cause an incorrect pick for the reference data used. The method is described to

be very sensitive to the reference data, and thus creating an even larger disagreement between predicted and experimental outcomes.

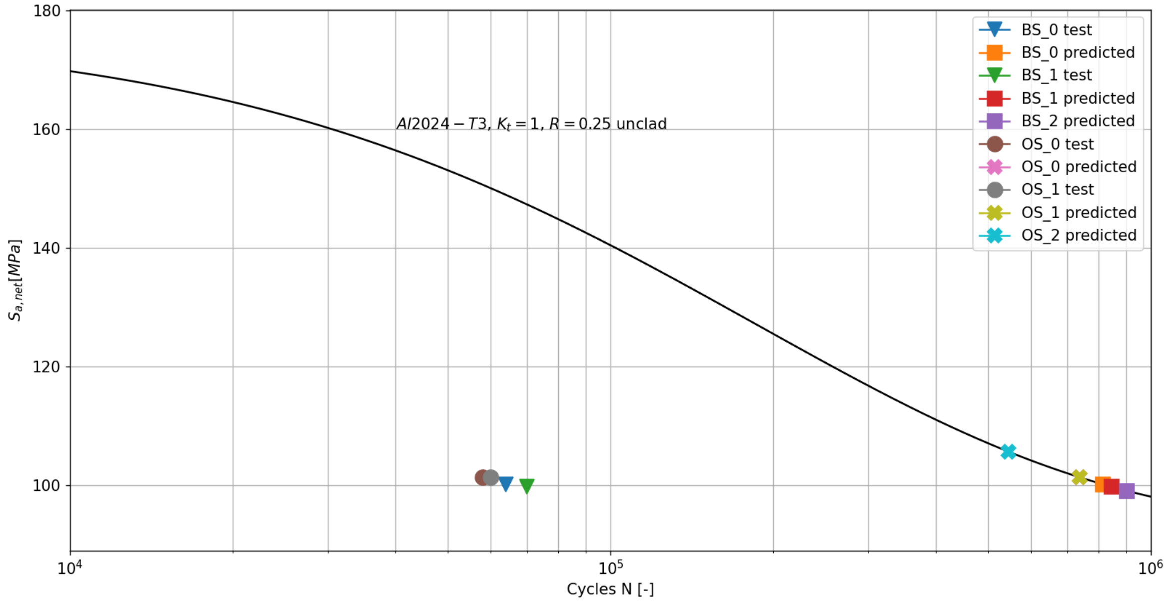

Figure 6.25: Predicted vs observed initiation fatigue lives in unnotched splices loaded under $S_{max} = 250$MPa, $R = 0.1$.

6.4 Discussion

6.4.1 Result summary

The tests showed consistency in damage propagation in the splices, beginning with adhesive fillet release, followed by a shear cracking of the adhesive or slight disbond, continuing as metal cracking of the adjacent aluminium layer. The same damage progression was observed by other researchers at much lower stress levels too. For the smallest joints, BS_2 and OS_2, fillet release acted as an onset to disbond of the overlaps instead of metal fatigue. When regarding the notched specimens, all specimens displayed the onset of damage in form of the metal fatigue cracks around the notch, as well as fillet release, again starting from the notch. Like predicted by the Finite Element (FE) static simulations, the damage always initiated in the flush side of the splice in the outer-most overlap due to secondary bending induced tension. Comparison between the predicted initiation lives and those observed in experiments is given in Tables 6.6, 6.7, and 6.8.

Table 6.6: Prediction vs. experiment fatigue life initiation for notched specimens with only $K_t = 3.6$, $R = 0.25$ and $K_t = 5.2$, $R = 0.25$ reference datasets.

Specimen	Predicted N_i [cycles]	Actual N_i [cycles]	|Error| [%]
OS_0	95,665	60,000	59.4
OS_1	91,134	60,000	51.9
OS_2	80,292	80,000	0.4
BS_0	62,259	85,000	26.8
BS_1	67,329	85,000	20.8
BS_2	70,369	80,000	12.0

Table 6.7: Prediction vs. experiment fatigue life initiation for notched specimens with only $K_t = 3.6$, $R = 0.25$ reference dataset.

Specimen	Predicted N_i [cycles]	Actual N_i [cycles]	|Error| [%]
OS_0	40,428	60,000	32.6
OS_1	38,432	60,000	35.9
OS_2	33,574	80,000	58.0
BS_0	62,259	85,000	26.8
BS_1	67,329	85,000	20.8
BS_2	70,369	80,000	12.0

Table 6.8: Prediction vs Experiment fatigue life initiation for unnotched specimens

Specimen	Predicted N_i [cycles]	Actual N_i [cycles]	|Error| [%]
OS_0	738,516	58,000	>100
OS_1	738,516	60,000	>100
OS_2	545,285	-	-
BS_0	816,378	64,000	>100
BS_1	845,062	70,000	>100
BS_2	903,740	-	-

Provided that damage propagation followed a similar pattern at $S_{max} = 250$ MPa, $R = 0.1$ loading and at $S_{max} = 150$ MPa, $R = 0.1$ loading in different splices, it is suggested that such a damage propagation is to be expected at other stress levels and other splice configurations with similar features. Moreover, this means even at high stress levels it is still possible to accurately compare splices in terms of fatigue performance without altering the way that initial damage accumulates in the splice.

Judging from both notched and unnotched specimens, see Figure 6.26 and Figure 6.27, the overlap splice performs worse than the butt splice when it comes to damage initiation, which is also predicted by the FE simulations, and the predictive model, where the overlap splice shows a higher stress concentration in the critical area while the same load level is applied. Despite this, from Figure 6.27 it is evident that the unnotched overlap splices fail later than the unnotched butt splices, suggesting a more damage tolerant design. This trend is reversed in the notched samples, as seen in Figure 6.26, and therefore it it difficult to conclude whether

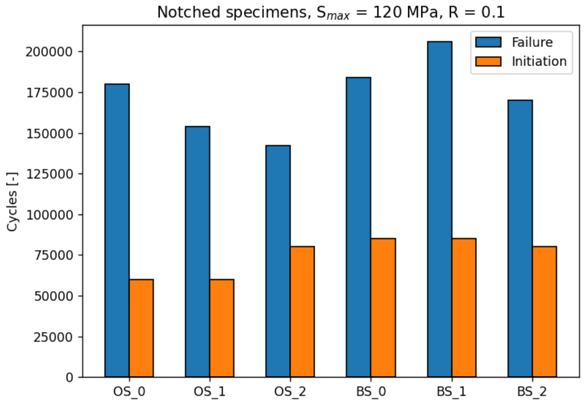

Figure 6.26: Fatigue performance of the notched specimens, from physical experiments. Based on data in Table 6.5.

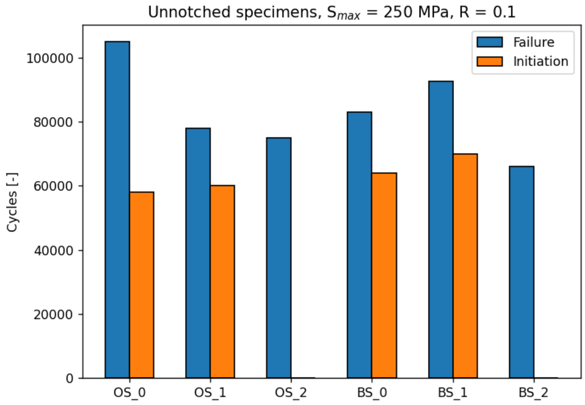

Figure 6.27: Fatigue performance of the unnotched specimens, from physical experiments. Based on data in Table 6.4.

the overlap splice or the butt splice is more damage tolerant. Overall, damage initiation phases seem to remain relatively unchanged with design iterations, taking into account that damage initiation is a subject to scatter.

Nevertheless, the performance of all splice configurations is good, indicated by substantial number of cycles to initiation that exceeds 48,000 cycles set by EASA [50]. Further, judging from test results of the unnotched BS_2 and OS_2 samples tested at $S_{max} = 120$ MPa for 600,000 cycles without revealing any significant damage, the designs can be declared to be of good durability. From Table 4.8, the OS_2 configuration is dramatically lighter than its competitors. Therefore, deciding on which splice configuration is superior depends on the trade-off between durability and weight.

It can be further concluded that the methodology utilised to predict the initiation of damage in spliced FMLs is accurate when a notch is present, based on Figure 6.23, but is not accurate without the notch, based on Figure 6.25. Further, it is highly sensitive to the reference data used, which was already concluded by the inventors of the method [12]. When computing predictions for the notched overlap splices using the $K_t = 3.6$ data, rather than $K_t = 5.2$, the average error of the predictions increases, but provides a better comparison of the performance between the two splice types, see Table 6.7. Regardless, both datasets lead to a good agreement with the experiments of the notched splices. Predictions of fatigue damage initiation lives in the unnotched specimens, however, are orders of magnitude off, and therefore the prediction methodology cannot be validated in that case. It is anticipated that this discrepancy is caused by a combination of factors, such as a mismatch in the real and predicted stress concentrations of the metal layers, and the consequent selection of the wrong reference data.

It is expected that with a better FE model that takes into account damage propagation and reference data that closely matches the test case, it would be possible to predict metal fatigue initiation in the unnotched samples too. Needless to say, the fatigue damage initiation prediction methodology would only be valid if the fatigue takes form of a metal cracking instead of disbonding of the outer overlaps, like was the case with the unnotched BS_2 and OS_2 samples.

6.4.2 Road to certification

Results and findings provided in this research offer a promising pathway for alternative splice designs that could potentially be seen in FML structures in the future, specifically those subjected to fatigue loading. This is because of the fact that, although the test results showcase that the smallest splice coupons, BS_2 and OS_2, remain free of damage for more than 600,000 cycles of $S_{min} = 12$ MPa and $S_{max} = 120$ MPa without the notch, and more than 60,000 cycles of the same loading with a notch in the most critical location, they still represent an extremely simplified part of an aircraft structure - a coupon. It's crucial to emphasize that safety and adherence to regulations are paramount in the aviation industry. In order to draw a concrete conclusion on whether the updated splices are a feasible joining solution to FML panels, more rigorous testing is necessary that would progressively resemble the final structure intended for splice use, see Figure 6.28. Additionally, the splice would not only have to be placed in a more realistic structure but also environment. This involves tests that investigate the effects of temperature, humidity / moisture and UV exposure on the joint.

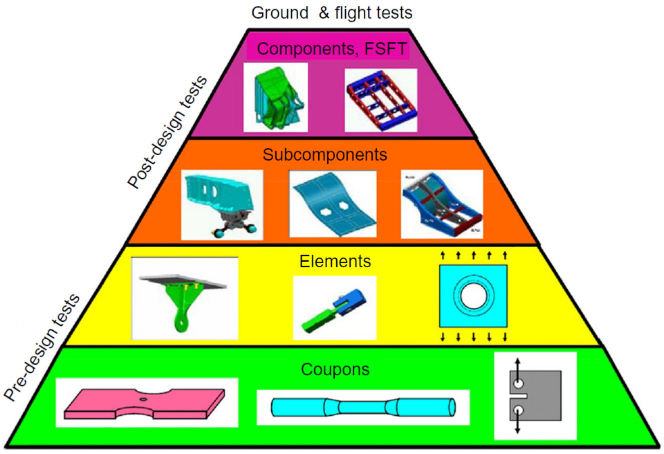

Figure 6.28: 'Building Block' fatigue test approach for aircraft structures and materials. From [13].

Given that the splice is an adhesive joint that joins both composite and metallic components, damage tolerance plays an important role in certification. Composites and adhesives exhibit adverse drops in load carrying capabilities once damaged [51]. While the experimental results obtained in this research show a good fatigue performance, although this would have to be confirmed by more populous data sample to provide statistical confidence in the results, damage tolerance has been hardly investigated. Configurations BS_0, BS_1, OS_0, and OS_1 behaved more and less like an uninterrupted FML, by showcasing damage initiation in a form of metal cracking. BS_2, OS_2 behaved like an adhesive joint, by exhibiting fatigue damage as disbond of the outer-most overlapping metal layer, pointing to a need of a damage tolerant design. This means that in addition to the element, sub-component, and component tests depicted in Figure 6.28, and aforementioned environmental tests, there is a need for fatigue and residual strength tests with damaged specimens. Depending on the type of structure, be it of primary or secondary type, these tests would have to involve damage of different categories that are based on the severity of such damage, for instance barely visible impact damage or more apparent damage. Barely visible damage would have to be showcase the ability to cycle for the aircraft's lifetime with an additional safety factor[3], and after a critical damage the splice would have to prove that it can facilitate a safe landing, withstanding 75% of the limit load, according to the FAA and NATO [51].

6.5 Proposed splice design guidelines

To answer the third and final research sub-question, additional design guidelines are suggested that could expand the design guidelines found in literature [6, 26, 31].

1. Placement of details within the splice can be closer than previously thought. It was suggested by Van Tongeren [31] that splice details are placed at least 20 mm apart from each other. This suggestion was based on a criteria that the loads must be redistributed back to their 'farfield' state, however, the increases in local stresses around the details were found not to be significant. Placing the details closer than 20 mm does not result degradation of fatigue strength. Despite that, it is not advisable to place details closer than 5 mm because that might induce premature damage and rapid delamination of the overlaps.

2. It has been found that stress concentrations in the overlap splice are higher than the butt splice, a cause of the more prominent secondary bending effects. The secondary bending effect is expected to increase with overlap splices in thicker laminates, for instance 4/3, 5/4, or 6/5. This is not the case with the butt splice, where the secondary bending effect would diminish with the thicker laminates as the neutral axis shift would become less significant. Therefore it is just suggested that for thicker laminates, the butt splice is used instead of the overlap splice.

3. The location that attracted the most damage in both splices was the overlap run-out on the flush side of the splice. Although having a flush side to the splice is desirable for both manufacturing and aerodynamic purposes, it is not advantageous structurally. This negative effect can be minimised by providing a longer adhesive fillet on the flush side of the splice, such that there is less curvature to the splice at joint boundaries.

4. Splice parameters in Figure 3.1 can be dimensioned at 5 mm, where the butt joints can have a gap of 2 mm. This is based on the successful tests of the lightest splices, which bore loads of $S_{max} = 120$ MPa for 600,000 cycles without revealing any damage. Further, from studies of Out [32], static strengths should not be affected by splice tolerances.

---

[3] Safety factor depending on the type of testing done. For coupon tests this safety factor is around 3 and 5, for sub-assembly tests this as low as 1.5.

Chapter 7

Conclusion & Recommendations

This chapter serves as concluding chapter of this report and this research. First, conclusion of the research that answers the research questions proposed is detailed in section 7.1, and then recommendations for future research are suggested in section 7.2.

7.1 Conclusion

To provide a complete and thorough closure to this research, it is important to recall to the main question of this research:

How do the splice tolerances affect fatigue life performance of a complete splice?

Since the splice joint can be seen as a collection of structural joints, each of those joints and distances between the joints were parametrically studied to reveal the influence of each detail on the complete splice structure. FEA revealed that varying the parameters selected, see Figure 3.1, resulted in peak stress changes under 5 MPa when comparing the biggest and the smallest tolerances, therefore the splice was systematically shrunken to potentially lead to a more lightweight design without sacrificing fatigue performance.

When it comes to experimental findings, it lead to observations of a systematic decrease in fatigue performance in smaller splices if looking at failure lives, varying between -16% and -40%. Interestingly, BS_1 consistently showed a 10% increase from the baseline fatigue failure life in both unnotched and notched cases. Contrary to that, damage initiation lives have shown to remain relatively the same through design iterations. It was further revealed that even the lightest designs, BS_2 and OS_2, despite the drop in fatigue performance, did not exhibit any fatigue damage up to 600,000 cycles while loaded at stress levels similar to those encountered during a typical ground-air-ground cycle: S_{max} = 120 MPa, at $R = 0.1$. Despite all that, when testing BS_2 and OS_2 at a high stress level of S_{max} = 250 MPa, more than double that of a realistic loading, a difference in damage propagation was observed when compared to OS_0, OS_1, BS_0, and BS_1. After the expected adhesive release, the sample then showcased a complete disbond of the external overlaps. This was not the case in other splice samples, which all consistently developed damage in a form of adhesive fillet release, adhesive cracking and metal fatigue cracking of the subsurface layers, in that respective order. It is thus possible to conclude that durability of even the most lightweight designs remains more than satisfactory, however the most lightweight designs with tightest tolerances resulted in an alternative damage progression in a form of an disbond in the metal overlaps, creating concerns over damage tolerance of such configurations.

In the process of answering the main research question, a methodology was developed that involves numerical and FE modelling. One of the research sub-questions was:

Is it possible to accurately predict the location and lifetime of damage onset in spliced Fibre Metal Laminates?

To answer this sub-question, an FE model was built in ABAQUS that models FML as a 3D solid, with every constituent modeled separately and later 'glued' together via a tie constraint. The model was aimed towards a better understanding of the stress field in the splice joint, and extracting the needed parameters, such as local axial, shear and peel stresses, to perform quantitative analysis of the splice configurations. The model was able to predict exactly where the damage would initiate within the splice, and further was able to predict damage progression after manual adjustments to the model that took into account the damage that has already occurred. This artificial damage in the FE model was based on the damage that has occurred during the experimental program.

Internal stresses around the location with highest stress concentration, which in all cases was the reinforcement doubler run-out on the flush side of the splice, were obtained from FEM and used in an adapted version of the prediction model developed by Spronk et al. [12]. The prediction model was meant to predict initiation of fatigue damage in Fibre Metal Laminates based on the reference data of monolithic metal alloys. An adapted model was used to achieve the same purpose for a spliced FML. There is a very good agreement with the experiments conducted on the notched samples, with predictions of fatigue initiation being on average only 28% off, which for initiation of fatigue is a good margin due to the known high degree of scatter in the phenomenon. The method, however, resulted in very poor agreement in the unnotched cases. The discrepancy was likely caused by an underestimations of stress concentration in the critical area, and the consequent wrongful choice of the reference data used in the predictions.

Which splice configuration possesses superior mechanical performance - the overlap splice or the butt splice with external doubler straps?

With the FE and experimental results it was possible to evaluate the performance of the two splice types, the butt splice and the overlap splice, and their respective configurations. The overlap splice showed a higher stress concentration in the critical area, which lead to a quicker initiation of damage when compared to the butt splice. For the notched samples, this also lead to a quicker failure. For unnotched samples, although the overlap splice reached the point of damage initiation sooner than the butt splice, failure in some cases occurred later than the butt splice, suggesting a more damage tolerant design. However, this was an isolated case where the overlap splice performed better than the butt splice, and since it is initiation of damage that is driving fatigue performance indicator here, it is concluded that the butt splice possesses better fatigue performance than the overlap splice. It is crucial to note that this competition is relative to the cases studied and that both splices showed good fatigue performance, with notched cases tested at $S_{max} = 120$ MPa initiating damage between 60,000 and 85,000 cycles, and unnotched samples tested at $S_{max} = 250$ MPa initiating damage around 58,000 to 70,000 cycles. When considering the weight of joint, the overlap splices appear to be lighter which is also directly but not exclusively related to their smaller size.

What design guidelines shall be followed when designing splice joints in FMLs, aimed for improved fatigue performance?

Having analysed the data and answered the previous sub-questions, it was possible to derive splice design guidelines that could then be used to simplify the design domain of these joints.

1. The splice details can be placed closer than 15 or 20 mm, which was previously thought by Van Tongeren [31]. The details could be placed as close as 5 mm away from one another, and has been proven to work by tests on splices having these dimensions, exhibiting no damage for 600,000 cycles, after which the tests were stopped.
2. The overlap splice leads to more severe secondary bending than the butt splice, an observation supported by both FE calculations of peak axial stresses and shorter damage initiation lives recorded from the experiments. This trend is expected to deteriorate in thicker overlap-spliced laminates. The butt splice is therefore recommended in thicker laminates as it dissipates secondary bending effects with increasing thickness or the number of layers in the laminate.
3. Longer fillets on the flush side of the splice are proposed to minimise the severity of the critical area of the joint. Longer fillets would reduce the curvature of the laminate around the reinforcement run-out, resulting in less stresses in the vulnerable area.
4. Parameters studied within the splices, particularly **b**, **c**, and **d** seen in Figure 3.1, can be as small as 5 mm, with butt widths (**a**) as small as 2 mm.

7.2 Recommendations

Throughout the course of this research, several recommendations became obvious and are thought of as benefit to any future researchers on a similar topic.

Modelling recommendations

The FE model built was a quasi-static model with no damage modelling. Therefore, any damage of interest observed in the experiments had to be added artificially. It is therefore recommended that a future iteration of the model described in this report is enriched with:

- Cohesive zone model in the interfacial boundaries between metal and composite layers, specifically in the external overlaps as it has been observed that damage is initiated in those areas.
- Modelling of every composite layer individually, rather than having a smeared model of a composite laminate modeled as a solid. This way, a fibre failure model could be added in order to predict if there is going to be fibre failure after preceding delamination, what is speculated to have happened in the case of OS_2, the smallest overlap splice.
- A curing simulation that can bring the stress state of the splice closer to reality by introducing residual stresses, which could then be compared with the numerically superposed thermal residual stresses used in the model of this research.
- Clamping areas of the specimen should be modeled to accurately evaluate the deformation behaviour of the specimen, which is expected to bring the model closer to the real-life case.

Manufacturing recommendations

During the manufacturing of splices, it is advised that each aluminium layer is cut to its precise dimensions from the start, such that the ends of the sample plate could be used a datum during the hand layup. Although this might seem like a tedious task, it would save a lot of time during the hand layup process and keep the dimensions within tighter tolerances. Regardless, hand layup would cause deviation of ±1 mm from the desired dimensions, therefore these must be taken into account. Further it is recommended that clamping tabs are installed on the samples, for instance aluminium or resin tabs. These will prevent damage in the clamping area of the specimen from developing during testing.

Research recommendations

It can be confidently stated that the reinforcement doubler run-out in the flush external overlap is the most critical feature in the splice joint. Therefore it is suggested that research studying efficient manufacturing ways to reduce the curvature of the splice around this run-out could be beneficial to joint fatigue and static performance. Alongside this, the sensitivity of this curvature, or fillet length, could be analysed in order to add to the splice design guidelines already present.

The prediction method in this research yielded good results with notched specimens, contrary to the unnotched specimens. It is expected that with a more advanced FE model, such as the one the described in modelling recommendations, could result in much better agreement with experimental results. Moreover, it was difficult to quantify fatigue initiation in the unnotched specimens as it was impossible to see inside the material, where initiation could begin. A blunt notch on the free edges of the specimen could be used, with DIC cameras focused on this blunt notch from the side, capturing the cross-section of the sample rather than its front and back surface. Other damage detection techniques that capture internal damage could be used, such as acoustic emission recordings or ultrasonic scans.

When it comes to splice design, more parameters could be included in the study, although this is a subject to resource availability. Thicker laminates could be studied to validate the design suggestion outlined in this research that in thicker laminates the butt splice is expected to perform much better than the overlap splice, drawing a more prominent performance gap between the two.

Given that the most lightweight configurations experienced an alternative damage mode that brings concerns over damage tolerance of such a splice, further research that would target static and dynamic splice performance of impact damaged specimens is suggested. This would bring the splice configurations designed in this research thesis closer to their potential certification for use in the aviation industry, or reveal flaws in the design over its damage tolerant capabilities that were not investigated in this thesis work.

And lastly, given the current global concerns for a more sustainable aviation and automotive industries, splice performances using different constituents could provide a new solution to the sustainability problem. For instance investigating mechanical performances of splices in natural flax fibre FMLs. Since flax fibres possess very different properties to glass fibres, it is obvious that both fatigue and static performances would differ, but also the damage modes present in these splices are expected to differ to. This might set a different winner in the butt splice and overlap splice competition.

References

[1] C. Liu and P. E. Linde. Numerical study on the buckling behavior of fiber-metal laminates (FML) with defects. 2009.

[2] A. Vlot and J.W. Gunnink. *Fibre Metal Laminates: an introduction*. Kluwer Academic Publishers B.V., 2001.

[3] G. H. J. J. Roebroeks. EP0983141B1, 2002.

[4] R. C. Alderliesten. *Fatigue and Fracture of Fibre Metal Laminates*. Springer International Publishing AG, 2017.

[5] P. A. Hoojimeijer. Mechanical properties of spliced Glare panels inside doubler & overlap splice configuration. Master's thesis, Delft University of Technology, 1999.

[6] P. A. Hooijmeijer. CONFIDENTIAL report B2V-00-43: overview of mechanical property test on Glare splices carried out between 1997 and 2000, 2000.

[7] W. A. de Ruyter. TZ report: doubler and splice under tensile fatigue loading, 1999.

[8] J. J. Homan. Fatigue initiation in fibre metal laminates. *International Journal of Fatigue*, 28:366–374, 4 2006.

[9] R. C. Alderliesten. *Fatigue Crack Propagation and Delamination Growth in Glare*. PhD thesis, Delft University of Technology, 2005.

[10] H. Quan and R. C. Alderliesten. On the effect of plastic model on simulation of adhesive bonded joints with FM94. *International Journal of Adhesion and Adhesives*, 110, 10 2021.

[11] Dassault Systèmes. SIMULIA User Assistance 2022, 2022. URL: `https://help.3ds.com/2022/English/DSSIMULIA_Established/SIMULIA_Established_FrontmatterMap/DSDocHome.htm?contextscope=all&id=e3e27f055d9b4199959f9082be373cc2`.

[12] S. W. F. Spronk, I. en, and R. C. Alderliesten. Predicting fatigue crack initiation in fibre metal laminates based on metal fatigue test data. *International Journal of Fatigue*, 70:428–439, 2015.

[13] D. L. Ball, D. S. Norwood, and S.C. TerMaath. Joint strike fighter airframe durability and damage tolerance certification. *47th AIAA/ASME/ASCE/AHS/ASC Structures, Structural Dynamics, and Materials Conference*, 2006.

[14] A. S. M. Al-Azzawi, L. F. Kawashita, and C. A. Featherston. A modified cohesive zone model for fatigue delamination in adhesive joints: Numerical and experimental investigations. *Composite Structures*, 225, 10 2019.

[15] M. Zhu, D. Chen, and Q. Hu. Failure mechanisms and reinforcing modes of ply splice fiber-reinforced composite laminates under tensile load. *Materials*, 12, 9 2019.

[16] L. Schwarmann and V. Hoang. Technical report: Fatigue strength of unnotched/notched specimen material: aluminum alloy 2024-T3 unclad. *Handbuch Struktur Berechnung*, 63111-01, 1986.

[17] J. Schijve, H. T. M. van Lipzig, G. F. J. A. van Gestel, and A. H. W. Hoeymakers. Fatigue properties of adhesive-bonded laminated sheet material of aluminum alloys. *Engineering Fracture Mechanics*, 12:561–579, 1979.

[18] L. B. Vogelesang and A. Vlot. Development of fibre metal laminates for advanced aerospace structures. *Journal of Materials Processing Technology*, 103:1–5, 2000.

[19] J. Schijve. Report lr-715: Development of fibre-metal laminates, ARALL and GLARE, new fatigue resistant materials, 1993.

[20] Composites World. The resurgance of GLARE, 2016. URL: `https://www.compositesworld.com/articles/the-resurgence-of-glare`, accessed on 08/12/2022.

[21] S. W. F. Spronk. Predicting fatigue crack initiation and propagation in Glare reinforced frames. Master's thesis, Delft University of Technology, 2013.

[22] T. Sinmazçelik, E. Avcu, M. Ö. Bora, and O. Çoban. A review: Fibre metal laminates, background, bonding types and applied test methods. *Materials and Design*, 32:3671–3685, 8 2011.

[23] Z. Ding, H. Wang, J. Luo, and N. Li. A review on forming technologies of fibre metal laminates. *International Journal of Lightweight Materials and Manufacture*, 4:110–126, 3 2021.

[24] N. M. Ishak, S. D. Malingam, M. Ridzuan Mansor, N. Razali, Z. Mustafa, and A. F. A. Ghani. Investigation of natural fibre metal laminate as car front hood. *Materials Research Express*, 8:025303, 2 2021.

[25] Composites World. SAMPE Europe highlights: Composites face challenges in next commercial airframes, 2016. URL: `https://www.compositesworld.com/articles/sampe-europe-highlights-composites-face-challenges-in-next-commercial-airframes`, accessed on 12/12/2022.

[26] C. A. J. R. Vermeeren, J. L. C. G. De Kanter, O. C. van der Jagt, and B. C. L. Out. Glare design aspects and philosophies. *Applied Composite Materials*, 10:257276, 2003.

[27] R. C. Alderliesten, C. D. Rans, Th. Beumler, and R. Benedictus. Recent advancements in thin-walled hybrid structural technologies for damage tolerant aircraft fuselage applications. *26th ICAF Symposium-Montreal*, pages 105–117, 2011.

[28] T. Beumler. EP2907654A1, 2014.

[29] A.D. Bied-Charreton. Friction stir welding effects of defects in glare. Master's thesis, Delft University of Technology, 2019.

[30] G. Roebroeks. Report TD-R-97-007: The self forming technique - recent progress in the development of a method to produce large aircraft fuselage panels of Glare, 1997.

[31] J. H. van Tongeren. Report NLR-CR-98606: Splice theoretical analysis GTO subproject 1.4.1, 1998.

[32] B. Out. Tolerances of splices. Master's thesis, Delft University of Technology, 2000.

[33] J. Schijve. *Fatigue of Structures and Materials.* Springer Science+Business Media B.V., 2009.

[34] M. Smolnicki, G. Lesiuk, Sz. Duda, and A. M. P. de Jesus. A review on finite-element simulation of fibre metal laminates. *Archives of Computational Methods in Engineering*, 2022.

[35] S. Sugiman and A. D. Crocombe. The static and fatigue response of metal laminate and hybrid fibre-metal laminate doublers joints under tension loading. *Composite Structures*, 94:2937–2951, 9 2012.

[36] M. Smolnicki and P. Stabla. Finite-element method analysis of fibre-metal laminates considering different approaches to material model. *SN Applied Sciences*, 1, 5 2019.

[37] R. C. Alderliesten. Analytical prediction model for fatigue crack propagation and delamination growth in Glare. *International Journal of Fatigue*, 29:628–646, 4 2007.

[38] T. J. De Vries, A. Vlot, and F. Hashagen. Delamination behavior of spliced fiber metal laminates. Part 1. Experimental results. *Composite Structures*, 46:131–145, 1999.

[39] R. C. Alderliesten. Analytical prediction model for fatigue crack propagation and delamination growth in glare. *International Journal of Fatigue*, 29:628–646, 4 2007.

[40] G. S. Wilson, R. C. Alderliesten, and R. Benedictus. A generalized solution to the crack bridging problem of fiber metal laminates. *Engineering Fracture Mechanics*, 105:65–85, 6 2013.

[41] R. F. H. van Maris. Prediction of fatigue crack growth and damage directionality in non-conventional fibre metal laminates. Master's thesis, Delft University of Technology, 2019.

[42] M. Gupta. *Directionality of damage growth in fibre metal laminates and hybrid structures.* PhD thesis, Delft University of Technology, 2017.

[43] J. A. Pascoe, R. C. Alderliesten, and R. Benedictus. Methods for the prediction of fatigue delamination growth in composites and adhesive bonds - a critical review. *Engineering Fracture Mechanics*, 112-113:72–96, 11 2013.

[44] R. C. Alderliesten. Damage tolerance of bonded aircraft structures. *International Journal of Fatigue*, 31:1024–1030, 6 2009.

[45] S. Yuan, Y. B. Li, M. H. Huang, and J. Li. Determination of key parameters of AlLi alloy adhesively bonded joints using cohesive zone model. *Journal of Central South University*, 25:2049–2057, 9 2018.

[46] M. Soroush, K. Malekzadeh-Fard, and M. Shahravi. Finite element simulation of interlaminar and intralaminar damage in laminated composite plates subjected to impact. *Latin American Journal of Solids and Structures*, 15, 6 2018.

[47] A. G. Gibson. Through-thickness elastic constants of composite laminates. *Journal of Composite Materials*, 47:3487–3499, 12 2013.

[48] S. G. Lekhnitskii. *Anisotropic Plates.* 1968.

[49] J.J. Homan. Gtm report 2021-077: FML splice design, CONFIDENTIAL, 2021.

[50] EASA. Airworthiness certificate - airbus, 2014. URL: `https://www.easa.europa.eu/sites/default/files/dfu/TCDS_EASA%20A%20064_%20Airbus_%20A318_A319_A320_A321_Iss_14_20140714.pdf`.

[51] C. Ashforth and L. Ilcewicz. Certification of bonded aircraft structure and repairs. 2018.

Appendix A

Classical Laminate Theory Approach

This appendix chapter is meant to provide Classical Laminate Theory methodology that have been used in the research of this thesis. All the equations displayed are displayed in a way that can be taken straight to numerical implementation.

A.1 Mechanical properties

Local stiffness matrix is computed using the in-plane engineering constants of the UD material given for S2-glass GFRP with FM94 epoxy matrix system, properties given in Table 3.2 and Table 3.6.

$$Q = \begin{bmatrix} E_1/C & \nu_{12}E_2/C & 0 \\ \nu_{21}E_1/C & E_2/C & 0 \\ 0 & 0 & G_{12} \end{bmatrix} \qquad where\ C = 1 - \nu_{12}\nu_{21}$$

The stiffness matrix is with reference to the principal (or local) coordinate system, and it has to be transported into the global one in order to be able to superimpose the layers and their properties into a combined laminate.

$$T_\sigma = \begin{bmatrix} cos(\theta)^2 & sin(\theta)^2 & 2cos(\theta)sin(\theta) \\ sin(\theta)^2 & cos(\theta)^2 & -2cos(\theta)sin(\theta) \\ -cos(\theta)sin(\theta) & cos(\theta)sin(\theta) & cos(\theta)^2 - sin(\theta)^2 \end{bmatrix}$$

$$T_\varepsilon = \begin{bmatrix} cos(\theta)^2 & sin(\theta)^2 & cos(\theta)sin(\theta) \\ sin(\theta)^2 & cos(\theta)^2 & -cos(\theta)sin(\theta) \\ -2cos(\theta)sin(\theta) & 2cos(\theta)sin(\theta) & cos(\theta)^2 - sin(\theta)^2 \end{bmatrix}$$

Where θ is the angle of the principal coordinate system (aligned with the fibers) with respect to the global coordinate system (usually aligned with the specimen). The transformation itself is:

$$Q' = T_\sigma^{-1} Q T_\varepsilon$$

The ABD matrix components are found by doing the following summations:

$$A_{ij} = \sum_{k=1}^{n} Q_{ij}^{(k)} (z_k - z_{k-1})$$
$$B_{ij} = \frac{1}{2} \sum_{k=1}^{n} Q_{ij}^{(k)} (z_k^2 - z_{k-1}^2)$$
$$D_{ij} = \frac{1}{3} \sum_{k=1}^{n} Q_{ij}^{(k)} (z_k^3 - z_{k-1}^3)$$

where z_k is the z-coordinate of the bottom of each ply with reference in the middle of the laminate, with $k = 0$ being the bottom-most ply.

Performing the above calculation and assembling the matrix results in:

$$\begin{Bmatrix} Nx \\ Ny \\ Ns \\ Mx \\ My \\ Ms \end{Bmatrix} = \begin{bmatrix} Axx & Axy & Axs & Bxx & Bxy & Bxs \\ Axy & Ayy & Ays & Bxy & Byy & Bys \\ Axs & Ays & Ass & Bxs & Bys & Bss \\ Bxx & Bxy & Bxs & Dxx & Dxy & Dxs \\ Bxy & Byy & Bys & Dxy & Dyy & Dys \\ Bxs & Bys & Bss & Dxs & Dys & Dss \end{bmatrix} \begin{Bmatrix} \varepsilon_x^0 \\ \varepsilon_y^0 \\ \varepsilon_s^0 \\ k_x \\ k_y \\ k_s \end{Bmatrix}$$

Where the ABD matrix now represents the properties of the entire laminate instead of just one ply. The equivalent properties of the built-up laminate can be deduced via the following equations:

$$\begin{aligned} E_x &= \frac{1}{ha_{xx}} & E_{xf} &= \frac{12}{h^3 d_{xx}} \\ E_y &= \frac{1}{ha_{yy}} & E_{yf} &= \frac{12}{h^3 d_{yy}} \\ \nu_{xy} &= -\frac{a_{xy}}{a_{xx}} & \nu_{xyf} &= -\frac{d_{xy}}{d_{xx}} \\ \nu_{yx} &= -\frac{a_{xy}}{a_{yy}} & \nu_{yxf} &= -\frac{d_{xy}}{d_{yy}} \\ G_{xy} &= \frac{1}{ha_{ss}} & G_{xyf} &= \frac{12}{h^3 d_{ss}} \end{aligned}$$

A.2 Thermal properties

Thermal properties, available again in Table 3.2 and Table 3.6, are used in order to evaluate the residual stresses within the laminate, layer by layer. These residual stresses are a result of the difference in CTEs between the aluminium alloys layers and the GFRP layers, causing additional stresses that these layers exert onto each other. CTEs can be prescribed as a vector:

$$\alpha_t = \begin{Bmatrix} \alpha_{t,x} \\ \alpha_{t,y} \\ 0 \end{Bmatrix}$$

All CTEs must be converted into the global reference system by transforming the local CTE vector into the global one like so:

$$\alpha_t' = T_\varepsilon^{-1}\alpha_t = \begin{Bmatrix} \alpha_{t,x}cos^2(\theta) + \alpha_{t,y}sin^2(\theta) \\ \alpha_{t,x}sin^2(\theta) + \alpha_{t,y}cos^2(\theta) \\ (\alpha_{t,x} - \alpha_{t,y})cos(\theta)sin(\theta) \end{Bmatrix}$$

The fictitious thermal loads are then computed:

$$N^T = \left[\sum_{k=1}^{n} Q_k \alpha_{t,k}'(z_k - z_{k-1})\right]\Delta T$$

$$M^T = \frac{1}{2}\left[\sum_{k=1}^{n} Q_k \alpha_{t,k}'(z_k^2 - z_{k-1}^2)\right]\Delta T$$

A.3 Thermal and mechanical stresses

Having obtained the fictitious thermal loads and the mechanical loads from the ABD matrix, it is thus possible to combine the two in order to obtain total strains and curvatures:

$$\begin{Bmatrix} \varepsilon_{tot} \\ \kappa_{tot} \end{Bmatrix} = [ABD] \begin{Bmatrix} N + N^T \\ M + M^T \end{Bmatrix}$$

Finally, to calculate the stresses of each layer with respect to the global coordinate system:

$$\sigma_k = Q_k(\varepsilon_{tot} + \kappa_{tot} - \alpha_k' \Delta T)$$

If only mechanical stresses are desired, the N^T and M^T can be set to zero, and the $\alpha_k' \Delta T$ term can removed to obtain purely mechanical stresses. For thermal stresses only, N and M are set to 0.